UNIVERSITY OF CALIFORNIA

Santa Barbara


Modulation-Doped $SrTiO_3$/$SrTi_{1-x}Zr_xO_3$ Heterostructures


A dissertation submitted in partial satisfaction of the

requirements for the degree Doctor of Philosophy

in Materials


by


Adam Paul Kajdos


Committee in charge:

Professor Susanne Stemmer, Chair

Professor S. James Allen

Professor James S. Speck

Professor Christopher Palmstrøm


March 2015

The dissertation of Adam Paul Kajdos is approved.

_____

Christopher Palmstrøm

_____

James S. Speck

_____

S. James Allen

_____

Susanne Stemmer, Committee Chair

January 2015

VITA OF ADAM PAUL KAJDOS
JANUARY 2015

EDUCATION

Bachelor of Science in Materials Science and Engineering, Georgia Institute of Technology, May 2010
Doctor of Philosophy in Materials, University of California, Santa Barbara, January 2015 (expected)

PUBLICATIONS

- **A. P. Kajdos** and S. Stemmer. Surface reconstructions in molecular beam epitaxy of $SrTiO_3$. Appl. Phys. Lett. 105, 191901 (2014).
- A. Verma, **A. P. Kajdos**, T. A. Cain, S. Stemmer, and D. Jena. Intrinsic Mobility Limiting Mechanisms in Lanthanum-doped Strontium Titanate. Phys. Rev. Lett. 112, 216601 (2014)
- **A. P. Kajdos**, D. G. Ouellette, T. A. Cain, and S. Stemmer. Two-dimensional Electron Gas in a Modulation-doped $SrTiO_3$/$Sr(Ti, Zr)O_3$ Heterostructure. Appl. Phys. Lett. 103, 082120 (2013)
- W. Han, X. Jiang, **A. P. Kajdos**, S. H. Yang, S. Stemmer, S. S. P. Parkin. Spin Injection and Detection in Lanthanum- and Niobium-doped $SrTiO_3$ Using the Hanle technique. Nature Comm. 4, 2134 (2013)
- P. Moetakef, J. Y. Zhang, S. Raghavan, **A. P. Kajdos**, and S. Stemmer. Growth Window and Effect of Substrate Symmetry in Hybrid Molecular Beam Epitaxy of a Mott Insulating Rare Earth Titanate. J. Vac. Sci. Technol. A31, 041503 (2013)
- T. A. Cain, **A. P. Kajdos**, and S. Stemmer. La-doped $SrTiO_3$ Films With Large Cryogenic Thermoelectric Power Factors. Appl. Phys. Lett. 102, 182101 (2013)
- E. Mikheev*, **A. P. Kajdos***, A. J. Hauser, and S. Stemmer. Electric Field-tunable $Ba_xSr_{1-x}TiO_3$ Films with High Figures of Merit Grown by Molecular Beam Epitaxy. Appl. Phys. Lett. 101, 252906 (2012) *equal contributors
- P. Moetakef, J. R. Williams, D. G. Ouellette, **A. P. Kajdos**, D. Goldhaber-Gordon, S. J. Allen, and S. Stemmer. Carrier-Controlled Ferromagnetism in $SrTiO_3$. Phys. Rev. X 2, 021014 (2012)
- A. M. Kaiser, A. X. Gray, G. Conti, B. Jalan, **A. P. Kajdos**, A. Gloskovskii, S. Ueda, Y. Yamashita, K. Kobayashi, W. Drube, S. Stemmer, and C. S. Fadley. Electronic Structure of Delta-doped La:$SrTiO_3$ Layers by Hard X-ray Photoelectron Spectroscopy. Appl. Phys. Lett. 100, 261603 (2012)
- J. Son, B. Jalan, **A. P. Kajdos**, L. Balents, S. J. Allen, and S. Stemmer. Probing the Metal-insulator Transition of $NdNiO_3$ by Electrostatic Doping. Appl. Phys. Lett. 99, 192107 (2011)

AWARDS

- National Science Foundation Graduate Research Fellowship (2012-2015)

- Graduate Assistance in Areas of National Need Fellowship, University of California, Santa Barbara (2010-2012)
- Phi Kappa Phi Award (Georgia Institute of Technology, 2010)
- Outstanding Senior Award (Georgia Institute of Technology, 2010)
- Outstanding Undergraduate Researcher in the College of Engineering (Georgia Institute of Technology, 2010)
- Henry Ford II Scholarship (2009)
- Chapman/Pentecost Scholarship (2009)
- Presidents Undergraduate Research Award (2009)

ABSTRACT


Modulation-Doped $SrTiO_3$/$SrTi_{1-x}Zr_xO_3$ Heterostructures


by


Adam Paul Kajdos

Two-dimensional electron gases (2DEGs) in $SrTiO_3$ have attracted considerable
attention for exhibiting a variety of interesting physical phenomena, such as
superconductivity and magnetism. So far, most of the literature has focused on interfaces
between nonpolar $SrTiO_3$ and polar perovskite oxides (e.g. $LaAlO_3$ or rare-earth titanates),
where high carrier density 2DEGs ($\sim 3 \times 10^{14}$ $cm^{-2}$) are generated by polar discontinuity.
Modulation doping is an alternative approach to generating a 2DEG that has been explored
extensively in III-V semiconductors but has not heretofore been explored in complex oxides.
This approach involves interfacing an undoped semiconductor with a doped semiconductor
whose conduction band edge lies at a higher energy, which results in electrons diffusing into
the undoped semiconductor transport channel, where scattering from ionized dopants is
minimized. Realizing a high-mobility modulation-doped structure with a $SrTiO_3$ transport
channel therefore requires both the optimization of the transport channel by minimizing
native defects as well as the development of a perovskite oxide which has a suitable band
offset with $SrTiO_3$ and can be electron-doped.

The growth of high electron mobility $SrTiO_3$ as a suitable transport channel material was
previously demonstrated using the hybrid molecular beam epitaxy (MBE) approach, where

Sr is delivered via a solid source and Ti is delivered using a metal-organic precursor, titanium (IV) tetra-isopropoxide (TTIP). Expanding on this, *in-situ* reflection high-energy electron diffraction (RHEED) is used to track the surface and resulting film cation stoichiometry of homoepitaxial $SrTiO_3$ (001) thin films grown by hybrid MBE. It is shown that films with lattice parameters identical to bulk single-crystal substrates within the detection limit of high-resolution X-ray diffraction (XRD) measurements exhibit an evolution in surface reconstruction with increasing TTIP beam-equivalent pressure. The change in the observed surface reconstruction from (1×1) to (2×1) to c(4×4) is correlated with a change from mixed $SrO/TiO_2$ to pure $TiO_2$ surface termination. It is argued that optimal cation stoichiometry is achieved for growth conditions within the XRD-defined growth window that result in a c(4×4) surface lattice.

The development of a doped perovskite oxide semiconductor with a suitable conduction band offset is then discussed as the next necessary step towards realizing modulation-doped heterostructures. The $SrTi_xZr_{1-x}O_3$ solid solution is investigated for this purpose, with a focus on optimizing cation stoichiometry to allow for controlled doping. In particular, the hybrid MBE growth of $SrTi_xZr_{1-x}O_3$ thin films is explored using a metal-organic precursor for Zr, zirconium *tert*-butoxide (ZTB). The successful generation of 2DEGs by modulation doping of $SrTiO_3$ is then demonstrated in $SrTiO_3/La:SrTi_{0.95}Zr_{0.05}O_3$ heterostructures, and the electronic structure is studied by Shubnikov-de Haas analysis using multiple-subband models.

TABLE OF CONTENTS

# Chapter 1

## Introduction

The study of electronic transport confined to two dimensions represents one of the most dominant areas of interest in semiconductor research, building on decades of work spanning a vast array of material systems. Research and development of two-dimensional electron and hole gases (2DEGs and 2DHGs, respectively) in group IV[1, 2], III-V[3-7] (including nitrides [8, 9]), and II-VI [10] semiconductors enabled a multitude of electronic device technologies for logic circuits and signal processing. 2DEGs not only play a major role in commercially ubiquitous (FET) structures, but they also serve as a valuable system for studying exotic quantum phenomena such as the integer [11] and fractional [12] quantum Hall effects, that only arise in 2D-confined electron systems, in which electrons are confined to motion within a plane (typically at an interface or surface).

More recently, there has been considerable interest in studying 2DEGs in complex oxide heterostructures, in particular those based on perovskite oxides. This class of materials exhibits a large variety of electrical and magnetic properties, including but not limited to superconductivity [13], ferromagnetism [14], ferroelectricity [15], and Mott metal-insulator transitions [16]. The prospect of integrating any number of these phenomena into an all-oxide electronic device drives much of the work on developing higher-quality materials to match traditional semiconductor standards of purity and defect control, as well as the study of their electronic structure.

$SrTiO_3$, a perovskite oxide superconductor ($T_C \leq 350$ mK [13]) and incipient ferroelectric with high low-temperature electron mobilities ($\sim 10^4$ cm$^2$V$^{-1}$s$^{-1}$ in bulk single crystals [17, 18]), has attracted significant attention for studies of 2D transport in complex oxides. This is in part because electronic transport occurs in a conduction band derived from Ti 3d orbitals, which are expected to exhibit transport properties substantially different from

group IV and III-V semiconductors, whose conduction bands are derived primarily from s-p hybridized orbitals. Free electrons in these narrow-bandwidth d-orbital-derived bands experience stronger electron-electron correlations [19], which play a role in Mott metal-insulator transitions and various magnetic ordering phenomena. The availability of n-type dopants (e.g. La and Nb) and relatively high electron mobilities also contribute to the interest in $SrTiO_3$ as a prototypic complex oxide semiconductor.

High electron mobility allows for the resolution of features in the electronic structure through magnetoresistance measurements. Typically, one may extract information about properties such as carrier density, charge carrier effective mass, and electronic subband energy spacings either directly or indirectly from oscillations in the longitudinal magnetoresistance $R_{xx}(B)$ (i.e. Shubnikov-de Haas oscillations), which will be discussed in greater detail in Section 1.2. The angular dependence of Shubnikov-de Haas oscillations further enables the confirmation of the two-dimensional confinement of carriers. For the purpose of introduction, it should be stated that the information above can only be extracted if electron mobility is sufficiently high, typically according to the criterion $\mu B > 1$, where $\mu$ is the quantum mobility of electrons in a magnetic field with magnitude $B$. This criterion holds true for both 3D and 2D electronic systems. The study of 2DEGs in $SrTiO_3$, as in any other material system, is thus greatly enhanced by high charge carrier mobility.


## 1.1 2DEGs in $SrTiO_3$

Interest in studying 2D transport in $SrTiO_3$ has led to the exploration of a number of approaches to generating 2DEGs in this system, including both new and traditional methods developed in more mature semiconductor systems. Perhaps the most thoroughly explored

2DEGs in $SrTiO_3$ are those formed via a polar discontinuity at the interface between a polar perovskite and nonpolar $SrTiO_3$. This configuration is most commonly realized at the interface between $LaAlO_3$ and $SrTiO_3$ [20], though substantial research efforts have also focused on $RTiO_3/SrTiO_3$ interfaces, where R represents a rare-earth metal (e.g. La [21, 22], Gd [23], Sm [24], Nd [25]).

The polar discontinuity mechanism leads to a 2DEG at the interface between a polar and nonpolar oxide by introducing a fixed sheet charge at the interface, though in a fundamentally different manner than for polarization-induced 2DEGs in GaN/AlGaN, for example. The terms "polar" and "nonpolar" in the context of polar discontinuity refer to the stacking of atomic layers, rather than a spontaneous bulk electrical polarization. To illustrate this point, $LaAlO_3$ can be described as a stack of alternating $LaO^+$ and $AlO_2^-$ atomic monolayers along the [001] crystallographic direction. Thus $LaAlO_3$ consists of bilayers with electrical polarity and as such can be described as polar, whereas $SrTiO_3$ consists of alternating neutral layers, $SrO^0$ and $TiO_2^0$, and as such is nonpolar. If the interface is formed between $LaO^+$ and $TiO_2^0$, a divergent electrostatic potential requires charge reconstruction, resulting in a 2DEG with a density equal to half an electron per planar unit cell ($\sim 3 \times 10^{14}$ $cm^{-2}$) [20].

Polar/nonpolar complex oxide 2DEGs display many interesting properties that motivate continued research in this area, such as coexisting superconductivity and ferromagnetism [26]. There is, however, interest in investigating 2DEGs with lower charge carrier densities ($< 10^{13}$ $cm^{-2}$) to investigate long-range Coulomb interactions or to simplify analysis of the electronic structure by filling fewer electronic subbands. In the case of 2DEGs formed by polar discontinuity, achieving low charge carrier densities in a controlled fashion is difficult

due to the inherently large interface charge in these systems. Electric-field gating of such large carrier densities is a challenge that has been met with limited success [27-29], though another route to much lower charge carrier densities and higher mobilities remains a necessary endeavor.

Compared to polar/nonpolar interfaces, delta-doping is a less explored route to generating 2DEGs in SrTiO$_3$. Originally developed for III-V semiconductors grown by MBE [6, 30], delta-doping is effected by confining donors in a semiconductor to a single atomic layer, and as such the dopant concentration profile can be approximated as a delta function. Confining the dopants to a single atomic layer is not a strict requirement for delta-doping; the doped layer need only be thinner than the spatial extent of the ground state wave function for a potential well from a given carrier density [6]. In this configuration, electrons diffuse away from their donors, and this diffusion is counterbalanced by Coulombic attraction between the electrons and their ionized dopants. Thus the charge carriers are effectively limited to motion in the vicinity of the plane of dopant atoms, forming a 2DEG.

SrTiO$_3$ has so far been successfully delta-doped with La substitution on the perovskite A-site and Nb [31] doping on the perovskite B-site [31]. The 2D nature of the electronic transport in these systems has been confirmed with Shubnikov-de Haas oscillations in both cases, and Nb-delta-doped SrTiO$_3$ was shown to exhibit 2D superconductivity. Unfortunately, engineering delta-doped semiconductors with higher mobility is hindered by scattering from a high density of ionized dopants in the doping plane for real systems with finite interface roughness, and the mitigation of ionized dopant scattering by reducing the concentration of dopants is limited by the minimum density required to maintain a confining

5

Coulombic potential [6]. Again, as was the case for polar/nonpolar interfaces, another approach is necessary to generate higher-mobility, low-carrier-density 2DEGs in SrTiO$_3$.

The development of more traditional MOSFET-type structures with undoped SrTiO$_3$ (without a high-density polar/nonpolar 2DEG) as the semiconducting channel has also been explored for studies of 2-D transport [32-35]. Such structures have attracted attention for their value in any studies involving systematic changes in 2-D carrier density regulated by gate bias in group IV [1] and III-V [7] semiconductors. Unfortunately, SrTiO$_3$ MOSFET structures exhibit relatively low charge carrier mobilities due to a large number of interfacial defect states [33, 34], limiting their usefulness for investigating electronic structure and various physical phenomena.

One method heretofore unexplored for generating 2DEGs in SrTiO$_3$, or any other complex oxide for that matter, is modulation doping [36]. The basic principle of this doping scheme relies on separating charge carriers in a semiconductor from their ionized dopants, thus increasing electron mobility. In practical terms, this involves interfacing an undoped semiconductor with a doped semiconductor whose conduction band edge lies at a relatively higher energy (for n-type modulation doping, see Fig. 1.1), which causes electrons to diffuse into the undoped semiconductor. These electrons are then confined to the interface by Coulombic attraction to the ionized dopants, while remaining in the undoped semiconductor due to the presence of a barrier at the interface. By spatially separating electrons from their ionized donors, ionized dopant scattering is reduced, and thus electron mobility is increased.

The modulation doping approach has been successfully employed in a variety of configurations in the III-V semiconductor family, yielding low-density 2DEGs with the highest recorded electron mobilities of any semiconductor system [5, 37]. The vast library of

6

research resulting from the development of modulation-doped 2DEGs in III-V

semiconductors can only suggest vast possibilities for discovery in complex oxides, which

as a class of materials exhibit a much greater variety of physical phenomena. The following

sections will discuss modulation-doped semiconductor heterostructures in greater detail with

the intention of outlining an approach to realize such structures in the complex oxide

$SrTiO_3$.

### 1.1.1 Modulation-doped III-V heterostructures

As mentioned above, one of the most prolific areas of research on 2DEGs has

centered on modulation-doped III-V semiconductors, where $GaAs/Al_xGa_{1-x}As$

heterostructures in particular serve as the prototypic system for this doping scheme. The first

modulation doped configuration was explored as a superlattice consisting of alternating

undoped GaAs and doped $Al_xGa_{1-x}As$ layers, with the undoped transport channel in direct

contact with the doped barrier layer [36]. A single-interface configuration led to

improvements in electron mobility in 2DEGs [5, 38] and led to the development of

modulation-doped FET (MODFET) structures, also referred to as high-electron-mobility

transistor (HEMT), similar to that shown in Fig. 1.1. This type of structure can be generally

classified as a selectively-doped heterostructure (SDH).

Incorporating an undoped spacer layer between the doped barrier layer and the

transport channel has been shown to drastically improve mobility in SDH's by further

separating the charge carriers in the transport channel from their ionized dopants. This

improved mobility (by nearly an order of magnitude) comes at the expense of the density of

charge carriers transferred to the transport channel [39]. In spite of this, undoped spacer
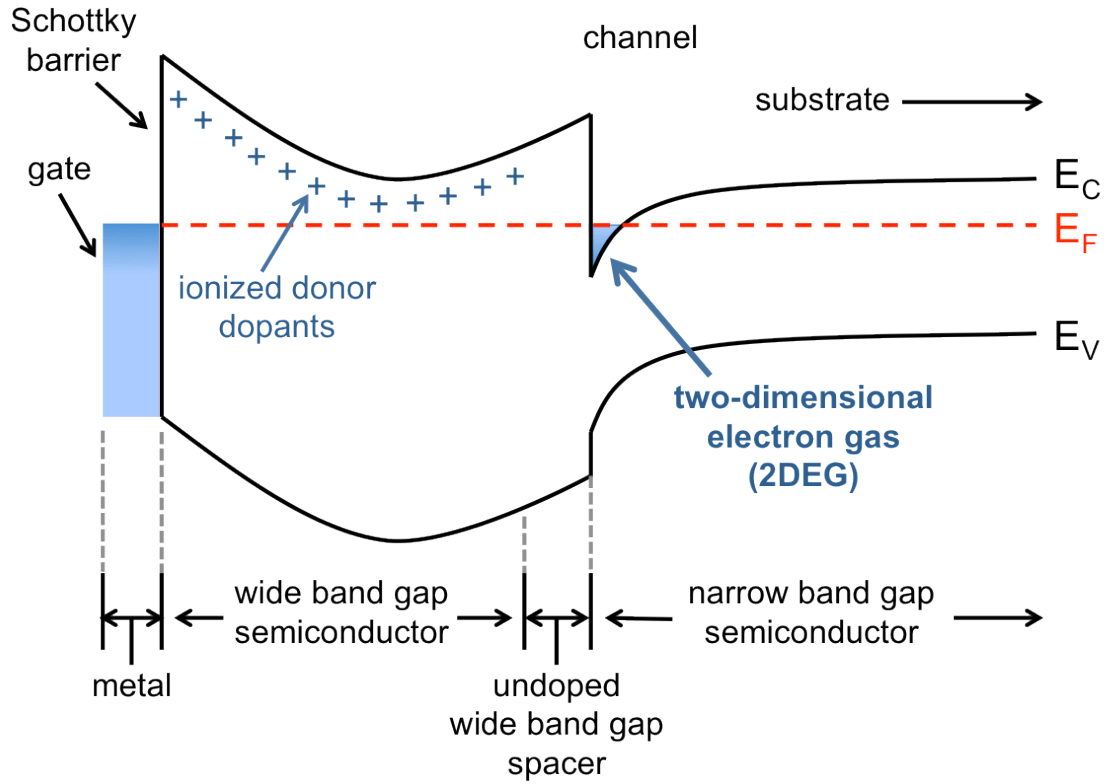
**Figure 1.1:** Schematic band diagram of a modulation-doped field-effect transistor (MODFET) or high-electron-mobility transistor (HEMT) heterostructure, valid for a type I band alignment. $E_C$, $E_F$, and $E_V$ mark the conduction band edge, Fermi level, and valence band edge, respectively.

layers are a standard feature in modulation-doped heterostructures [5].

Modulation doping can also been effected without needing to dope the barrier layer at all. In a selectively-*delta*-doped GaAs/Al$_x$Ga$_{1-x}$As heterostructure (SDDH), a delta-doped Al$_x$Ga$_{1-x}$As layer or GaAs/Al$_x$Ga$_{1-x}$As quantum well is placed in the vicinity of a GaAs/Al$_x$Ga$_{1-x}$As interface transport channel. This approach has the advantage of effectively increasing the conduction band discontinuity at the interface by the value of the ground state energy in the well, and it also mitigates the effects of surface depletion, allowing for a higher carrier density to be transferred to the conducting channel [6].

More complicated structures incorporating short-period superlattice (SPSL) delta-doping structures, among other refinements and modifications, have been conceived for achieving extremely high electron mobilities (exceeding $3 \times 10^7$ cm$^2$V$^{-1}$s$^{-1}$) in III-V heterostructures structures [37]. However, in the interest of developing a roadmap for developing modulation-doped SrTiO$_3$ heterostructures, the simpler selectively-doped and selectively-delta-doped heterostructures are more appropriate for initial exploration. Prior to that, it will be necessary to first establish a suitable barrier material for band-gap engineering in SrTiO$_3$, as will be discussed in the next section.

*1.1.2 A modulation-doped 2DEG in SrTiO$_3$*

Realizing a modulation-doped 2DEG in SrTiO$_3$ necessitates the development of a suitable doped barrier material to deliver charge carriers to the undoped transport channel. This barrier material must, as the name suggests, provide a barrier at the interface for electron confinement. More specifically, it must exhibit a positive conduction band offset with SrTiO$_3$. The barrier material must also be amenable to n-type doping to be viable for a

modulation doping scheme, and structural compatibility between the undoped channel and the doped barrier layer must also be considered. Both should be sufficiently lattice-matched to prevent excessive scattering or charge-carrier trapping at the interface due to defects. As such, a perovskite oxide with a positive conduction band offset with $SrTiO_3$ that can be doped n-type would prove an ideal candidate for modulation doping.

One material that attracts attention as a candidate for modulation doping $SrTiO_3$ is $SrZrO_3$, a large band-gap ($E_g = 5.6$ eV [40]) orthorhombic (space group Pbnm [41]) perovskite oxide band insulator. Of particular interest is the large conduction band offset between $SrTiO_3$ and $SrZrO_3$ ($\Delta E_c = 1.9$ eV) in a type I band alignment [42]. In terms of band offsets, this is ideal for modulation doping; however, there are other concerns that limit the usefulness of $SrZrO_3$ as a doped barrier. For one, the lattice mismatch between $SrZrO_3$ and $SrTiO_3$ is substantial, both in terms of size ($\Delta a \sim 5\%$, assuming a pseudocubic lattice parameter for $SrZrO_3$: $a = 4.11$ Å [41]) and symmetry. Defects resulting from the mismatch or from domain formation are problematic for controlled doping of the barrier layer as well as for engineering of an interface with high structural quality. Furthermore, it is unlikely that any shallow donors exist for $SrZrO_3$; it is a large band-gap insulator with no reports of electronic conduction available in the literature. That being said, $SrZrO_3$ remains a valuable candidate as an undoped barrier material in other perovskite oxide heterostructures.

Given the potential issues with using pure $SrZrO_3$ outlined above, a more reasonable approach could utilize the alloy system $SrTi_{1-x}Zr_xO_3$. Several reports have been published on the structure of this material system [41, 43, 44], showing a solid solution across the entire range $0 < x < 1$. For small amounts of Zr content, $x < 0.05$, the alloy maintains a Pm3-m lattice with a reasonable lattice size match with $SrTiO_3$. Although no reports have heretofore

been published on the electronic structure or transport in this alloy system, one may

hypothesize that for small enough Zr substitution, $SrTi_{1-x}Zr_xO_3$ can be doped n-type, similar

to $SrTiO_3$. Furthermore, if one assumes a Vegard's Law relation between the Zr content and

conduction band offset, relatively small amounts of Zr substitution are necessary to produce

a sufficient conduction band offset for modulation doping. For these reasons, developing

and studying prototypic $SrTiO_3/SrTi_{1-x}Zr_xO_3$ modulation doped systems is a reasonable step

towards realizing high-mobility, low-density 2DEGs in complex oxides.


## 1.2 Shubnikov-de Haas Analysis of 2DEGs

Oscillations of the longitudinal magnetoresistance $R_{xx}$ periodic in inverse magnetic

field $1/B$ are collectively referred to as Shubnikov-de Haas (SdH) effect. This effect has

been utilized as a means to extract valuable information about the band structure of many

semiconductor 2DEGs with sufficiently high electron mobility. The frequency, as well as

the temperature-dependence and field-dependence of the amplitude of these

magnetoresistance oscillations depend on properties such as the electron density, effective

mass, and charge carrier lifetime, respectively. The angle-dependence of the oscillations

allows for an unambiguous test of the two-dimensional nature of the system. As such, the

Shubnikov-de Haas effect is an invaluable probe of the electronic structure of new 2DEG

systems. To fully appreciate the usefulness of SdH analysis, it is worth discussing the origin

of this effect specifically for a 2D system.

In the most basic sense, the Shubnikov-de Haas effect is a probe of the electronic

structure insofar as the longitudinal magnetoresistance reflects, to some extent, changes in

the density of states near the Fermi level. In a 2D system, the density of states is constant for

each subband and is typically depicted as a step-like structure as a function of energy, with each step representing an additional subband. When a magnetic field is applied, the 2D density of states is partitioned into highly degenerate Landau levels [45], which represent quantized cyclotron energy levels with energies:

$$\varepsilon_n = (n - \tfrac{1}{2})\hbar\omega_c \tag{1.1}$$

where $n$ is any positive integer and $\omega_c$ is the cyclotron frequency

$$\omega_c = \left|\frac{eB}{m*}\right| \tag{1.2}$$

where e is the elementary charge and $m*$ is the effective mass of electrons in the magnetic field. Thus for a fixed mass the energy spacing of these Landau levels depends only on the applied magnetic field $B$.

In an ideal system, the Landau levels themselves are delta functions in energy, but when the electron scattering (due to any number of mechanisms) is taken into account, Landau levels can be assumed to take on a Gaussian [45] or Lorentzian [46, 47] distribution with a finite breadth, typically quantified as a full-width at half maximum given by $\Gamma = \hbar/\tau_q$, where $\tau_q$ is the quantum lifetime of electrons in this scenario. Thus in real systems at low $B$ fields or short quantum lifetimes, where $\hbar\omega_c < \Gamma$, the Landau levels strongly overlap, leading to minimal perturbation of the original 2D density of states. Resolution of individual levels only occurs to a significant extent when $\hbar\omega_c > \Gamma$, which are achieved with either higher fields or longer carrier lifetimes (e.g. at lower temperatures or with higher charge carrier mobilities). It is for this reason that high charge carrier mobility is crucial for tracking the electronic structure with varying field.

If the above criterion is met, oscillations can be observed in the longitudinal magnetoresistance. These oscillations correspond to changes in the density of states at the

Fermi level, as is shown in Fig. 1.2. Since the total electron density $n_{2D}$ of a system is typically fixed, and since the density of states of each Landau level $n_L$ varies with the magnetic field according to the relation $n_L = eB/h$, the Fermi level (or more generally, the Fermi surface) will necessarily adjust to keep the total electron density constant, which requires that Landau levels are successively depleted with increasing magnetic field. When any Landau level is fully depleted, $E_f$ is located at a minimum in the density of states, which corresponds to a *minimum* in $R_{xx}(B)$. Conversely, $R_{xx}(B)$ will exhibit a *maximum* if $E_f$ is located within a Landau level. This differs from transport in the absence of a magnetic field in that the longitudinal resistivity and conductivity scale directly with each other in this scenario [44]. In very high-mobility 2D systems where the Landau level width $\Gamma$ is sufficiently small and $B$ sufficiently high ($\Gamma << \hbar\omega_c$), $R_{xx}(B)$ will go to zero when the density of states vanishes at $E_F$. The transverse magnetoresistance $R_{xy}(B)$ will be constant for a range of $B$ where these conditions hold; this behavior is known as the quantum Hall effect.

The angle-dependence of SdH oscillations (as well as de Haas-van Alphen oscillations) has been used extensively to map the Fermi surface of metals and can similarly be used to determine whether a system is two-dimensional nature. This is due to the fact that the period of the oscillations in $1/B$ is inversely related to the extremal cross-sectional area of the Fermi surface normal to the magnetic field **B** [48]. In a 2-D electronic system, the Fermi surface takes the form of a cylinder in $k$-space (if the in-plane mass is isotropic). If we assume two-dimensional carrier confinement in the x,y-plane, the Fermi vector along $k_z$ is undefined, and the angle-dependence of SdH oscillations will give a oscillation period that is
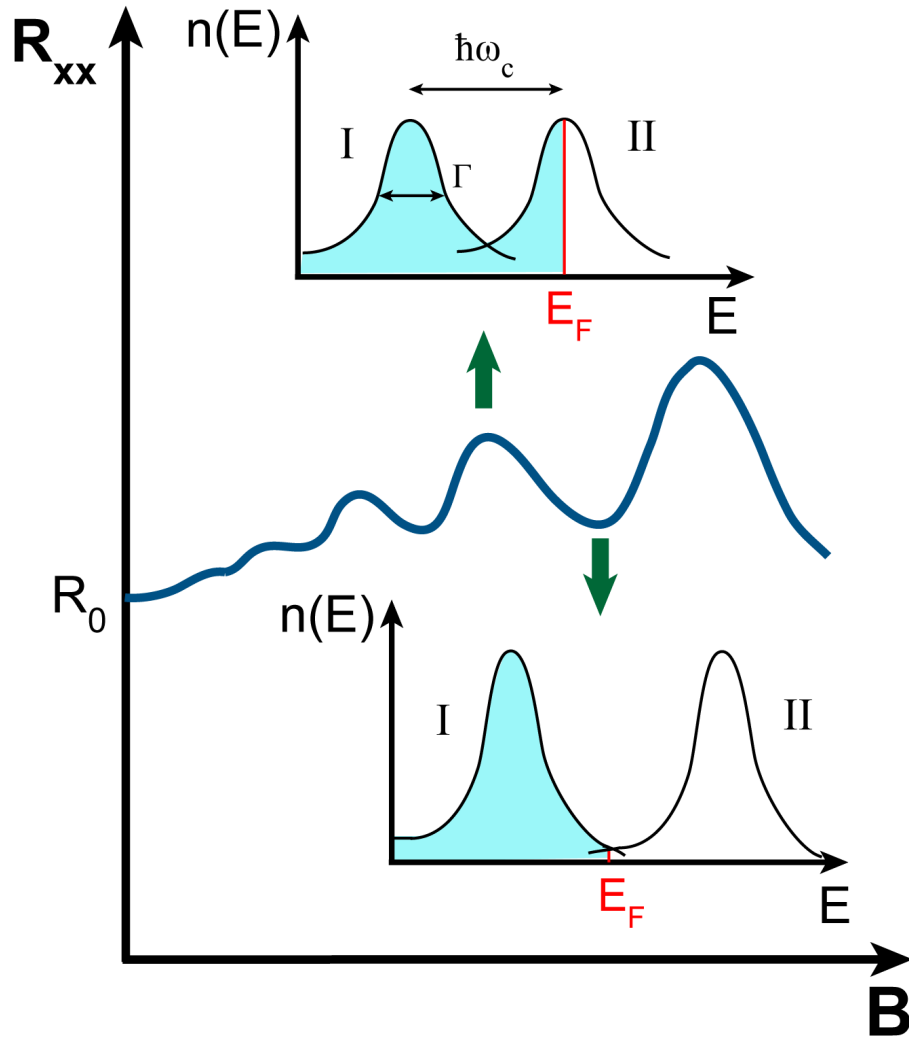
**Figure 1.2:** Illustration of the link between the density of states $n(E)$ and oscillations in the longitudinal magnetoresistance $R_{xx}(B)$ from the Shubnikov-de Haas effect. The Landau levels "I" and "II" are adjacent Landau levels from the same subband. $E_F$ is the Fermi level; $\Gamma$ is the full-width half maximum of the Landau levels; and $\hbar\omega_c$ represents the spacing between the centers of adjacent Landau levels. The areas shaded light-blue represent filled states.

constant with regard to the inverse of the component of the magnetic field **B**: $1/(B\cos\theta)$, where $\theta$ is the angle between **B** and the confinement-plane normal. This behavior can thus be used to confirm the two-dimensional confinement of charge carriers in a system with sufficiently high mobility to resolve SdH oscillations.

To extract information from a 2DEG system with multiple occupied subbands (as is the case for SrTiO$_3$ even at low carrier densities), a standard equation [47] may be used to simulate or fit to Shubnikov-de Haas oscillations from $m$ occupied subbands as a function of $1/B$:

$$\frac{\Delta R_{xx}}{R_0} = \sum_{i=1}^{m} 2A_i \exp\left(\frac{2\pi^2 k_B T_{D,i}}{\hbar\omega_c}\right)\frac{X}{\sinh(X)}\cos\left(\frac{2\pi f_i}{B} + \pi\right) \tag{1.3}$$

where $i$ is the subband index, $A_i$ are amplitude factors related to intrasubband scattering probabilities, $k_B$ is the Boltzmann constant, $T_{D,i}$ is the Dingle temperature of each subband, $\omega_c$ is the cyclotron frequency described in Eq. 1.2, $f_i$ are the oscillation frequencies, and $X = \left(2\pi^2 k_B T\right)/\left(\hbar\omega_c\right)$. By fitting this equation to experimental data, one may extract the effective mass from $\omega_c$, the quantum lifetime $\tau_q$ from the Dingle temperature via

$$\tau_q = \frac{\hbar}{2\pi k_B T_D} \tag{1.4}$$

and the carrier density $n_s$ from each subband via

$$f = \frac{n_s h}{2q} \tag{1.5}$$

for non-spin-split subbands. Extracting this information from experimental data will make up the bulk of the analysis of a modulation-doped complex oxide heterostructures in Chapter 6.

## 1.3 Organization

To realize a 2DEG in $SrTiO_3$ by modulation doping, the hybrid MBE growth of $SrTi_{1-x}Zr_xO_3$ must be explored as a prototype doped barrier layer. In addition, the optimization of $SrTiO_3$ undoped channel must be optimized beyond previous efforts to better suit the growth of more complex heterostructures. With these goals in mind, this dissertation will focus on the following:

- Investigating surface reconstructions as a guide for optimizing MBE growth conditions for $SrTiO_3$ and related perovskite alloy systems, using *in-situ* reflection high-energy electron diffraction (RHEED)

- Developing the hybrid MBE growth of $SrTi_{1-x}Zr_xO_3$

- Investigating the transport properties of $La:SrTi_{1-x}Zr_xO_3$ and $La:SrTi_{1-x}Zr_xO_3/SrTiO_3$ modulation-doped heterostructures (both selectively doped and selectively delta-doped)

Chapter 2 will provide background regarding the hybrid MBE growth technique and previous efforts in stoichiometry optimization of perovskite oxide titanates, with a focus on the materials development to be discussed in this dissertation. Chapter 3 will present a new method for stoichiometry control of hybrid-MBE-grown $SrTiO_3$ utilizing *in-situ* RHEED characterization. Chapter 4 will demonstrate the application of this stoichiometry optimization approach in a related system, the tunable dielectric $Ba_xSr_{1-x}TiO_3$. Chapter 5 will then cover the hybrid MBE growth and characterization of $SrTi_{1-x}Zr_xO_3$ and $SrZrO_3$, as well as electrical transport characterization of $La:SrTi_{1-x}Zr_xO_3$ and $La:SrTi_{1-x}Zr_xO_3/SrTiO_3$ modulation doped heterostructures.

# Chapter 2

## Background: Hybrid MBE Growth of Complex Oxides

*2.1 Introduction*

As discussed in Chapter 1, gaining insight into the electronic structure of materials that exhibit exotic phenomena demands high materials quality. Achieving maximal electron mobility and mitigating the effects of unintentional defects allows for features of the electronic structure to be more clearly observed in Shubnikov-de Haas oscillations. As an example, the fractional quantum Hall effect was only observed in III-V semiconductors once the electron mobility was sufficiently high [5, 12]. The prospect of modulation doping in the complex oxide $SrTiO_3$ is therefore contingent on developing high quality materials for both the conducting channel as well as the doped barrier layer. Fortunately, the success of III-V semiconductor materials development provides some basis for similar developments in complex oxides, particularly with respect to materials synthesis.

Although metal-organic chemical vapor deposition (MOCVD) constitutes a great portion of the industrial synthesis of III-V semiconductors, much of the progress in the research and development of III-V semiconductor heterostructures is enabled by the molecular beam epitaxy (MBE) crystal growth technique. This is in large part due to the level of control afforded by MBE. The technique is based on line-of-sight delivery of vapor-phase constituents sublimated or evaporated from high-purity sources to a crystalline substrate, which typically determines the phase and orientation of the resulting crystalline film. The background pressure during growth is kept sufficiently low such that the mean free path between collisions for these vapor-phase constituents is much greater than the distance between the sources and the substrate. It is under these conditions that a molecular beam will form. Since the arrival rate of the vaporized source elements forming the molecular beam is not confounded by gas-phase interactions or reactions prior to impingement onto the

substrate, a high level of control over the flux is possible. This allows for very precise doping and alloying profiles, which are critical for applications relying on quantum-confinement effects.

The high materials quality enabled by MBE has arguably played the greatest role in the successful development of III-V semiconductor heterostructures. This high quality results in part from a combination of high source purity and low background pressure [5]. The ultra-high vacuum (UHV) background standard in most MBE systems mitigates the incorporation of defects by minimizing the impingement and adsorption of impurity gases on the growing surface. A substantial increase in mobility from improving the integrity of the UHV background, for example, was effected by introducing a load-locked sample loading chamber [39], attesting to the value of maintaining low partial pressures of impurity gases in the MBE growth chamber.

Growth of high-quality thin films by MBE is also largely predicated on the existence of a growth window. The growth window for a particular material defines a range of growth conditions (e.g. growth temperature, absolute and relative fluxes of the vapor-phase source materials, etc.) within which a stoichiometric crystal is thermodynamically favored to grow [49]. In terms of thermodynamics, it defines a two-phase region wherein the stoichiometric crystal is in equilibrium with the vapor of the more volatile constituent. The growth window for GaAs, for example, falls within a range of conditions that favor the growth of stoichiometric GaAs in equilibrium with an As-rich vapor. The thermodynamic system is As-rich overall, in that Ga and As are supplied with an As overpressure, but due to the volatility of As at appropriate growth temperatures, only as much As will incorporate into the film as is needed to form stoichiometric GaAs. Excess As will favor the vapor phase,

19

which can be removed in dynamic vacuum to maintain a controlled steady-state flux, over

solid As in this regime. Therefore, the fluxes of each constituent need not be precisely

controlled to obtain a stoichiometric compound as long as the growth conditions fall within

the growth window. If conditions fall outside of the growth window, the stoichiometric

compound may decompose or evaporate, or solid phases of the excess constituents may be

incorporated into the film, depending on the temperature and composition of the system.

The advantages of MBE growth in materials quality motivate its implementation in the

development of complex oxide semiconductor heterostructures, for which low defect

densities are necessary for studies of the intrinsic physics of these systems. That being said,

the growth of stoichiometric complex oxides using traditional solid-source MBE has proven

difficult for some material systems [50] due to the inaccessibility of the growth window.

This difficulty has led to alternative deposition methods, such as pulsed laser deposition

(PLD) [51] or RF magnetron sputtering [52, 53], to become widely used for the growth of

complex oxides. These deposition techniques allow for the transfer of material from

nominally stoichiometric targets formed by standard bulk synthesis; however, the energies

of impinging species is high, typically on the order of several eV or greater [54]. In contrast,

the energy of impinging species during MBE growth is on the order of the energy of

thermally evaporated species, $\sim k_B T$ or tenths of an eV. The low energy of deposition of

MBE leads to the incorporation of fewer intrinsic defects in the growing film than in the

case of PLD or sputtering. MBE is therefore still ultimately preferred for the growth of

complex oxide heterostructures.

In this chapter, the challenges associated with the MBE growth of complex oxides from

solid sources will be discussed. Background will be provided on the development of hybrid

MBE as a method to address these challenges, prefaced with some discussion of oxide growth from metal-organic compounds.

*2.2 MBE Growth of Complex Oxides*

The MBE growth of complex oxides from solid sources has generally proven difficult primarily due to the relatively low volatility (i.e. low vapor pressure) of their binary oxide constituents, which effectively places the growth window for many complex oxides at impractically high temperatures. As an example, the growth window for $SrTiO_3$ is shown in Fig. 2.1a on a graph of the beam-equivalent pressure of SrO (the more volatile constituent comparing SrO and $TiO_2$) and inverse temperature. To reach the growth window with practical beam-equivalent pressures ($10^{-8}$ to $10^{-6}$ Torr), substrate temperatures in excess of 1200 °C would need to be maintained during growth [55]. Such high temperatures are incompatible with the integrity of substrate heating systems developed for the growth of III-V semiconductors, especially in the presence of highly oxidizing gas species such as ozone or oxygen plasma.

It should be noted that the growth window for some complex oxides, such as $PbTiO_3$ [56] (see Fig. 2.1b) and $BiFeO_3$ [57], exists for practical growth conditions, due to the relatively high volatility of PbO and $Bi_2O_3$, respectively. Although the growth window may be considerably narrower than that for GaAs, for example, adsorption-controlled growth can proceed in a fashion similar to III-V semiconductors under appropriate conditions. For example, a substrate temperature of ~640 °C should hypothetically allow for a growth window for $PbTiO_3$ for a range of PbO beam-equivalent pressures from $10^{-8}$ to $10^{-6}$ Torr [56], which are easily attainable with standard MBE equipment. Unfortunately, these
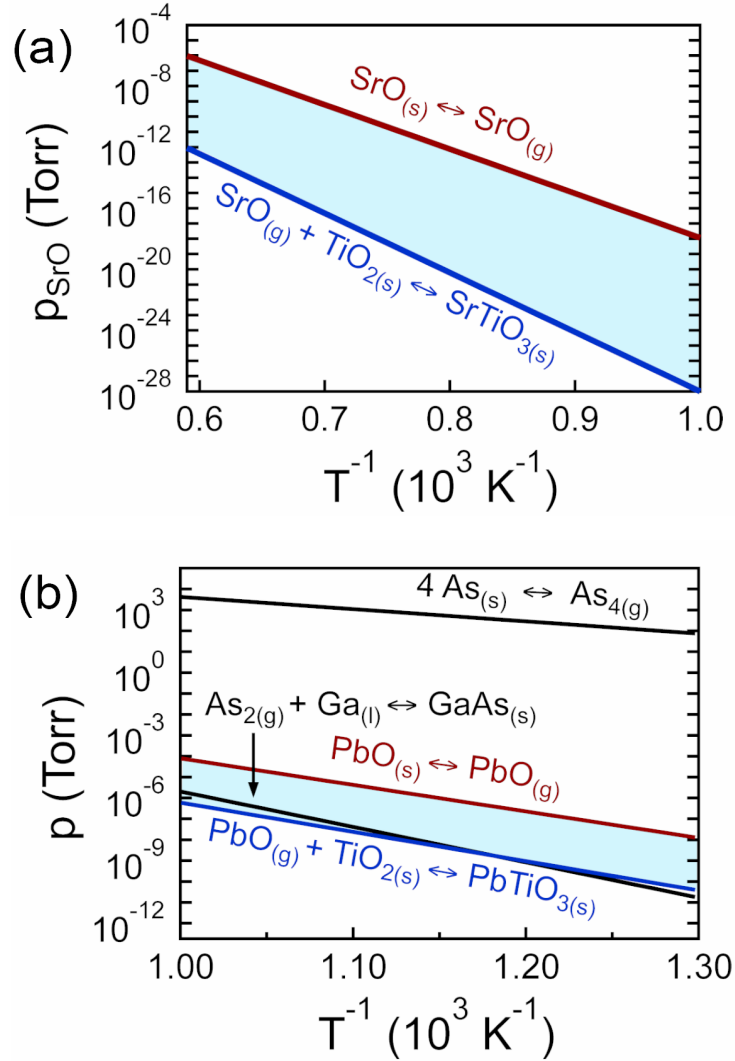
**Figure 2.1:** Equilibrium curves of vapor pressure versus inverse temperature relevant to the solid-source MBE growth of (a) $SrTiO_3$ (adapted with permission from [55]. Copyright 2009, AIP Publishing LLC) and (b) $PbTiO_3$, with GaAs shown for comparison (adapted from [56] with permission from Elsevier). For beam equivalent pressures (BEP) of AO (A = Sr or Pb) below the red curves, the vapor phase is favored for AO; BEP above the blue curves favor the formation of $ATiO_3$ from vapor-phase AO and solid $TiO_2$. Above the blue curve and below the red curve, one would expect $ATiO_3$ to form and for excess adsorbed AO species to re-enter the vapor phase. Regions shaded blue thus represent the growth window for the respective complex oxide.

materials lack utility as semiconductor transport layers, so the aforementioned advantages of MBE have a limited benefit in this regard.

Given the low vapor pressure of SrO and the limitations of standard (or even nominally oxygen-resistant) MBE equipment, the growth of SrTiO$_3$ by solid-source MBE is relegated to taking place outside the growth window. As such, Sr:Ti cation stoichiometry is determined entirely by the relative local fluxes of each constituent; any deviations from a 1:1 flux ratio correspond directly to cation nonstoichiometry. To obtain semiconductor-quality thin films with the concentration of defects from nonstoichiometry limited to the order of parts per million (~$10^{16}$ cm$^{-3}$ in SrTiO$_3$), the difference in cation flux would need to be controlled within 0.0001% of the total flux, which is highly impractical even with advanced flux monitoring techniques.

*2.3 Stoichiometry Optimization of SrTiO$_3$*

Despite the absence of a growth window, several methods have been developed or existing methods employed to optimize the stoichiometry of SrTiO$_3$ grown by solid-source MBE. Most involve *in-situ* monitoring of growth with reflection high-energy electron diffraction (RHEED), an indispensable tool for thin film growth in high vacuum conditions. Most also rely on corroboration with data from *ex-situ* characterization such as X-ray diffraction (XRD) and Rutherford backscattering spectrometry (RBS). A brief review of how various characterization methods have been employed to optimize the cation stoichiometry of SrTiO$_3$ will be given below.

One method employed by Haeni et al [58] involves tracking of the reflected RHEED beam intensity during the sequential deposition of SrO and TiO$_2$ layers to grow SrTiO$_3$

(001). The doses of each constituent monolayer were carefully controlled with a combination of atomic absorption spectroscopy (AAS [59]) and quartz crystal monitor measurements. The RHEED intensity during sequential deposition shows an oscillating pattern (increases with SrO deposition and decreases with $TiO_2$ deposition) that varies depending on the relative dosage. The authors find that the RHEED maximum intensity remains constant for stoichiometric conditions, while for Sr-rich and Ti-rich conditions, the maximum intensity will increase and decrease with subsequent oscillation periods, respectively [58]. Controlling the dose of each layer with a combination of flux monitoring and RHEED intensity profiles allows for stoichiometry to be controlled within the limits of RBS measurements (~1%).

Others concerned with the solid-source MBE growth of $SrTiO_3$ (001) on Si (001) [60] and $LaAlO_3$ (001) [61] have correlated changes in the RHEED pattern with stoichiometry. In both cases, the authors find that an excess of Sr is indicated by ½-order reflections along the <110> azimuths with only integral order reflections along <100> azimuths, which correspond to a c(2 × 2) surface reconstruction. For Ti-rich conditions, ½-order reflections are observed along the <100> azimuths but only integral order reflections are observed along <110> azimuths, which indicates a mixed-domain (2 × 1) and (1 × 2) surface reconstruction. The authors determine that stoichiometric growth conditions produce a (1 × 1) $SrTiO_3$ (001) surface, indicated by the absence of fractional-order reflections in the RHEED pattern. These observations hold true for both sequential deposition and codeposition, and stoichiometry is quantified within the limits of RBS.

The stoichiometry of $SrTiO_3$ thin films can also be determined by measurements of its lattice constant with high-resolution XRD. This method is predicated on the lattice

expansion of $SrTiO_3$ in both regimes of cation excess. Proposed mechanisms for lattice expansion involve the formation of SrO bilayers (a Ruddlesden-Popper type defect) in the Sr-rich regime, whereas in the Ti-rich regime, Sr vacancies form, leading to the mutual repulsion of O anions in nearby $TiO_6$ octahedra [62]. A stoichiometric $SrTiO_3$ thin film grown homoepitaxially on $SrTiO_3$ will produce an XRD spectrum with the peaks from the film overlapping with those from the substrate. Sufficient cation excess would lead to a shift in the film XRD peaks due to lattice expansion. Using XRD as a measure of stoichiometry can conceivably apply to heteroepitaxial growth of $SrTiO_3$ or related systems; in that case, the minimum lattice parameter would be indicative of stoichiometry, even without peak overlap, assuming all films are coherently strained and assuming that lattice expansion only comes from cation nonstoichiometry rather than alloying, for example. This latter point will be explored in the growth of $Ba_xSr_{1-x}TiO_3$ and $SrTi_{1-x}Zr_xO_3$, discussed in Chapters 4 and 5, respectively.

The methods described above allow for 1:1 Sr:Ti cation stoichiometry in solid-source MBE-grown $SrTiO_3$ on the order of a few percent, the measurement limit of more common compositional analysis techniques (e.g. RBS, XPS). The defect density for 1% off-stoichiometry in $SrTiO_3$ corresponds to $\sim10^{20}$ $cm^{-3}$, which is still far too large for high mobility transport and controlled doping to carrier densities on the order of the defect density or lower. Regarding the objectives of this dissertation, controlling the stoichiometry of a doped $SrTi_{1-x}Zr_xO_3$ barrier using solid sources alone is entirely impractical, especially given the necessity of controlling an additional flux from a highly refractory Zr source as well. As such, developing a new modulation-doped heterostructure for $SrTiO_3$ absolutely necessitates growth under conditions allowing self-regulated stoichiometry. The following

section will introduce metal-organic precursors as alternatives to solid sources for MBE growth, leading the way for a discussion on prior development of the hybrid MBE approach, which employs a combination of solid and metal-organic sources.

*2.4 Metal-organics for MBE*

The hybrid MBE approach addresses the issue of the low volatility of binary oxide constituents in complex oxides on the premise that if the vapor pressure of one of the binary oxide constituents were effectively increased, the growth window would then exist at more reasonable growth conditions. To this end, one can look to metal-organics (MO), a class of chemical compounds that have been studied extensively as precursors for binary oxide deposition in metal-organic chemical vapor deposition (MOCVD) and atomic-layer deposition (ALD) processes, for their higher vapor pressures as compared to their corresponding elemental metals.

A MO is a coordination complex with a central metal ion connected to organic functional group ligands via oxygen atoms, which is sometimes distinguished from an "organometallic," a label typically reserved for similar compounds (of considerable importance in III-V MOCVD) where the metal ion is bonded directly to the organic functional group [63]. β-diketonate chelate compounds [64-71] are one set of extensively studied and widely used MO compounds for both transition metals and alkaline earth metals (see Fig. 2.2a for an example). Homoleptic metal alkoxides [63, 68-76], a subset of MO compounds with the chemical formula $M(OR)_n$, where M is a metal ion and R is any of a number of organic functional groups, constitute many of the most extensively studied precursors for metal oxide growth (see Fig. 2.2b for an example).
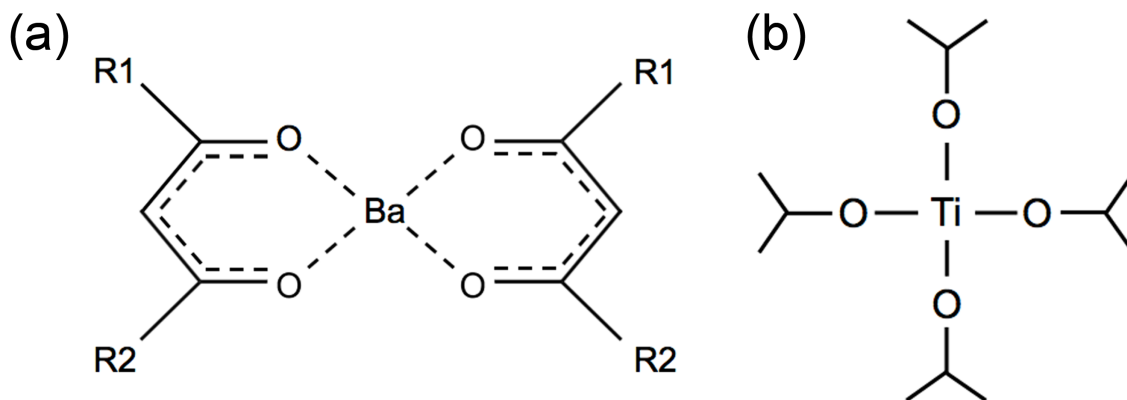
**Figure 2.2:** (a) Chemical structure of a typical β-diketonate chelate with a central Ba ion. R1 and R2 can be either identical or different organic functional groups. (b) The chemical structure of titanium (IV) tetra-isopropoxide (TTIP).

Although many MO compounds have been successfully utilized in MOCVD processes, those that are suitable for MBE growth comprise a much smaller set of compounds due to the special requirements of MBE growth. For instance, MOCVD typically relies on an inert carrier gas (e.g. $H_2$) to convey the precursor to the substrate. This would not be practical for MBE, where background pressures must be sufficiently low to maintain molecular beam conditions. Therefore, a suitable precursor for MBE must be conveyable without a carrier gas. In addition, the precursor must have sufficiently high vapor pressure to sustain sufficient flux for practical growth rates without exceeding the minimum temperature for thermal decomposition at the source. Furthermore, when the precursor arrives at the substrate and decomposes, the byproducts of the reaction must be sufficiently volatile such that they can be removed in a dynamic vacuum, minimizing the incorporation of carbon or other undesirable components of the MO into the growing film.

To better understand the requirements for MO precursors in MBE growth, it is informative to discuss the β-diketonates of Ba, which have been successfully implemented in MOCVD growth processes but have proven unsuitable for MBE growth. Several studies

have demonstrated the growth of Ba-based compounds from these precursors using a carrier gas; however, at temperatures required to get a sufficiently high flux (300-400 °C) without a carrier gas, Ba precursors invariably decompose at the source, leading to a build-up of residue [77]. To address this issue, some researchers have modified Ba precursors with fluorinated ligands to increase the vapor pressure at lower temperatures and prevent premature decomposition, though upon decomposing on the surface of the growing film, nonvolatile fluoride compounds may be incorporated into the film [78]. Residue from unfluorinated precursors builds up in MO vaporizers even in MOCVD systems that successfully utilize the precursors for oxide growth, and a solvent flush is necessary to clear the residue and thus maintain a stable working condition [70, 79]. This is not a viable solution for MBE growth, since periodic solvent flushes would compromise the integrity of the UHV conditions in the growth chamber. Ba β-diketonates thus do not satisfy most of the criteria necessary for implementation in MBE.

In contrast to the previous example, titanium tetra-isopropoxide (TTIP), a homoleptic metal alkoxide, does satisfy the criteria for precursors in MBE, and has proven to be instrumental in the development of hybrid MBE. The molecular structure consists of a central $Ti^{4+}$ cation bonded to four isopropyl groups via oxygen. The vapor pressure of TTIP is approximately 100 mTorr at 49 °C [80], which is sufficiently high at a temperature far below its minimum temperature for decomposition, ~ 260 °C [81]. This allows the precursor to be delivered without a carrier gas while avoiding the deposition of residue at the source or in the growth chamber. In addition, the byproducts of TTIP, which include water, alkenes, and alcohols [81], are all highly volatile, thus contamination from MO byproducts is

minimized. TTIP can thus be expected to perform reliably if implemented as a MBE gas source.

The MBE growth of oxides from MO precursors (i.e. MOMBE) has been demonstrated previously for both binary oxides [78, 82-84] as well as thin films of more chemically complex high-$T_c$ superconductors [77, 85]. In most cases, the precursor was used as a means to increase the vapor pressure of the source material to get a higher, more stable flux from the effusion cell, rather than as a method to open a growth window. Incidentally, this led to the earliest published reports of hybrid MBE growth, in which MO precursors for Dy and Y were used in conjunction with solid sources for Ba and Cu to grow high-$T_c$ superconductors [85]. As such, selectively replacing solid sources with MO precursors in a HMBE approach was shown to be feasible for the growth of high-quality thin films, even if semiconductor-quality stoichiometry control was not necessarily the primary goal.

Given that a hybrid MBE approach is a feasible one, it is also desirable in some cases over using MO precursors alone. Hypothetically, the adsorption-controlled growth of complex oxides could be achieved with MOMBE, without the need for solid sources. However, suitable precursors for certain elements have not yet been developed to meet the criteria for MBE growth, as is the case for Ba and Sr, whose precursors have shown little promise for MBE growth even with substantial effort put forth to mitigate unfavorable characteristics [66]. Solid sources for Ba and Sr are readily available and can provide a reasonably stable flux, even at moderate oxygen background pressures [86], in contrast to solid sources for Ti, for example, which suffer from low vapor pressures and reactivity between the source material and its crucible at elevated temperatures [87]. Furthermore, adsorption-controlled growth of a ternary oxide (quaternary or higher order oxides are not

considered for the sake of simplicity and relevance to the thesis topic) only requires that one of the binary oxide constituents be volatile, so in the case of $SrTiO_3$ growth by hybrid MBE, supplying Sr via a solid source and Ti via a MO precursor should constitute an effective configuration for adsorption-controlled MBE growth.

As long as one of the binary oxide constituents is sufficiently volatile to open a growth window under practical growth conditions, the choice between using a solid source or MO precursor for a particular element in a hybrid MBE configuration can be determined by source or precursor availability and performance. The issue of choosing one or the other type of source becomes particularly relevant in the hybrid MBE growth of perovskite alloy systems, such as the $SrTi_{1-x}Zr_xO_3$ and $Ba_xSr_{1-x}TiO_3$ systems to be explored in this dissertation. Since both systems are solid solutions with random substitution on one type of site (B- and A-sites, respectively), and since control of same-site stoichiometry is not as critical, though still of much significance, to the desired materials properties as the A:B site stoichiometry, either solid source or MO sources can be utilized to add an alloying element. For example, if a Zr solid source were to be used in conjunction with a Ti MO precursor to grow the alloy system $SrTi_{1-x}Zr_xO_3$, the growth window would not be compromised as long as excess TTIP desorbs to maintain a 1:1 A:B site stoichiometry. Its use as a doped barrier is predicated on the assumption that the Zr substitution can vary on the order of a few percent (as would be expected from a solid source) and still allow n-type doping, which is not the case for A:B nonstoichiometry of that magnitude. Later in this chapter, the use of a Zr MO precursor will be justified as the preferred approach over a solid source for the $SrTi_{1-x}Zr_xO_3$ alloy system. Because of the lack of suitable precursors for Ba as discussed in this section, a

solid source for Ba will be used together with a solid source for Sr in the growth of $Ba_xSr_{1-x}TiO_3$.

*2.4.1 Deposition Kinetics of Metal Oxides from Metal-organic Precursors*

To better understand the role of MO precursors in opening a growth window, a discussion of the deposition kinetics of metal oxides from metal-organics is necessary. The study of the conversion of MO compounds into metal oxides comprises a sizeable library of research, spurred in large part by the ability to grow oxide thin films at low temperatures and with solution-based methods [80].The conversion invariably involves removing the organic constituents from the precursor to form the metal oxide and gaseous byproducts, a chemical reaction which can be generally represented (for a homoleptic metal alkoxide) as:

$$M(OR)_n \rightarrow MO_x + byproducts_{(g)} \tag{1}$$
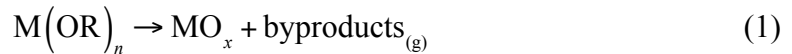
The specific byproducts released by the reaction depend on the configuration of the MO precursor molecule [75]. This reaction describes the simplest case in which the MO decomposes via pyrolysis, although hydrolytic reactions [88] have also been studied extensively. Since this chapter is concerned with MO precursor implementation for MBE, where great care is usually taken to minimize the amount of water vapor in the growth chamber, hydrolysis is of limited relevance, and as such the focus will remain on pyrolytic reactions. It should be noted that in reality, the reaction described in Eqn. (1) takes place in a number of steps [88], but the simplified expression suffices for the following discussion of growth kinetics.

A thorough investigation of the growth kinetics of $TiO_2$ from MO precursors TTIP and titanium (IV) nitrate was performed by Taylor et al [76], whose results can be generalized to

31

any arbitrary vapor-phase precursor. To explain the observed changes in growth rate with temperature, their model describes the deposition of a binary oxide $MO_x$ as a two-step process, involving the reversible adsorption of a precursor species P and the subsequent pyrolysis of the adsorbed precursor:

$$P_{(g)} \Leftrightarrow P_{(ad)} \tag{2}$$

$$P_{(ad)} \rightarrow MO_x + byproducts_{(g)} \tag{3}$$

It should be noted that the precursor species P may differ from the precursor molecule $M(OR)_n$ in equation (1). This distinction is made to generalize the process to instances where the adsorbed precursor species may be altered from the original molecule during the process of adsorption. Equations (3) and (1) can therefore be identical in a number of cases, but equation (3) is more generally applicable.

The schematic diagram presented in Fig. 2.3 illustrates the process of binary oxide deposition from a MO precursor, with the rate-determining steps labeled in red text. If one assigns the rate constants $k_a$, $k_d$, and $k_r$ for the rate-determining processes of adsorption, desorption, and reaction, respectively, Taylor et al show that the growth rate (R) of the binary oxide from a MO precursor can be described as:

$$R = \frac{k_r Z_P S_P^0}{\left(Z_P S_P^0 / \Theta_P^0\right) + k_d + k_r}, \tag{4}$$

where $Z_p$ is the rate at which precursor molecules impinge onto the growth surface (related to the precursor flux); $S_P^0$ is the probability that an impinging precursor molecule will adsorb on the surface if no previously adsorbed precursor is present (i.e. with zero coverage); and $\Theta_P^0$ is the total number of sites available for precursor adsorption [76]. The
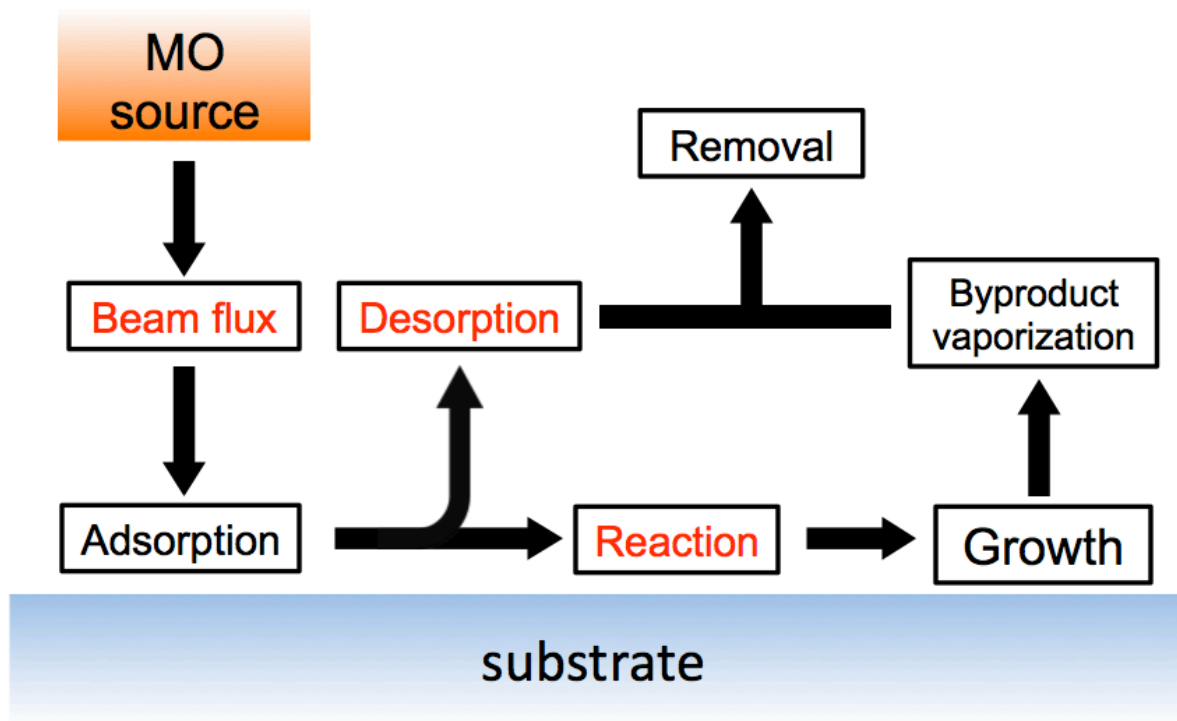
32

**Figure 2.3:** Flow chart depicting the process of binary oxide deposition from a MO precursor. Rate-limiting steps are labeled with red text.

growth rate R is temperature dependent via the Arrhenius temperature dependence of the rate constants:

$$k_i = A_i \exp\left(\frac{-E_{a,i}}{k_b T}\right),$$  (5)

where $A_i$ is the reaction frequency factor and $E_{a,i}$ is the activation energy for the reactions with $i$ = a, d, or r. Thus the growth rate is expected to change with temperature as the rate constants for each process vary in accordance with their respective activation energies.

Above the minimum temperature for decomposition, Taylor et al [76] observe three kinetic regimes of growth from a precursor, as shown in Fig. 2.4. These kinetic regimes have also been observed for the MOCVD growth of III-V semiconductors [49]. Below the minimum temperature for decomposition, the precursor molecule is thermally stable, as the rate of reaction is so low so as to yield a negligible growth rate. As the temperature increases, the reaction rate constant becomes significant, but the rate of reaction (and desorption) are negligible compared to the rate of adsorption, giving $\left(k_d + k_r\right) << \left(Z_P S_P^0 / \Theta_P^0\right)$, where the latter term is related to the rate of adsorption. For a range of temperatures in which this holds true, there is full coverage of the surface with unreacted precursor, and Equation 4 can be simplified to give the approximation:

$$R = k_r \Theta_P^0$$  (6)

This describes the growth rate in the range of temperatures known as the reaction-limited regime, since the growth rate only depends on the rate at which the precursor decomposes (as well as the number of sites available for precursor adsorption, which is independent of temperature in this case), and as such the growth rate increases with increasing temperature.

34

When the temperature increases further, eventually the rate of reaction exceeds both the rate of adsorption and desorption. Under these conditions, $k_r \gg \left( Z_P S_P^0 / \Theta_P^0 \right) + k_d$, and the growth rate can be approximated from Equation (4) as:

$$R = Z_P S_P^0 \tag{7}$$

The growth rate thus depends only on the rate of impingement of precursor molecules on the growing surface. This is known as the flux-limited or mass transport-limited regime [49]. For a given flux, the growth rate is constant for the range of temperatures where these conditions hold.

At the highest temperatures, desorption of the unreacted precursor limits the growth rate, i.e. $k_d \gg \left( Z_P S_P^0 / \Theta_P^0 \right) + k_r$, and the growth rate can be approximated as:

$$R = \frac{k_r}{k_d} Z_P S_P^0 \tag{8}$$

In this desorption-limited regime, the growth rate is *limited* by desorption but is determined by the precursor flux and reaction rate as well. In terms of temperature dependence, this means that the growth rate may either increase or decrease depending on the relative activation energies of reaction and desorption [76]. In the case of TTIP, the growth rate decreases with increasing temperature in the desorption-limited regime, as shown in Fig. 2.4, because the activation energy for desorption is greater than that of reaction.

Since the existence of a growth window in hybrid MBE is predicated on the desorption of excess unreacted precursor species, it is expected that the growth window will only open in the desorption-limited regime. It is assumed that the nonvolatile component has negligible vapor pressure compared to the volatile metal-organic; otherwise the adsorption-

controlled growth regime for a complex oxide would be complicated by desorption of the second constituent. This assumption holds for SrTiO$_3$ with regard to SrO volatility, as was covered in previous sections. As such, the study of the kinetics of oxide deposition from MO precursors allows for some insight into the growth conditions necessary to achieve a growth window in hybrid MBE for SrTiO$_3$ and related compounds.
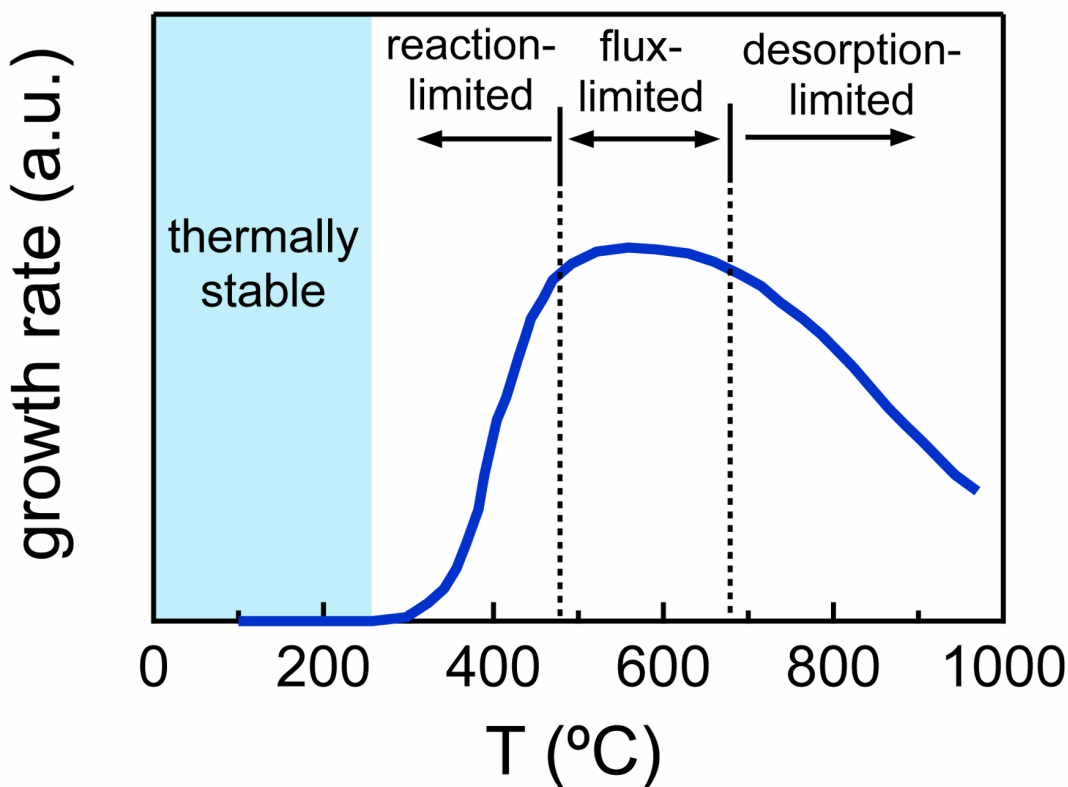


**Figure 2.4:** Growth rate of TiO$_2$ from the pyrolysis of TTIP in a low-pressure CVD reactor. Three kinetic regimes of deposition and the thermally stable regime at lower temperatures are labeled. Adapted with permission from [76]. Copyright 1999 American Chemical Society.

*2.5 Hybrid MBE Growth of SrTiO₃*

The practical implementation of a hybrid MBE technique combining an MO precursor and an elemental solid source, specifically for the purpose of opening an adsorption-controlled growth regime (growth window) under practical growth conditions, was first demonstrated for $SrTiO_3$. Initial studies [55, 89] investigated the homoepitaxial growth of $SrTiO_3$ on $SrTiO_3$ (001) single-crystal substrates, using TTIP as an MO precursor for the $TiO_2$ binary oxide constituent. Unlike in solid-source MBE, an additional oxygen source is not necessary to grow high-quality $SrTiO_3$ by hybrid MBE [23], since the TTIP precursor molecule already contains a sufficient number of oxygen atoms bonded to the central $Ti^{4+}$ cation per precursor molecule. However, the first hybrid MBE-grown films were grown in an oxygen plasma background to modulate the breakdown of TTIP with varying beam-equivalent pressures of oxygen [55].

The growth window in hybrid MBE-grown $SrTiO_3$ thin films was initially demonstrated through XRD measurements of the film lattice parameter [55], which is indicative of the Sr:Ti cation stoichiometry as was discussed in previous sections. As shown in Fig. 2.5, at substrate temperatures of 700 °C and above, a range of TTIP/Sr beam-equivalent pressure ratios exists such that the resulting thin film lattice parameter matches that of the substrate. This range of growth conditions constitutes a growth window insofar that matching substrate and film lattice parameters are indicative of stoichiometric films, which are indistinguishable by XRD, grown with substantially different relative cation fluxes. The broadening of the growth window and its shift towards higher TTIP/Sr beam-equivalent pressure ratios suggests that the self-regulating stoichiometry is effected
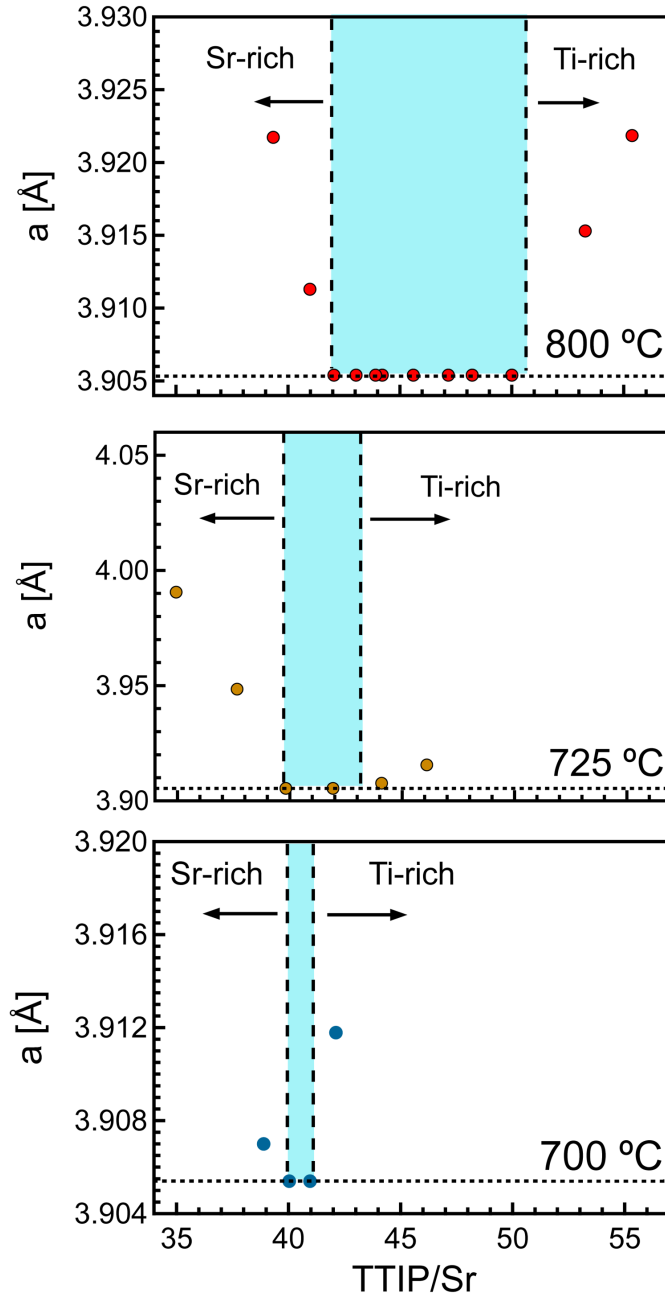
**Figure 2.5:** Out-of-plane lattice parameter of $SrTiO_3$ thin films on $SrTiO_3$ (001) substrates at various TTIP/Sr beam-equivalent pressure ratios and at different temperatures. All films shown here were grown in an RF oxygen plasma (250 W, $8 \times 10^{-6}$ Torr). The bulk lattice parameter of cubic $SrTiO_3$ (at room temperature) is marked by a dotted line for each data set. Adapted with permission from [55]. Copyright 2009, AIP Publishing LLC.

primarily by the desorption of excess TTIP. This is also corroborated by the opening of the

window at 700 °C, the approximate onset of the desorption-limited regime for TTIP.

The cation stoichiometry of $SrTiO_3$ films grown within the growth window was also

corroborated by energy positron annihilation spectroscopy (VE-PALS). With this technique,

cation-site defect concentrations in La-doped $SrTiO_3$ films grown by MBE were found to be

on the order of 2 ppm [90]. By contrast, $SrTiO_3$ films grown by pulsed laser deposition

contained an order of magnitude higher concentration of cation-site defects, ~50 ppm [91].

The low energy of deposition for MBE-grown films and the self-regulating stoichiometry of

a growth window thus allow for much lower defect densities than can be achieved by more

typical high-energy deposition techniques.

The transport properties of La-doped hybrid MBE-grown $SrTiO_3$ also attest to the

superior stoichiometry of thin films grown within the growth window. For instance, a 1:1

correlation between La dopant concentration (measured by secondary ion mass

spectroscopy, or SIMS) and charge carrier concentration (determined by Hall effect

measurements) can be shown for films doped as low as $5 \times 10^{17}$ $cm^{-3}$ [92]. This suggests that

the density of any defects involved in charge-carrier trapping must be substantially lower

than the lowest dopant concentration, which is supported by data from VE-PALS that places

cation defect concentrations on the order of $10^{16}$ $cm^{-3}$. The electron mobility of hybrid MBE-

grown La-doped $SrTiO_3$ thin films also far exceeds that of thin films grown by other

techniques and even that of bulk single crystals, reaching values of 30,000 $cm^2V^{-1}s^{-1}$ at 2 K

[92] in early studies and more recently exceeding 50,000 $cm^2V^{-1}s^{-1}$ at 2 K [93] with growth

at higher substrate temperatures. Given the superior transport properties of these thin films,

hybrid MBE stands as the preferred method for growing $SrTiO_3$ transport layers for studies of high-mobility systems in complex oxides.

So far, it has been shown that the growth window, as defined by XRD measurements of the film lattice parameter, allows for unprecedented stoichiometry control of the complex oxide $SrTiO_3$. There are, however, some limitations to the use of XRD as the main tool for stoichiometry optimization. For one, cation nonstoichiometry can only be detected to the extent that it produces a detectable peak shift in the spectrum. Second, the analysis of XRD data becomes increasingly difficult when more complicated heterostructures (such as those designed for modulation doping) are being studied or once different substrates are being used. It is therefore beneficial to revisit *in-situ* RHEED characterization for the purpose of stoichiometry optimization, as will be discussed in more detail in Chapter 3.

*2.6 Hybrid MBE Growth of SrTi$_{1-x}$Zr$_x$O$_3$*

The previous section presented background information about the development of hybrid MBE for the purpose of improving the cation stoichiometry in $SrTiO_3$, with discussions about further improvements deferred to subsequent chapters. Optimizing the stoichiometry of the transport layer is crucial to successful mobility enhancement by modulation doping, as is the development of the doped barrier layer. Addressing the latter point requires Zr substitution on Ti sites to produce $SrTi_{1-x}Zr_xO_3$, creating a doped barrier layer with a significant conduction band offset.

Using a Zr solid source for the growth of $SrTi_{1-x}Zr_xO_3$ can be problematic due to the low vapor pressure of Zr, which is even lower than that of Ti. The temperature necessary to give a vapor pressure of $10^{-2}$ Torr for Zr is 2450 °C, compared to 1740 °C for solid Ti [94], and

the low vapor pressure of Ti has even proven troublesome for the growth of titanates from a solid source [87]. Electron beam-evaporated Zr sources have been used to grow $SrZrO_3$ by MBE in a layer-by-layer growth mode [95] and as such are viable for Zr evaporation. However, in this case, one still encounters the issue of MBE growth with another nonvolatile binary oxide constituent, $ZrO_2$, precluding the existence of a growth window for $SrZrO_3$. The extremely low vapor pressure of $ZrO_2$ may not be an issue for the adsorption-controlled growth of $SrTi_{1-x}Zr_xO_3$, since the A:B stoichiometry can still be regulated by desorption of excess TTIP despite variations in the Zr flux. In spite of this, there is sufficient motivation to implement a MO precursor for Zr.

One MO precursor for Zr, zirconium *tert*-butoxide (ZTB, $Zr[OC(CH_3)_3]_4$), stands as an attractive candidate for realizing the growth of $SrTi_{1-x}Zr_xO_3$. ZTB has already been shown to satisfy the compatibility criteria for MBE growth in the growth of $ZrO_2$ on III-V semiconductors [96]. The vapor pressure of ZTB [97] and the minimum decomposition temperature of ZTB [73] are similar to those of TTIP [80], allowing it to be integrated into an MBE system using similar equipment proven effective for the growth of $SrTiO_3$. Similar to TTIP, the CVD growth of $ZrO_2$ from ZTB exhibits 3 kinetic regimes versus temperature: reaction-, flux-, and desorption-limited (see Fig. 2.6). Given the advantages of improved volatility (for either increased growth rate or the opening of a growth window) of MO precursors, and since an MBE-compatible precursor already exists for Zr, the hybrid MBE growth of $SrTi_{1-x}Zr_xO_3$ will be realized with MO precursors for both Ti and Zr, along with a solid source for Sr. Details and results of the growth will be discussed in Chapter 5.
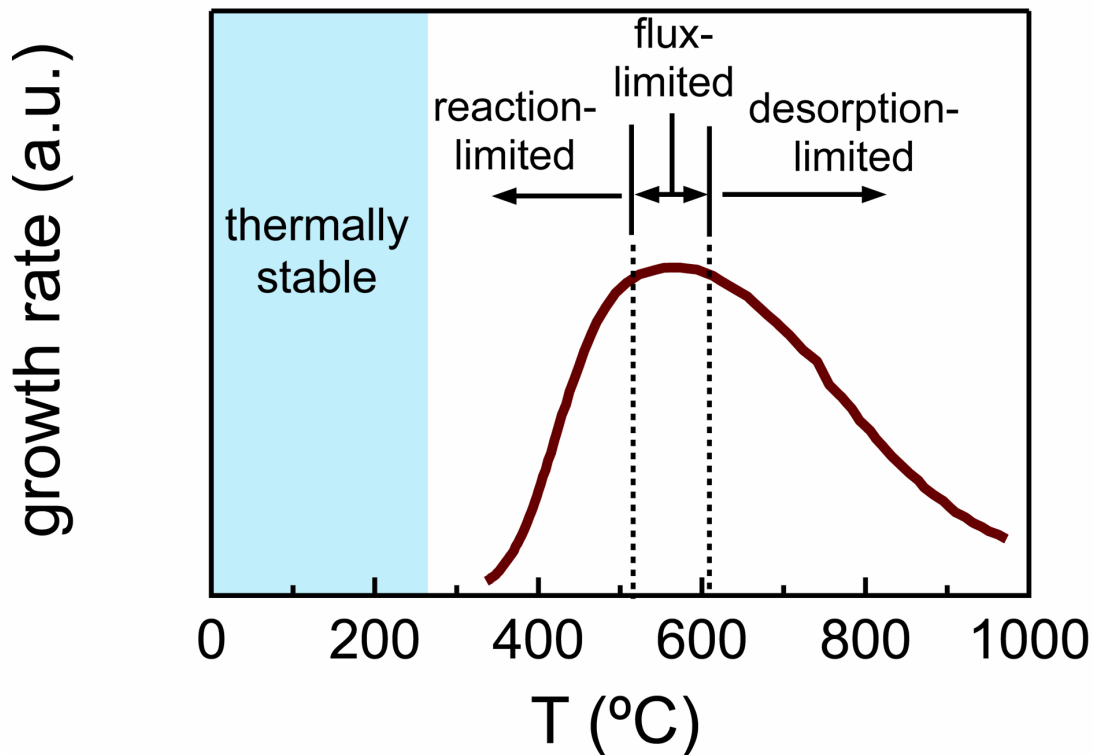
**Figure 2.6:** Growth rate of $ZrO_2$ from the pyrolysis of zirconium *tert*-butoxide (ZTB) in a low-pressure CVD reactor. The approximate boundaries of three kinetic regimes of deposition and the thermally stable regime at lower temperatures are labeled. Adapted with permission from [73] Copyright 2002 American Chemical Society.

*2.7 Chapter Summary*

In this chapter, the development of a hybrid MBE approach was motivated by the necessity of growing electronic transport-quality complex oxides in an adsorption-controlled growth regime (i.e. growth window) at practically attainable growth conditions. Substituting solid sources with a more volatile MO precursor opens a growth window wherein stoichiometry is regulated by the desorption of excess precursor at temperatures within a desorption-limited kinetic regime. Previous efforts in the hybrid MBE growth $SrTiO_3$ with a MO precursor for Ti, TTIP, successfully demonstrated a growth window for $SrTiO_3$ observed with XRD peak overlap for the film and substrate. Although stoichiometry optimization by XRD has proven useful for substantially improving the transport properties

of SrTiO$_3$ thin films, revisiting *in-situ* RHEED characterization as a more sensitive method

for stoichiometry optimization of SrTiO$_3$ was motivated, and the relevant results and

discussion deferred to Chapter 3. The precursor ZTB was also introduced as the preferred Zr

source for the hybrid MBE growth of SrTi$_{1-x}$Zr$_x$O$_3$, to be discussed in more detail in Chapter

5.

# Chapter 3

Surface Reconstructions and Stoichiometry in SrTiO$_3$ Grown by Hybrid Molecular Beam Epitaxy

*3.1 Introduction*

Chapters 1 and 2 motivated the development of highly stoichiometric $SrTiO_3$ as the transport channel in modulation-doped complex oxide heterostructures and provided background on the development of the hybrid MBE approach as a means to address inherent difficulties in the MBE growth of complex oxides, respectively. The growth of $SrTiO_3$ by the codeposition of Sr from a solid source and Ti from a MO precursor, TTIP, was shown to open a growth window at practical growth conditions defined by a range of TTIP/Sr beam-equivalent pressures in which the film lattice parameter (as measured by XRD) is equal to the lattice parameter of the $SrTiO_3$ (001) substrate. Although stoichiometry optimization by XRD has proven effective in the growth of high-mobility homoepitaxial $SrTiO_3$ thin films, its utility in optimizing the growth of heterostructures is limited. *In-situ* RHEED characterization has been used extensively to track the surface stoichiometry in the MBE growth of a wide variety of semiconductor systems, including $SrTiO_3$ grown by solid-source MBE (without a growth window). In this chapter, RHEED will be shown to be a sensitive probe of the surface stoichiometry (and thus the resulting bulk stoichiometry) of hybrid MBE-grown $SrTiO_3$ thin films within the growth window. The results presented in this chapter were published elsewhere [98].

*3.2 Experimental Details*

The $SrTiO_3$ thin films that are the focus of this chapter were grown homoepitaxially on $10 \times 10 \times 0.5$ mm$^3$ $SrTiO_3$ (001) single crystal substrates (MTI Corporation). Growth was performed in a VEECO GEN930 MBE reactor configured for hybrid MBE, identical to the experimental setup used in earlier studies of hybrid MBE growth of $SrTiO_3$ [55, 89]. Sr

(99.99% purity, Sigma-Aldrich) was supplied via a low-temperature, oxygen-resistant (VEECO) solid source effusion cell; Sr was melted into a Ti crucible in an inert atmosphere prior to installation in the effusion cell. Ti was delivered via the metal-organic precursor, titanium (IV) tetra-isopropoxide (TTIP, 99.999% purity, Sigma-Aldrich). The TTIP delivery system consists of a bubbler containing liquid TTIP heated to 60 °C, from which vapor is delivered to a low-temperature gas source in the MBE growth chamber through stainless steel tubing (heated to ~100 °C to prevent condensation without thermally decomposing the precursor). The flux of the precursor is regulated by a linear leak valve with feedback from a Baratron capacitance manometer located forward of the valve. The beam-equivalent pressure of the precursor is measured by a beam-flux ion gauge (typically located on the sample manipulator opposite the sample block) and calibrated with respect to various delivery line pressures maintained by the valve-manometer feedback loop. *TTIP/Sr* beam-equivalent pressure (BEP) ratios were adjusted by fixing the *Sr BEP* at $5 \times 10^{-8}$ Torr and adjusting the *TTIP BEP*.

Substrate temperatures were measured during growth using an Ircon Modline 3 optical pyrometer. Prior to the beginning of growth, substrates were subjected to a 20 min cleaning step at growth temperature in the growth chamber in an oxygen plasma delivered by an RF plasma source operating at 250 W and a pressure of $4 \times 10^{-6}$ Torr measured at the beam-flux ionization gauge, which is facing away from the source. The same oxygen plasma conditions were maintained during growth as well as the post-growth cooldown until the substrate cooled below 400 °C. Film thicknesses varied between 60 and 100 nm as determined from RHEED intensity oscillations at the beginning of growth.

A Staib Instruments RHEED system operating *in-situ* with an accelerating voltage of 14 kV was used to record RHEED images for each sample after the post-growth cooldown. It should be noted that the observed surface reconstructions do not change during cooldown. RHEED intensity was measured for the 00 and 10 reflections of SrTiO$_3$ (001) at the beginning of growth. *Ex-situ* high-resolution XRD 2θ-ω on-axis scans of the films were performed in the vicinity of the 002 reflection of SrTiO$_3$ using a Philips X'Pert Panalytical Pro Thin Film Diffractometer to determine the out-of-plane lattice parameters of the films.

*3.3 Evolution of the Surface Reconstruction Within the XRD Growth Window*

RHEED patterns captured along the [100] and [110] azimuths of samples grown at a substrate temperature of 810 °C are shown in Fig. 3.1. The observed patterns along each azimuth are four-fold symmetric for all samples in this study; no qualitative differences were found for 90° in-plane rotations. The samples represented in Fig. 3.1 all fall within the XRD growth window, except for the one grown at TTIP/Sr = 60.0, which is slightly Ti-rich. For the film grown at TTIP/Sr = 37.5, only integer-order reflections are observed, consistent with a (1 × 1) unreconstructed surface lattice. For a slightly increased TTIP flux, at TTIP/Sr = 39.5, ½-order reflections become apparent only along the <100> azimuths. Because of the four-fold symmetry of the patterns, this indicates that both (1 × 2) and (2 × 1) reconstructed surface lattice domains are present on the surface. As the TTIP flux is increased further, giving TTIP/Sr = 45.0, the ½-order reflections along the <100> azimuths persist (and are more pronounced), and ¼-order reflections are observed along the <110> azimuths. This pattern is indicative of a c(4 × 4) reconstructed surface lattice. The c(4 × 4) lattice persists even to slightly Ti-rich conditions (as shown for TTIP/Sr = 60.0, though dim ¼-order

47

RHEED beam incidence:
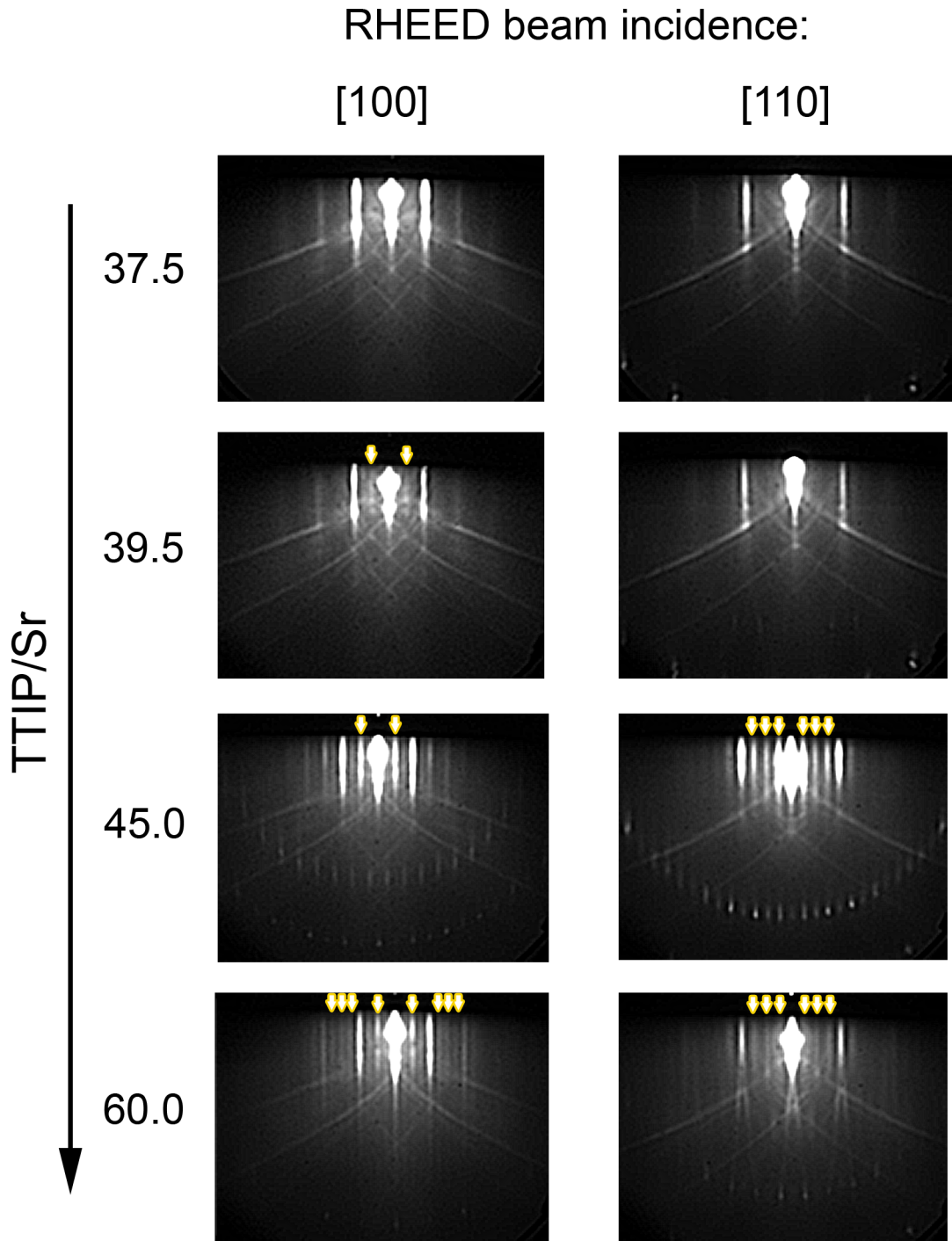
[100]                    [110]



**Figure 3.1:** RHEED images captured along the [100] and [110] azimuths of SrTiO$_3$ thin films grown at various *TTIP/Sr BEP* ratios at a substrate temperature of 810 °C. Adapted with permission from [98]. Copyright 2014, AIP Publishing LLC

reflections begin to appear along the <100> azimuths, accompanied by well-defined

chevrons along the <110> azimuths. This pattern is consistent with the coexistence of c(4 ×

4) with mixed (1 × 4) and (4 × 1) domains similar to anatase $TiO_2$ grown on $SrTiO_3$ (001)

[99].

The surface lattices observed in samples grown at 810 °C and 850 °C at various TTIP/Sr

BEP ratios are plotted in Fig. 3.2 along with the measured out-of-plane lattice parameters at

each growth condition. The growth window as defined by XRD film-substrate peak overlap

is marked for both temperatures. The evolution of the surface lattice with TTIP/Sr BEP ratio

at 850 °C is consistent with that described for samples grown at 810 °C. Surface

reconstructions observed outside the XRD window are also labeled. The (2 × 1) surface

reconstruction is labeled according to what is observed in the RHEED pattern and as such

(2 × 1) surface lattices observed inside the XRD window are not distinguished from those

observed outside the window. However, the implications for surface and bulk stoichiometry

are different for each case, as will be discussed in the following sections.


*3.4 Surface Lattices Observed Outside the XRD Growth Window*

Before exploring the significance of the surface lattice evolution within the XRD

window, it is helpful to compare the RHEED patterns observed outside the growth window

with those observed by other researchers in the growth of $SrTiO_3$ with solid-source MBE.

Figure 3.3 shows RHEED patterns of hybrid MBE-grown $SrTiO_3$ thin films exemplifying

surface reconstructions observed in the Sr-rich and Ti-rich regimes. The (2 × 1)

reconstructed lattice evidenced by ½-order reflections along the [100] azimuth in Fig. 3.3a

has been previously associated with growth in the Ti-rich regime [60, 61]. This is consistent
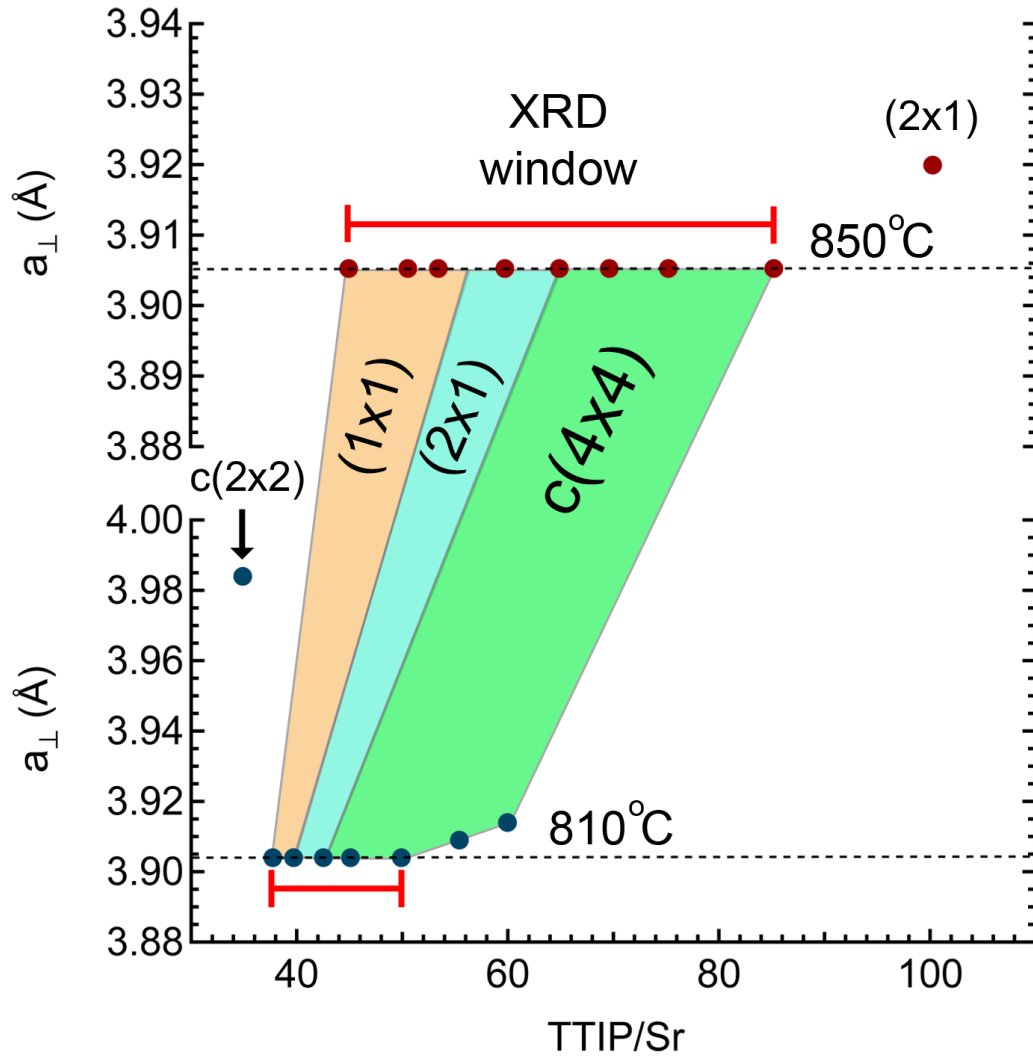
**Figure 3.2:** Surface lattices observed by *in-situ* RHEED for $SrTiO_3$ (001) thin films grown at 810 °C and 850 °C at various *TTIP/Sr BEP* ratios, along with the out-of-plane lattice parameters of each film measured by *ex-situ* XRD. The $(2 \times 1)$ label for surface reconstruction refers to a multi-domain $(2 \times 1)$ and $(1 \times 2)$ reconstructed surface. The horizontal dashed lines mark the lattice parameter of bulk, cubic $SrTiO_3$ at room temperature. Adapted with permission from [98]. Copyright 2014, AIP Publishing LLC

**Figure 3.3:** RHEED images captured along the [100] and [110] azimuths of SrTiO$_3$ thin films grown (a) at a substrate temperature of 850 °C, *TTIP/Sr* = 100.0 (Ti-rich), and (b) at a substrate temperature of 810 °C, *TTIP/Sr* = 35.0 (Sr-rich).

with the growth conditions for this sample (850 °C, TTIP/Sr = 100.2, compare to Fig. 3.2), which place the sample outside the growth window into regime of Ti excess. The c(2 × 2) reconstructed lattice indicated by ½-order reflections along the [110] azimuth in Fig. 3.3b has been similarly associated w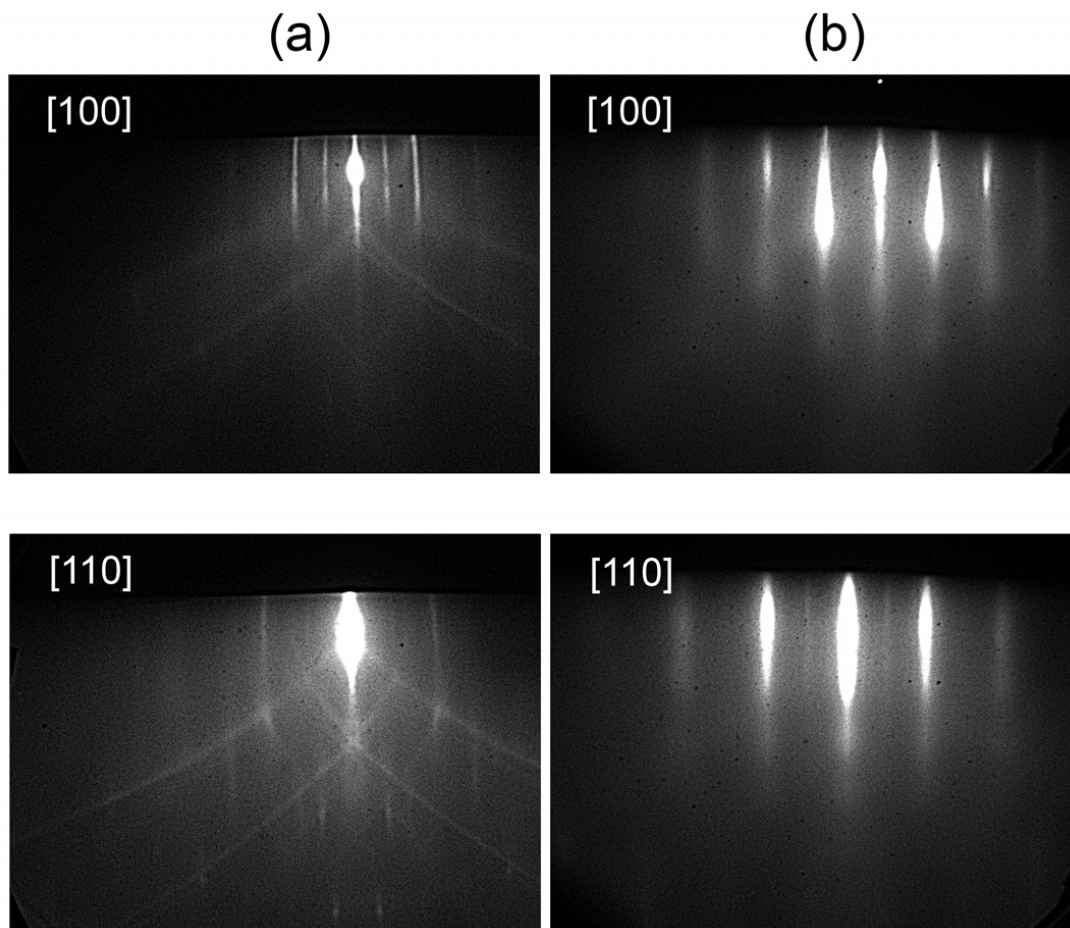ith Sr excess in previous studies [60, 61] and is consistent with the growth conditions of the sample (810 °C, *TTIP/Sr* = 35.0, compare to Fig. 3.2).

A (1 × 1) surface may also be observed in either regime of cation excess. In the Ti-rich regime, this is typically characterized by narrower streaks and a diffuse background, likely the result of amorphous $TiO_x$ forming on the surface [100]. In the Sr-rich regime, the background also becomes more diffuse, and the pattern along the [100] azimuth exhibits "bulging" in the first-order diffraction streaks (somewhat evident in Fig. 3.3b). Extreme cases of cation excess will lead to a spotty RHEED pattern resulting from the deposition of three-dimensional crystallites of SrO or $TiO_2$ on the surface.

Since the surface lattices observed by RHEED for hybrid MBE-grown $SrTiO_3$ (001) thin films grown outside the growth window are consistent with what is observed for films grown by solid-source MBE, one can consider the evolution of the surface reconstruction within the growth window as a trend whose study is uniquely enabled by the hybrid MBE growth technique. It is also clear from Fig. 3.2 that XRD measurements of the lattice parameter within the growth window are ineffective in capturing the changing nature of the surface and potentially the bulk stoichiometry of the resulting films in this range of growth conditions. Therefore, the following sections will look to RHEED as a sensitive probe of the surface, and comparisons with the literature will inform the analysis of the trend in surface reconstructions.

*3.5 Surface Reconstructions and Stoichiometry Inside the XRD Growth Window*

To better understand the changing nature of the surface of hybrid MBE-grown $SrTiO_3$ thin films, one may look to the literature for studies of surface reconstructions in bulk $SrTiO_3$ single crystals. Multiple studies have investigated surface reconstructions on bulk $SrTiO_3$ using scanning tunneling microscopy (STM) [101-103] low-energy electron diffraction (LEED) [102-104], and RHEED [105]. Unlike in MBE, where the surface has been observed to change depending on the relative flux of each constituent, changes in the surface reconstruction in bulk specimens were realized by annealing in vacuum, oxygen, or hydrogen [101, 103-106]. One study investigates changes in the surface reconstruction after deposition of fractional monolayers of Sr (from an effusion cell) and Ti (from an electron beam evaporator) onto bulk single-crystal $SrTiO_3$ (001), followed by annealing [102].

For $SrTiO_3$ (001), which can be described with alternating SrO and $TiO_2$ layers along the growth direction, a $(1 \times 1)$ surface was found to be indicative of a surface with approximately equal fractions of SrO and $TiO_2$ termination. A multi-domain $(2 \times 1)$ and $(1 \times 2)$ reconstructed lattice has been observed in both $TiO_2$ saturated surfaces and mixed-termination surfaces with a majority $TiO_2$ termination. Higher order reconstructions, such as $c(2 \times 4)$, $c(4 \times 4)$, and $c(2 \times 6)$, consist of a Ti-O network on the surface exclusive to $TiO_2$-saturated surfaces.

Comparing these results with the observed surface reconstructions in the growth window, the $(1 \times 1)$ surface regime at lower TTIP/Sr BEP ratios corresponds to a mixed termination surface that yields a film with bulk stoichiometry within the limit of XRD measurements. Increasing the relative TTIP flux results in a multi-domain $(2 \times 1)$ surface, where the reconstructed portions consist of expanding regions of $TiO_2$ termination, though

the surface remains SrO-terminated in uniformly distributed areas. This is distinct from the

$(2 \times 1)$ reconstruction in the Ti excess regime, in which the surface is completely $TiO_2$-

saturated. A further increase in the relative flux of TTIP results in a $c(4 \times 4)$, indicative of a

$TiO_2$-saturated surface. As such, the crossover point from a multi-domain $(2 \times 1)$ to a $c(4 \times$

4) reconstructed surface represents the growth conditions under which sufficient TTIP is

supplied to transition from a mixed termination surface to a purely $TiO_2$-terminated surface.

The shifting of this point to higher *TTIP/Sr BEP* values at higher temperature is consistent

with the more rapid desorption of TTIP at higher temperatures.

The crossover from a mixed surface termination to a purely $TiO_2$-terminated surface can

also be observed through a change in the RHEED intensity oscillations at the beginning of

growth.  Figure 3.4 shows the RHEED intensity oscillations from the specular (i.e. 00) and

10 diffracted beams measured for samples grown at 810 °C at various *TTIP/Sr BEP* ratios.

For *TTIP/Sr* below the crossover point ($42.5 <$ *TTIP/Sr* $< 45$), a phase shift in the

oscillations of the specular intensity can be seen at approximately 5 oscillation periods after

the beginning of growth, placing the 00 oscillations approximately $\pi$ rad out-of-phase with

the 10 oscillations. This phase shift is not observed above the crossover, where the 00 and

10 oscillations remain approximately 0 to $\pi/2$ rad out of phase. This is the case even for

growth conditions slightly outside of the growth window in the Ti-rich regime (*TTIP/Sr* =

55.4). The origin of this phase shift is unknown, though it is possibly associated with the

dynamics of boundaries between SrO-terminated and $TiO_2$-terminated surface regions

during the layer-by-layer growth of $SrTiO_3$. This is consistent with the phase shift only

occurring for oscillations in the 00 reflection, which contains information from surface

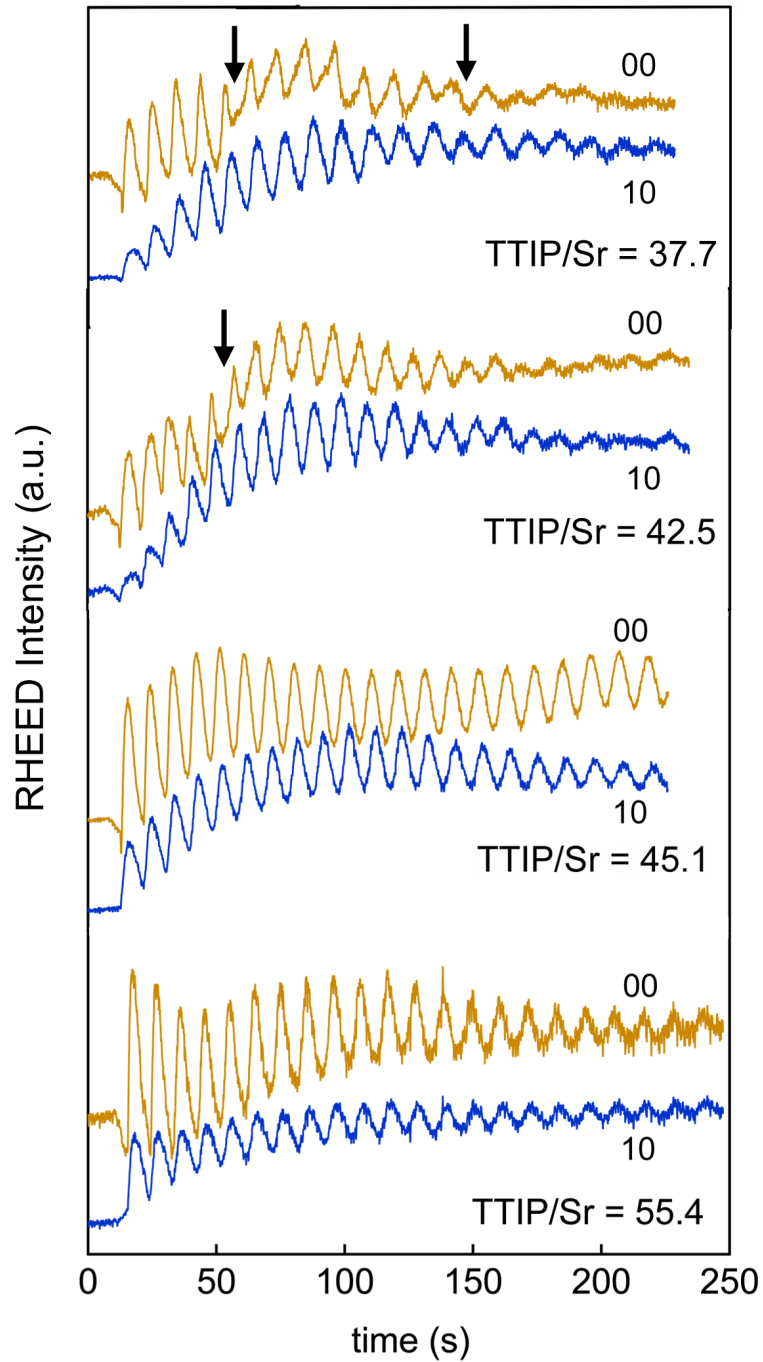features without lateral symmetry, such as steps and defects. Determining the exact origin of

**Figure 3.4:** RHEED intensity of the specular (00) and 10 diffracted beam taken along the [100] azimuth at the beginning of growth for samples grown at different *TTIP/Sr BEP* ratios (810 °C substrate temperature). Adapted with permission from [98]. Copyright 2014, AIP Publishing LLC

the phase shift lies beyond the scope of the study, but the correlation between changes in surface reconstruction and the RHEED intensity oscillations emphasize the significant variations in the surface stoichiometry within the XRD growth window. It should be noted that this analysis was limited to samples grown at 810 °C; samples grown at 850 °C either did not exhibit oscillations or exhibited oscillations that decayed within approximately 6 oscillation periods, which is likely due to the onset of a step-flow growth mode at higher temperatures.

*3.6 Implications for the Adsorption-controlled Growth of SrTiO$_3$ (001)*

The consistent trend described for surface reconstructions within the XRD-defined growth window indicates substantial variation in the surface stoichiometry (and the resulting bulk stoichiometry) of the growing thin films. Although the (1 × 1) growth regime results in a stoichiometric film insofar that the density of defects is sufficiently low to maintain film-substrate XRD peak overlap, a significant portion of the surface is SrO-terminated. Since SrO has a low vapor pressure at the growth temperatures considered here, a mixed termination surface is likely to lead to the accumulation of cation-excess defects over time. The mixed termination surfaces suggest growth is taking place outside of an adsorption-limited growth regime, where an overpressure of the more volatile constituent is supplied, ideally relying on desorption to regulate stoichiometry. The (1 × 1) regime for hybrid MBE is reminiscent of the RHEED patterns observed for SrTiO$_3$ films grown by solid-source MBE under stoichiometric conditions (to the extent possible outside a growth window). This a reasonable indicator of stoichiometry if no adsorption-controlled regime exists and flux

56

must be controlled to give a 1:1 A:B cation ratio, resulting in a comparable ratio of surface

terminations.

The adsorption-controlled growth regime thus begins with conditions giving a c(4 × 4)

reconstructed lattice, since a sufficient TTIP overpressure is supplied to maintain a $TiO_2$-

saturated surface. Any adsorbed SrO will remain in the film, and enough of the TTIP

precursor will impinge to fill any SrO-terminated sites. Any excess TTIP will desorb to

maintain 1:1 A:B stoichiometry. Since the c(4 × 4) reconstructed lattice persists beyond the

XRD window, optimal stoichiometry most likely lies at the overlap between the XRD

window and the c(4 × 4) growth regime. Indeed, electron mobilities exceeding 50,000

$cm^2V^{-1}s^{-1}$ were recorded for La-doped $SrTiO_3$ thin films grown in this regime (850 °C

substrate temperature, TTIP/Sr = 75) [93].


*3.7 Chapter Summary*

RHEED patterns from homoepitaxial $SrTiO_3$ (001) thin films were shown to vary

substantially within the XRD growth window. Changes in the surface reconstruction were

correlated with changes in the surface stoichiometry. In particular, the evolution of the

surface from (1 × 1) to multi-domain (2 × 1) to c(4 × 4) with an increasing relative TTIP

flux corresponds to the evolution from a mixed termination surface (with approximately

equal fractions of SrO and $TiO_2$ termination) to increasing $TiO_2$ coverage to a fully $TiO_2$-

saturated surface.  The crossover from mixed termination to $TiO_2$ saturation is marked by

the transition from multi-domain (2 × 1) to c(4 × 4) reconstructed lattices. RHEED intensity

oscillations observed at the beginning of growth exhibit a phase shift in the oscillations from

the specular reflection for *TTIP/Sr BEP* ratios below the crossover point. A truly adsorption-

controlled growth regime for stoichiometric $SrTiO_3$ thin films is defined by the overlap of growth conditions giving a $TiO_2$-saturated c(4 × 4) reconstructed lattice and growth conditions falling within the XRD growth window.  XRD therefore remains a powerful tool for the optimization of stoichiometry in $SrTiO_3$, and in this chapter, *in-situ* characterization by RHEED has been shown to provide vital information about the nature of growth within the XRD window, which was not possible with solid-source MBE.

# Chapter 4

$Ba_xSr_{1-x}TiO_3$ Thin Films with Low Dielectric Loss Grown by Hybrid Molecular Beam Epitaxy

*4.1 Introduction*

Chapter 3 discussed the evolution of the surface stoichiometry of $SrTiO_3$ within the XRD growth window as observed by *in-situ* RHEED characterization. This allows for refinement of the film stoichiometry beyond the XRD-based stoichiometry optimization of prototypic hybrid MBE-grown $SrTiO_3$ thin films introduced in Chapter 2. Though ultimately intended to aid in the MBE growth of high-mobility $SrTiO_3/SrTi_{1-x}Zr_xO_3$ heterostructures, it is worth evaluating the effectiveness of RHEED and XRD characterization in optimizing the stoichiometry of related material systems. To this end, this chapter will discuss the hybrid MBE growth and dielectric characterization of stoichiometric $Ba_xSr_{1-x}TiO_3$ (BST), an electric field-tunable dielectric of considerable interest for microwave device applications [15].

BST is a ferroelectric perovskite oxide solid solution with end members $BaTiO_3$, a ferroelectric at room temperature ($T_C$ = 393 K), and $SrTiO_3$, an incipient ferroelectric. Intermediate compositions yield ferroelectrics with a Curie temperature that varies approximately linearly with composition [107]. The ferroelectric transition for each composition is accompanied by a peak in the dielectric permittivity. The composition of BST tunable dielectrics for devices operating at room temperature is typically chosen to give a $T_C$ somewhat below room temperature, so that the BST dielectric is operating near the peak permittivity in the paraelectric state. In this regime, the permittivity is highly dependent on the applied electric field, while dielectric losses remain minimal [15]. The reasons for this will be discussed in following sections describing the relevant performance metrics for tunable dielectrics, which will further inform and motivate the stoichiometry optimization of BST with hybrid MBE.

*4.2 Figures of Merit for Tunable Dielectrics*

The interest in tunable dielectrics centers on the strong dependence of the permittivity on applied electric field in this class of materials. This property can be exploited for a number of microwave device applications that rely on variable capacitors, such as those involved in wireless communication. It is desirable to not only maximize electric-field tunability in these materials but to also minimize dielectric losses, which lead to deviations from ideal capacitor behavior. The following sections will describe these primary figures of merit, dielectric tunability and dielectric loss, as well as the factors that influence them.

*4.2.1 Tunability*

The dielectric tunability is the extent to which the relative permittivity of a dielectric material is suppressed in an applied electric field $E$. The tunability $n$ may be quantified as:

$$n = \frac{\varepsilon_r(0)}{\varepsilon_r(E)} \tag{1}$$

where $\varepsilon_r(0)$ is the relative permittivity at zero applied bias and $\varepsilon_r(E)$ is the relative permittivity at some arbitrary applied field. A tunable dielectric will exhibit $n > 1$, resulting in a nonlinear dependence of the electrical polarization on the electric field. The relative tunability $n_r$ is also sometimes used to quantify the suppression of the permittivity:

$$n_r = \frac{\varepsilon_r(0) - \varepsilon_r(E)}{\varepsilon_r(0)} = 1 - \frac{1}{n} \tag{2}$$

From Landau theory, one finds that the tunability is strongly dependent on the zero-field tunability, $\varepsilon_r(0)$. At low electric fields, the nonlinearity of the permittivity is weak, i.e. $n_r \ll 1$ and the polarization under DC bias $P_{DC} \approx \varepsilon_r(0)\varepsilon_0 E$, and the tunability can be expressed as:

61

$$n \approx 1 + 3\beta \left( \varepsilon_r(0)\varepsilon_0 \right)^3 E^2 \tag{3}$$

where $\beta$ is a coefficient left over from the Landau theory expansion of the Helmholtz free energy as a function of electrical polarization [15]. This illustrates the strong dependence of the tunability $n$ on the zero-field permittivity, as well as the applied electric field. This dependence remains strong even in the high-field limit, where $n \propto \varepsilon_r(0)$ [15].

The peak in $\varepsilon_r(0)$ in the vicinity of the ferroelectric transition is closely tied to the dependence of the tunability on $\varepsilon_r(0)$. The frequency of the transverse optical phonon mode, $\omega_{TO}$ in $SrTiO_3$ and BST, which governs the motion of the Ti cation within each $TiO_6$ octahedron and thus the polarizability of the material, approaches zero as the material is cooled near its Curie temperature. This "softening" of the phonon mode leads to an increase in $\varepsilon_r(0)$, which has been found to depend on the $\omega_{TO}$ according to:

$$\frac{\varepsilon_r(0)}{\varepsilon_\infty} = \frac{\omega_{LO}^2}{\omega_{TO}^2} \tag{4}$$

where $\varepsilon_\infty$ is the permittivity at optical frequencies and $\omega_{LO}$ is the frequency of the longitudinal optical phonon mode [108]. Tunability then arises from the dependence of $\omega_{TO}$ on the applied electric field. At temperatures far above the Curie temperature, $\omega_{TO}$ is only weakly dependent on applied electric field; however, near the ferroelectric transition, the application of an electric field leads to a substantial increase in $\omega_{TO}$, and the effect is more dramatic upon approaching the transition temperature (where $\omega_{TO}$ is lowest at zero-field) [109]. The permittivity is thus increasingly tunable as it reaches a maximum near the ferroelectric transition.

The above description of the physical mechanism for electric field-tunable permittivity is valid for ferroelectric perovskites in their paraelectric phase. It should be noted that the

permittivity is tunable in the ferroelectric phase as well. However, nearly all BST-based devices are operated in the paraelectric phase due to high dielectric losses suffered in the ferroelectric phase. Low dielectric loss is as vital as high tunability to the performance of devices utilizing tunable dielectrics, and as such, it will be discussed in the following section as part of the figure of merit.

*4.2.2 Dielectric Loss*

Dielectric loss can be generally described as the dissipation of electrical energy of an AC signal leading to a deviation from ideal capacitor behavior. The alternating current in an ideal capacitor (i.e. one that suffers no losses) leads the associated AC voltage by 90°. Dielectric loss will cause the voltage phase to shift by an angle $\delta$ toward the phase of the alternating current, and thus the non-ideal capacitor will exhibit resistive (dissipative) behavior to the extent determined by the deviation $\delta$. The dielectric loss is typically quantified with tan $\delta$, the loss tangent, or with the quality factor $Q = [\tan \delta]^{-1}$. $Q$ will be primarily used as a more convenient figure of merit for dielectric loss in most of the chapter.

Various mechanisms may contribute to the dielectric loss in a tunable dielectric-based capacitor. These may arise from intrinsic interactions between AC signal quanta and thermal phonons or from extrinsic contributions by (charged) defects and polar regions (e.g. precursors to the ferroelectric phase). Device-related losses, such as DC leakage and electrode losses at high AC frequencies, are also major contributors, but since this chapter is primarily concerned with losses from the tunable dielectric itself, device-related losses will not be investigated in great detail.

Extrinsic loss mechanisms constitute the most significant source of dielectric loss in the majority of tunable dielectric systems [110, 111]. These extrinsic contributions to loss typically scale directly with permittivity, which results in a nearly universal inverse relationship between the quality factor and tunability. For example, polar regions in the ferroelectric phase can be shown to contribute to loss according to:

$$\tan \delta_{PR} \propto \varepsilon^{4.5-d} \; , \tag{5}$$

where $d$ is the dimension of the polar defect (e.g. $d = 0$ for point defects, $d = 1$ for line defects, etc) [15]. The strong dependence of this loss mechanism, as well as the tunability, on permittivity motivates the design of devices with tunable dielectrics operating exclusively in the paraelectric phase, where the density of polar regions is minimal. Losses from charged point defects are also dependent on the permittivity, as well as the density of defects $n_d$ according to:

$$\tan \delta_{CD} \propto \varepsilon n_d Z^2 \; , \tag{6}$$

where $Z$ is the effective charge of the defect [15]. Effectively mitigating this loss mechanism by reducing $n_d$ motivates the growth of tunable dielectrics by MBE to be discussed in this chapter.

Intrinsic loss mechanisms also warrant some discussion in order to understand the limits of the quality factor in the absence of extrinsic loss contributions. The 3-quantum and 4-quantum mechanisms involve the absorption of AC signal quanta by thermal phonons. Both contribute to the loss proportional to the permittivity [15], so even with reduced extrinsic contributions, an inverse relationship between the tunability and quality factor are expected to remain. In contrast, the quasi-Debye [112, 113] intrinsic loss mechanism contributes to loss inversely with the permittivity. This mechanism is active in non-centrosymmetric

crystals and can also be induced when the application of DC bias breaks the inversion symmetry of a centrosymmetric crystal. The acoustic phonon distribution is then shifted from its equilibrium state by an AC signal. The Debye-like relaxation of the phonon distribution leads to the dissipation of the AC signal, resulting in loss. It can be shown that:

$$\tan \delta_{QD} \propto n_r \tag{7}$$

Comparing with Eq. (2), this indicates that as the permittivity is suppressed in an applied field, the associated loss will increase, unlike most other loss mechanisms. As such, observation of this behavior has been attributed to a cross-over from extrinsically dominated loss to intrinsically dominated loss [114].

*4.2.3 Thin Films and Bulk Specimens*

The growth of thin-film tunable dielectrics is motivated by the prospect of improved integration with semiconductors and by lower operating voltages. However, the tunability and quality factor of thin-film tunable dielectrics are almost universally lower than in polycrystalline or single-crystal bulk specimens [110, 111, 115, 116]. This has been attributed to a number of factors, mainly focusing on higher defect densities resulting from poor stoichiometry control and high-energy thin film deposition processes, such as sputtering, which is commonly used for the growth of BST thin films. Electrode/dielectric interfaces also negatively impact the tunability by forming a "dead layer," an interfacial region that comprises a more significant fraction of the dielectric in thin films than in bulk specimens.

The dielectric dead layer constitutes a low-permittivity region in a dielectric that originates at the interface with the electrodes. Interfacial defects, such as trapped charge at

the electrode-dielectric junction [117], may lead to polarization of the dielectric in the dead layer, reducing the permittivity of the layer relative to the interior of the film by locally hardening the transverse optical phonon (soft) mode that is responsible for the high permittivity and tunability of ferroelectric perovskite oxides [118]. This effectively places a low capacitance in series with the higher-permittivity tunable dielectric, lowering the effective overall permittivity of the device, which negatively impacts the tunability of the film and may also contribute to loss.

Growth of thin film tunable dielectrics by MBE, which enables growth with low defect densities and high interface quality, is therefore expected to result in improved dielectric performance. Hybrid MBE in particular is credited with enhanced electron mobility in $SrTiO_3$ thin films, with values exceeding those of bulk specimens [92]. The remainder of this chapter will focus on the growth of BST thin films by the hybrid MBE approach to achieve self-regulating A:B stoichiometry in this tunable dielectric material system. The figures of merit described above will be used to evaluate the effectiveness of the stoichiometry optimization methods detailed in Chapters 2 and 3.

*4.3 Experimental Details*

BST thin films were grown using the same hybrid MBE configuration described in Chapter 3. Ba (99.99%, Sigma-Aldrich) was supplied via a low-temperature solid-source effusion cell. All films were grown at a substrate temperature of 750 °C as read by thermocouple (730 °C by optical pyrometer). The *Ba/Sr* ratio was varied by adjusting the Sr BEP and Ba cell temperature; the Ba BEP could not be accurately determined due to incompatibility with the beam flux ionization gauge. Reported compositions were

determined from Rutherford Backscattering Spectrometry measurements of 300 nm thick BST films on epitaxial Pt/SrTiO$_3$ (001) (see below). With the Ba and Sr fluxes thus fixed, the *TTIP/(Ba+Sr)* ratio was varied by adjusting the TTIP BEP. Additional oxygen was supplied for all growths by an RF plasma source operating at 250 W and a background pressure of $4 \times 10^{-6}$ Torr measured at the beam flux ionization gauge. The growth conditions were first optimized with growth on SrTiO$_3$ (001) single-crystal substrates. RHEED patterns (14 kV accelerating voltage) along the [100] and [110] azimuths for each film were captured with a Staib RHEED system after post-growth cooldown, and the out-of-plane lattice parameter of these films was measured by XRD *2θ-ω* scans (Philips X'PERT Panalytical MRD Pro Thin Film Diffractometer) in the vicinity of the SrTiO$_3$ 002 reflection. Atomic force microscopy (AFM) images were captured using an Asylum MFP3D scanning probe microscope operating in tapping mode.

For the dielectric characterization of BST films in this study, parallel-plate capacitor structures with Pt top and bottom electrodes were fabricated. Pt bottom electrodes were grown epitaxially (with a cube-on-cube orientation) on SrTiO$_3$ (001) single crystal substrates to a thickness of 100 nm by DC magnetron sputtering at a substrate temperature of 825 °C and an Ar sputter gas pressure of 10 mTorr. These Pt films were then annealed in 1 atm oxygen at 1000 °C for 10 min. BST films (300 nm thick) were then grown on the bottom electrodes by hybrid MBE using conditions optimized on bare SrTiO$_3$ substrates. Prior to growth, samples were heated from 200 °C to 750 °C (growth temperature) in oxygen plasma running under the same conditions as during growth. Post-growth, samples were cooled below 400 °C under an oxygen plasma.

Parallel-plate capacitor mesas and Pt top electrodes were then patterned using a two-step mask photolithographic process. The capacitor mesa was first defined by wet etching in 1:20 diluted trace-metal grade HF. Pt top electrodes (100 nm thick, $45 \times 45~\mu m^2$) deposited by electron-beam evaporation were then patterned by a lift-off process. These devices were then annealed in 1 atm of oxygen at 800 °C for 20 min. The dielectric properties of the devices were extracted from capacitance-voltage (C-V) measurements (courtesy of Evgeny Mikheev) performed with a Cascade Microtech probe station, along with GGB 100-μm GSG probes and an HP 4294 A impedance analyzer. A 500 mV oscillation voltage (~0.02 MV/cm for the given film thicknesses) was used for measurements versus frequency and versus DC bias.

*4.4 Stoichiometry Optimization of BST Grown on SrTiO₃ (001)*

The optimization of growth conditions for 1:1 A:B stoichiometry in hybrid MBE-grown BST thin films followed a strategy similar to that introduced in Chapter 2 and elaborated upon in Chapter 3 for SrTiO$_3$. That is, the *TTIP/(Ba + Sr)* ratio was varied by adjusting the TTIP BEP to give a minimum out-of-plane lattice parameter (measured by *ex-situ* XRD) in the BST films. This was then juxtaposed with RHEED patterns taken after growth to determine the conditions with optimal stoichiometry. Central to this analysis is the assumption that any observed lattice expansion as a function of TTIP BEP is due only to A:B off-stoichiometry, and not due to changes in the alloy composition (beyond those arising from typical fluctuations in the flux of any given source). Given the low vapor pressure of BaO and SrO at the growth temperatures considered and given the stability of alkaline earth solid sources for a fixed oxygen background [86], it is reasonable to assume

that the relative incorporation of Ba and Sr into the film does not change appreciably as the

TTIP BEP is varied. Assuming that similar defect mechanisms are active for

accommodating A:B off-stoichiometry in BST as in pure $SrTiO_3$, lattice expansion can thus

be attributed to these defect mechanisms in off-stoichiometric growth conditions, rather than

changes in alloy composition.

Figure 4.1 shows the out-of-plane lattice parameters for $Ba_{0.1}Sr_{0.9}TiO_3$ thin films grown

on $SrTiO_3$ (001) single crystal substrates at various TTIP BEP. The TTIP BEP is shown

rather than the *TTIP/(Ba + Sr)* BEP ratio due to ambiguity in the Ba BEP, which could not

be measured with the beam flux ionization gauge. However, fixing the Sr BEP and Ba cell

temperature gives consistent, reproducible results. Varying the TTIP BEP with the Ba and Sr

fluxes thus fixed gives a minimum in the out-of-plane lattice parameter. This minimum

value is consistent with that expected for BST of the same composition coherently strained

to $SrTiO_3$ (001).

The range of growth conditions spanning the apparent minimum in the lattice parameter

is comparatively narrow, as expected for the growth temperature (750 °C), which is near the

onset of the desorption-limited regime of TTIP. The XRD growth window may also appear

narrow compared to $SrTiO_3$ due to the fact that even at the minimum, the XRD 002 peak for

BST does not overlap with that of the $SrTiO_3$ (001) substrate. As such, film peak shifts near

the minimum are not masked by overlap with the substrate peak.

Tracking the RHEED patterns in Fig. 4.1 yields a similar result as that found in Chapter

3 for homoepitaxial $SrTiO_3$ (001). Near the minimum in the Ti-poor regime, one observes a

pattern indicative of a $(2 \times 1)$ mixed-termination surface due to incomplete $TiO_2$ saturation.

At the minimum, a pattern indicative of a $c(4 \times 4)$ reconstructed lattice is
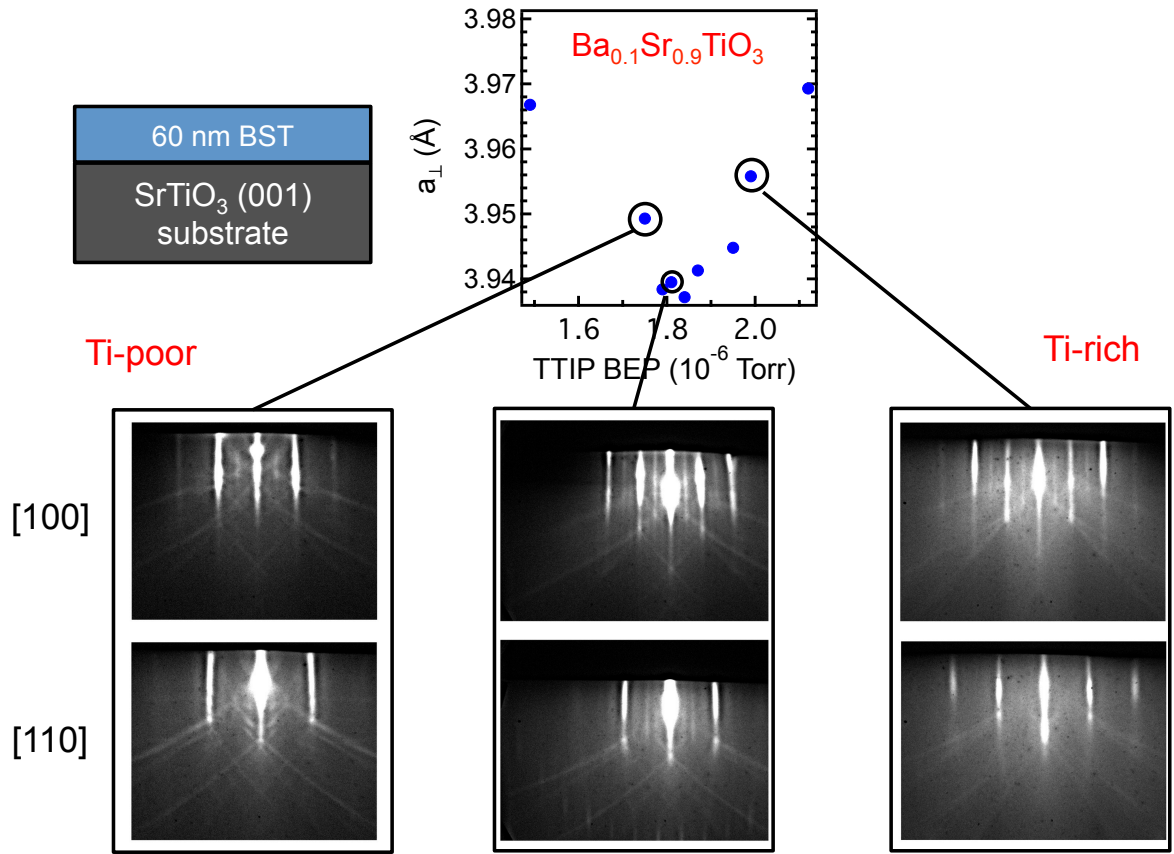
**Figure 4.1:** Out-of-plane lattice parameters of 60 nm $Ba_{0.1}Sr_{0.9}TiO_3$ thin films grown on $SrTiO_3$ (001) at various *TTIP BEP*. RHEED patterns taken along the [100] and [110] azimuths after growth are shown for samples at select growth conditions.

observed, consistent with optimal stoichiometry in an adsorption-controlled growth regime where enough TTIP is supplied to achieve a pure $TiO_2$ surface termination. Supplying additional TTIP brings the growth into a Ti-rich regime, resulting in a RHEED pattern indicative of a Ti-rich ($2 \times 1$) surface. Therefore, it seems that for a relatively low Ba content, the trend in out-of-plane lattice parameter and the associated trend in the RHEED pattern is similar to that observed in $SrTiO_3$.

Figure 4.2 shows the out-of-plane lattice parameters for $Ba_{0.46}Sr_{0.54}TiO_3$ thin films grown on $SrTiO_3$ (001) at various TTIP BEP values. Similar to the lattice parameters of $Ba_{0.1}Sr_{0.9}TiO_3$ thin films, the lattice parameters of $Ba_{0.46}Sr_{0.54}TiO_3$ thin films exhibit a minimum value as a function of TTIP BEP. The minimum lattice parameter is also similarly consistent with the expected value for a film of that composition coherently strained to $SrTiO_3$ (001). The position of the lattice parameter minimum ($\sim 1.45 \times 10^{-6}$ Torr) for this composition is lower than that for $Ba_{0.1}Sr_{0.9}TiO_3$ most likely due to a lower overall A-cation flux rather than due to a substantial difference in the dynamics of adsorption-controlled growth at this composition.

The trend in the observed RHEED pattern differs somewhat from the trend observed at lower Ba content and in pure $SrTiO_3$. A ($1 \times 1$) surface lattice is observed for growth conditions away from the minimum lattice parameter value. A c($4 \times 4$) reconstructed lattice is not observed for any of the growth conditions explored at this composition. Instead, a multi-domain ($2 \times 1$) surface is observed throughout the range of growth conditions in the vicinity of the lattice parameter minimum. It is possible that at intermediate compositions, the c($4 \times 4$) surface reconstruction is no longer energetically favored, and as such it cannot be used to determine the conditions giving a purely $TiO_2$-terminated surface. Although
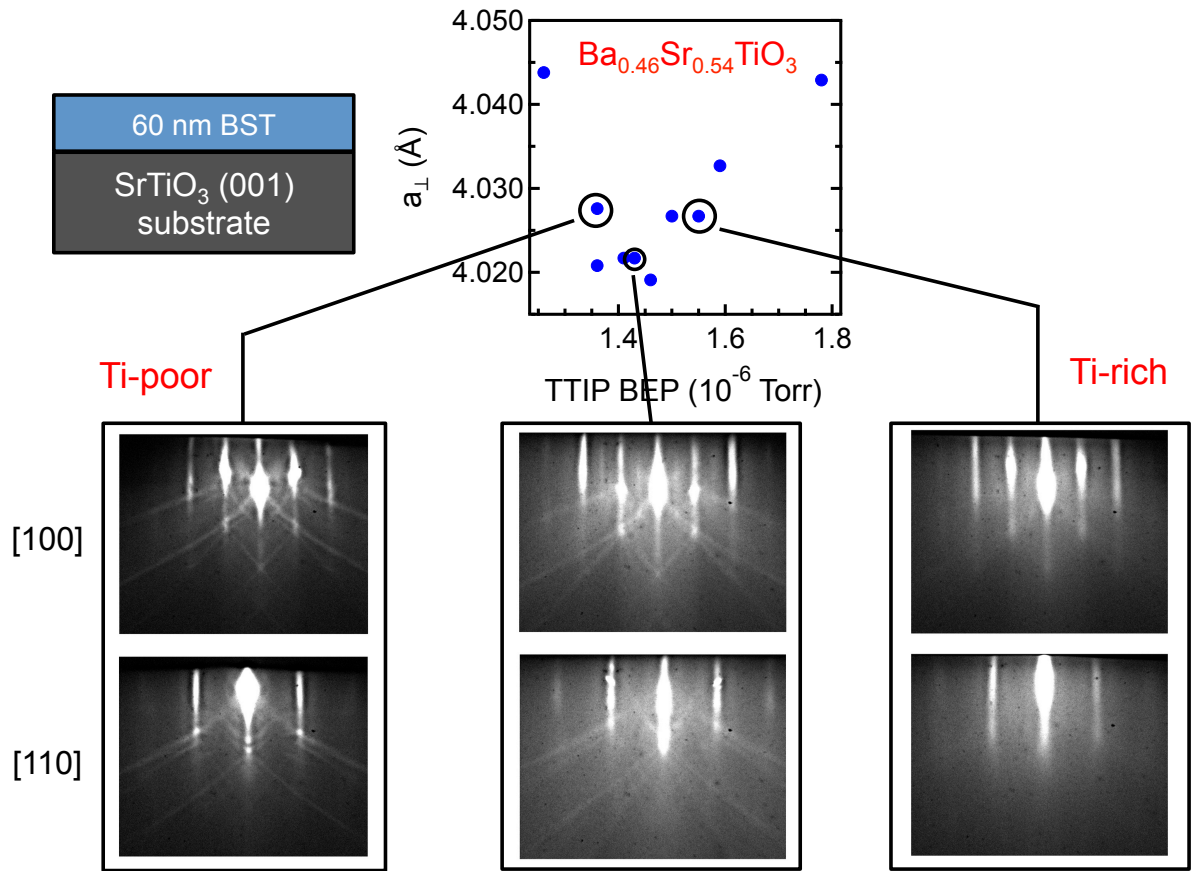
**Figure 4.2:** Out-of-plane lattice parameters of 60 nm $Ba_{0.5}Sr_{0.5}TiO_3$ thin films grown on $SrTiO_3$ (001) at various *TTIP BEP*. RHEED patterns taken along the [100] and [110] azimuths after growth are shown for samples at select growth conditions.

$Ba_{0.46}Sr_{0.54}TiO_3$ retains the same bulk lattice as $SrTiO_3$ (space group $Pm\bar{3}m$), the increased

Ba substitution disrupts the formation of a $c(4 \times 4)$ surface lattice by changing the energetics

at the surface.

RHEED intensity oscillations were observed for all growth conditions featured in Figs. 1

and 2, indicating a layer-by-layer growth mode for all BST films explored in this study.

Similar to the case for $SrTiO_3$ films investigated in Chapter 3, a phase shift can be observed

for oscillations of the intensity of the specular (00) reflection of $Ba_{0.1}Sr_{0.9}TiO_3$ after ~4

oscillation periods (see Fig. 4.3a), placing the intensity oscillations from the 00 reflection

approximately $\pi$ rad out of phase with oscillations from the 10 diffracted beam. This phase

shift is observed for TTIP BEP's of $1.49 \times 10^{-6}$ Torr and $1.75 \times 10^{-6}$ Torr, placing the

growth within the Ti-poor regime (compare to Fig. 4.1). The 00 and 10 reflection intensity

oscillations remain $\sim\pi/2$ rad out of phase and do not exhibit a phase shift for growth

conditions giving a minimum lattice parameter or conditions falling within the Ti-rich

growth regime, consistent with observations presented in Chapter 3 for the growth of

$SrTiO_3$. In contrast, the RHEED intensity of 00 and 10 reflections from $Ba_{0.46}Sr_{0.54}TiO_3$

films do not exhibit this phase shift under Ti poor conditions within approximately 6

monolayers from the beginning of growth (see Fig. 4.3b as a representative example). A

phase shift may occur after additional oscillation periods, though it is also possible the phase

shift may not be observed at higher Ba substitutions, where the introduction of disorder

through heavy alloying may disrupt whatever mechanism is involved with the observed

phase shift. This is reasonable given the significant effect of high Ba substitution on

observed surface reconstructions. Additional studies at higher substrate temperatures, where
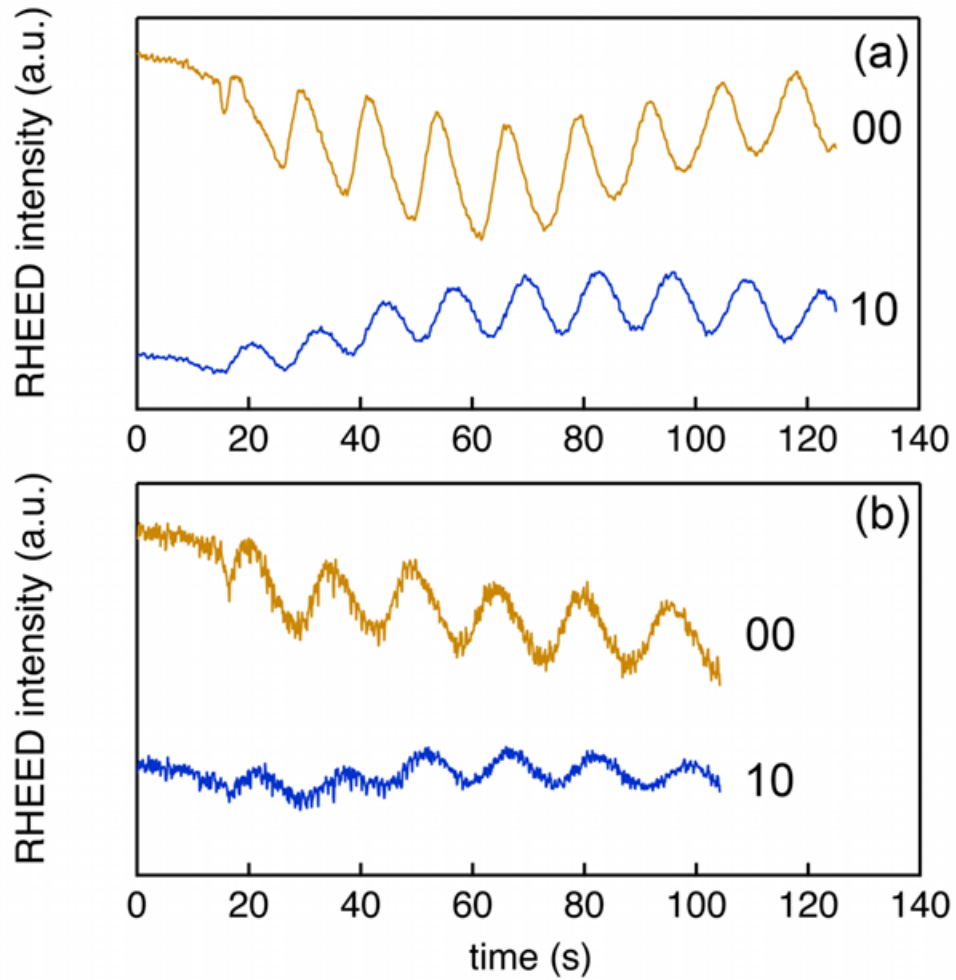
**Figure 4.3:** RHEED intensity oscillations of the specular (00) and 10 diffracted beams taken along the [100] azimuth at the beginning of growth for (a) $Ba_{0.1}Sr_{0.9}TiO_3$ grown with a *TTIP BEP* of $1.49 \times 10^{-6}$ Torr and (b) $Ba_{0.46}Sr_{0.54}TiO_3$ grown with a *TTIP BEP* of $1.26 \times 10^{-6}$ Torr.

the growth window is expected to widen, is warranted to investigate this trend further for various BST compositions.

It has been shown that the XRD stoichiometry optimization approach appears to be valid even for heteroepitaxial BST grown on $SrTiO_3$, up to relatively high Ba substitution (46% Ba). RHEED also remains a reliable tool for tracking the surface and bulk stoichiometry of BST thin films, though it is less informative with increasing Ba content. To quantify the effectiveness of these stoichiometry optimization methods, the dielectric properties of these films need to be measured. Dielectric characterization of BST films on bare $SrTiO_3$ would necessitate a coplanar, inter-digitated capacitor device geometry, which requires complicated analysis to extract dielectric data, confounded further by the large permittivity of $SrTiO_3$ single crystal substrates. Therefore, the following section will discuss the growth of BST on an epitaxial Pt /$SrTiO_3$ (001) as a means to construct parallel plate capacitor structures for dielectric characterization.

*4.5 BST Growth on Pt/SrTiO₃*

Figure 4.4a shows a 5 × 5 μm$^2$ *ex-situ* AFM height scan micrograph obtained from a 100 nm epitaxial Pt (001) film on $SrTiO_3$ (001) after annealing in 1 atm oxygen for 10 min at 1000 °C. A cross-hatched pattern on a fairly smooth (380 pm RMS) surface is consistent with previous studies [119]. The *in-situ* RHEED pattern shown in Fig. 4.4b was captured along the [110] azimuth of the same film at a substrate temperature of 750 °C in oxygen plasma. The streaks indicate an atomically smooth surface, consistent with the AFM micrograph, while the bright spots indicate the presence of some 3-dimensional features on

the surface. The $1/5^{th}$-order reflections observed along the [110] azimuth are consistent with previous RHEED studies of Pt (001) surfaces [120].

BST films were grown on epitaxial Pt bottom electrodes using growth conditions optimized for minimum lattice parameter and/or c(4 × 4) surface reconstruction. No RHEED oscillations were observed for BST films grown on Pt/SrTiO$_3$, most likely due to the textured nature of the growing films (see below). Figure 4.5a shows a representative RHEED pattern captured along the [100] azimuth of a 300 nm BST film on Pt/SrTiO$_3$ after the post-growth cooldown. The diffraction patterns along [100] and [110] azimuths are qualitatively indistinguishable. The patterns consist of both streaks and spots, indicating interaction of the RHEED beam with both atomically smooth surfaces as well as 3-dimensional features. The spacing of the streaks also suggests a textured film in which (001)-oriented grains are rotated 45° relative to one another, effectively giving a RHEED pattern along [100] and [110] azimuths of different grains simultaneously. Because of this convolution of images from multiple grains, the surface reconstructions observed in BST on SrTiO$_3$ are not seen here, though they may form locally on each (001)-oriented grain.

Figure 4.5b shows a 5 × 5 µm$^2$ *ex-situ* AFM micrograph obtained from the same 300 nm BST film discussed above. Rod-like and triangular features (20-50 nm in height) are visible among a comparatively smooth surface (1.50 nm RMS). This is consistent with the RHEED pattern indicating both a smooth surface and 3-dimensional features. RHEED and AFM indicate a textured microstructure in BST films grown on epitaxial Pt, which is confirmed by wide-angle XRD 2$\theta$-$\omega$ scans. Bragg peaks corresponding to (110)- and (111)-oriented grains of either Pt, BST, or both can be seen in the inset of Fig. 4.6. The relative intensities of the 110 and 111 peaks vary for each sample without any apparent trend based
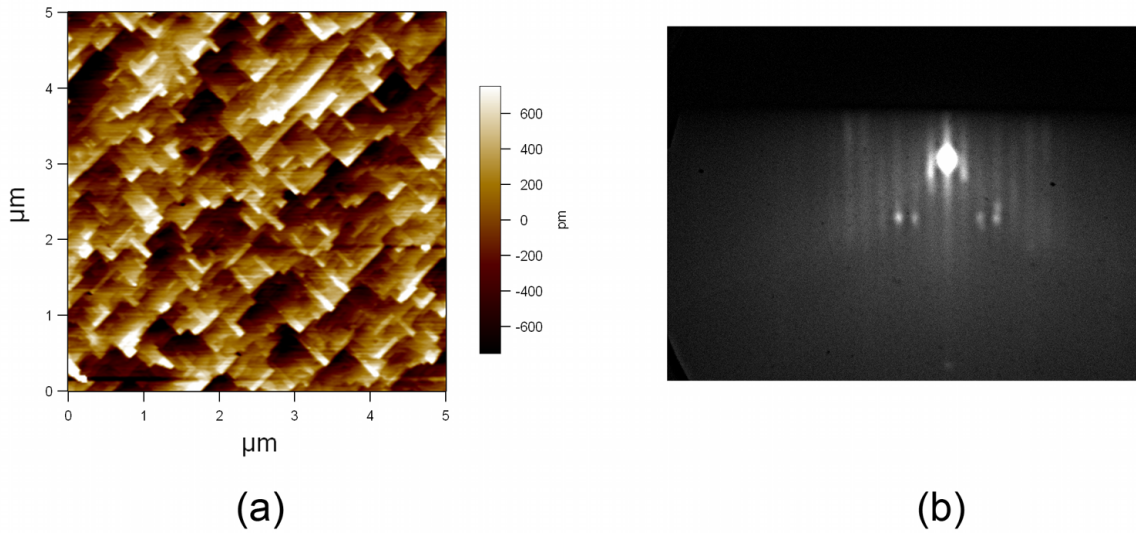
(a)

(b)

**Figure 4.4:** (a) Typical AFM height image ($5 \times 5$ μm$^2$) of 100 nm epitaxial Pt film on SrTiO$_3$ (001) after annealing in oxygen and (b) RHEED pattern captured along the [110] azimuth of an epitaxial Pt/SrTiO$_3$ (001) film heated to 750 °C in oxygen plasma.
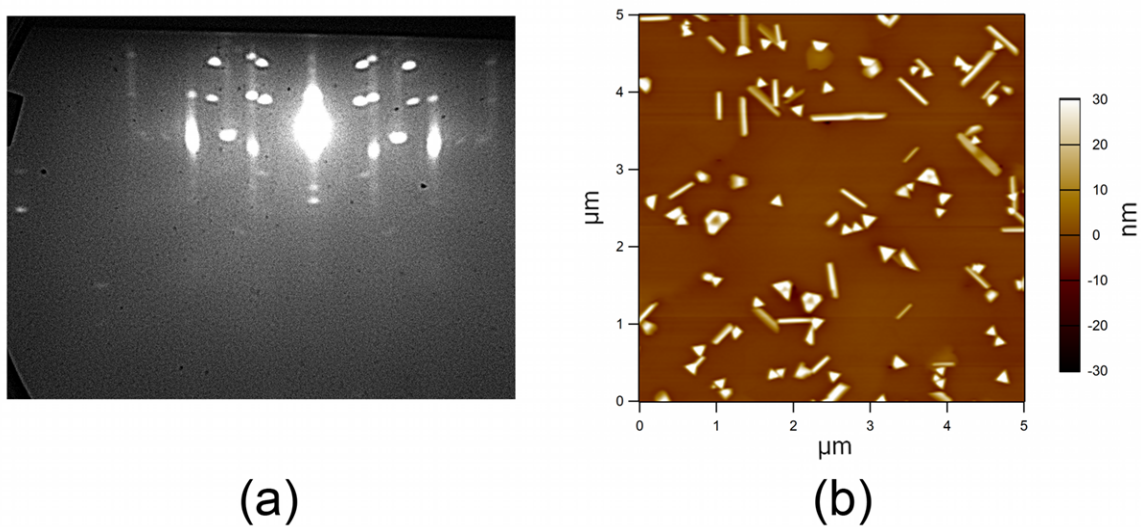


(a)

(b)

**Figure 4.5:** (a) RHEED pattern taken along the [100] azimuth of a ~300 nm Ba$_{0.35}$Sr$_{0.65}$TiO$_3$ thin film after growth on an epitaxial Pt/SrTiO$_3$ (001) bottom electrode and (b) a typical $5 \times 5$ μm$^2$ *ex*-situ AFM height image (60 nm scale) captured from the same film.

on BST film stoichiometry or composition, and as such they are probably dependent on variations in the Pt bottom electrodes. The rod-like structures observed in AFM are associated with the (110)-oriented grains, while the triangular features are associated with (111)-oriented grains. These shapes are the result of faceting of these grains to achieve a (001) free surface, which is the lowest-energy surface for BST.

High-resolution XRD *2θ-ω* scans in the vicinity of the 002 peak of $SrTiO_3$ (see Fig. 4.6) show 002 Bragg peaks from the $SrTiO_3$ (001) substrate, the epitaxial Pt (001) film, and the (001)-oriented grains of BST. The Laue oscillation period corresponds to a film thickness of approximately 100 nm; they can therefore be attributed to the epitaxial Pt bottom electrode. The Laue oscillations are also observed in $Pt/SrTiO_3$ (001) fillms before growth and indicate both high structural quality and interface quality in the Pt film after growth as well. The shift in the BST 002 peak with composition is consistent with lattice expansion with increasing Ba substitution. Off-axis measurements of the 103 and 101 Bragg peak positions for (001)-oriented BST grains give in-plane lattice parameters that are within 0.05% of the out-of-plane lattice parameters for respective compositions, indicating that the (001)-oriented grains are relaxed.

Structural characterization of polycrystalline, relaxed BST films on epitaxial $Pt/SrTiO_3$ (001) reveals substantial differences with single-crystal, coherently strained films grown directly on $SrTiO_3$ (001). This may complicate comparison of the growth optimization in the previous section with the resulting dielectric properties of films grown for parallel plate capacitor structures described in this section. It is worth noting that dielectric properties may vary substantially along different crystallographic directions, as it is relevant for polycrystalline BST films. We note, however, that (001)-oriented BST
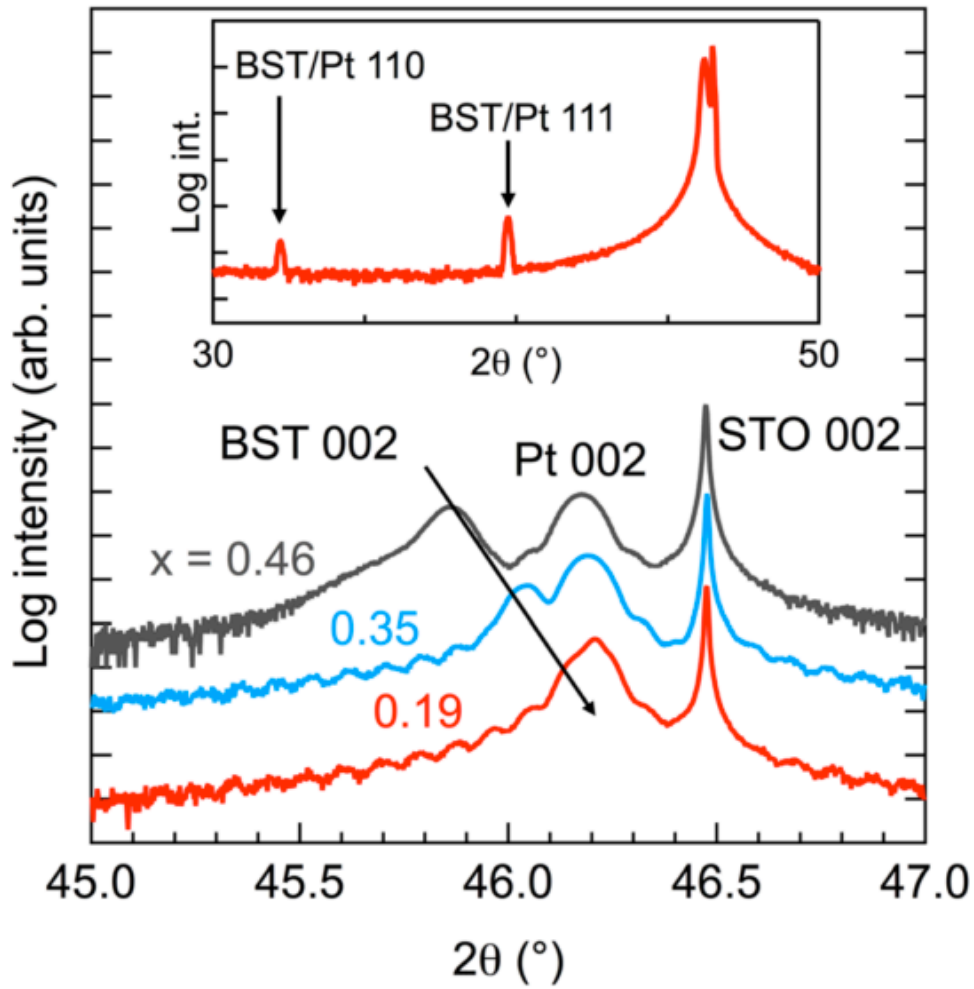
78

**Figure 4.6:** XRD *2θ-ω* spectra in the vicinity of the 002 reflection of SrTiO₃ for
Ba$_x$Sr$_{1-x}$TiO₃/Pt/SrTiO₃ structures with *x* = 0.19, 0.35, and 0.46. The inset shows a wide-
angle *2θ-ω* scan for the sample with *x* = 0.19. Reprinted with permission from [121].
Copyright 2012, AIP Publishing LLC

comprises the majority phase for these films, with comparable fractions of grains with other orientations among films with different growth conditions and compositions. A comparison of the dielectric properties of these samples therefore remains valid. The following section will present the dielectric properties of parallel plate capacitors based on these BST thin films to enable this comparison and thus evaluate the effectiveness of the stoichiometry optimization approach described previously.

*4.6 Dielectric Characterization*

The author would first like to acknowledge Evgeny Mikheev for diligently and conscientiously collecting the dielectric data to be presented in this section, allowing the author the privilege of adapting it for the evaluation of the growth technique. In section 4.4, it was assumed that a minimum lattice parameter in XRD and/or a c(4 × 4) surface reconstruction in films grown on $SrTiO_3$ indicated growth conditions that give optimal film stoichiometry. To test this hypothesis, $Ba_{0.1}Sr_{0.9}TiO_3$ films were grown on Pt bottom electrodes with different TTIP BEP's, corresponding to conditions falling within the Ti-poor ($1.70 \times 10^{-6}$ Torr), stoichiometric ($1.77 \times 10^{-6}$ Torr), and Ti-rich regimes ($1.89 \times 10^{-6}$ Torr), based on data presented in Fig. 4.1. The frequency-averaged ($10^5$-$10^6$ Hz, the frequency regime in which only the BST loss is measured, see below) quality factor ($Q_{av}$) and relative permittivity ($\varepsilon_r$) of each sample are presented in Table 4.1.  Clearly, the growth condition corresponding to films with a minimum lattice parameter and c(4 × 4) surface reconstruction suffers the lowest losses (highest $Q_{av}$). Deviation from the stoichiometric condition in either regime of off-stoichiometry leads to a substantial drop in the quality factor, most likely due to the incorporation of defects from non-stoichiometry. All three films in Table 4.1 have

**Table 4.1:** Frequency-averaged quality factor $Q_{av}$ and relative permittivity $\varepsilon_r$ of parallel plate capacitors with $Ba_{0.1}Sr_{0.9}TiO_3$ films grown at various values of *TTIP BEP*, selected for comparison with growth conditions presented in Fig. 4.1.

| *TTIP BEP* ($\times 10^{-6}$ Torr) | $Q_{av}$ | $\varepsilon_r$ |
|---|---|---|
| 1.70 | 790 | 420 |
| 1.77 | 2290 | 410 |
| 1.89 | 1090 | 430 |

similar values of $\varepsilon_r$, as is expected for BST films of the same composition. Therefore, varying the TTIP BEP appears to affect the A:B stoichiometry substantially without a significant effect on the extent of Ba substitution. This strongly supports the hypothesis that the lattice parameter and surface reconstruction can be used to evaluate and optimize the bulk stoichiometry of BST thin films.

Figure 4.7 shows $Q$ and $\varepsilon_r$ for BST films with 19%, 35%, and 46% Ba substitution as a function of frequency. The films have frequency-averaged ($10^5$-$10^6$ Hz) quality factors, $Q_{av}$, of 4350, 1130, and 140, respectively. As expected, $\varepsilon_r$ increases while $Q$ decreases with increasing Ba content, due to the increasing contribution of multiple loss mechanisms at higher values of $\varepsilon_r$ described in previous sections. A lower $Q$ for the films with $x = 0.19$ and 0.35 at frequencies below $\sim 10^4$ Hz can be attributed to losses from DC leakage [122]. Values of $Q$ measured at frequencies above $10^4$ Hz are primarily determined by the loss from the BST film [122]. The film with $x = 0.19$ exhibits sharp peaks in Q versus frequency, which are reproducible and observed on other instruments. Other hybrid MBE-grown BST films with $Q > 1000$ have exhibited these peaks as well, though their origin remains unclear. The substantially lower $Q$ observed for the film with $x = 0.46$ can be attributed to the
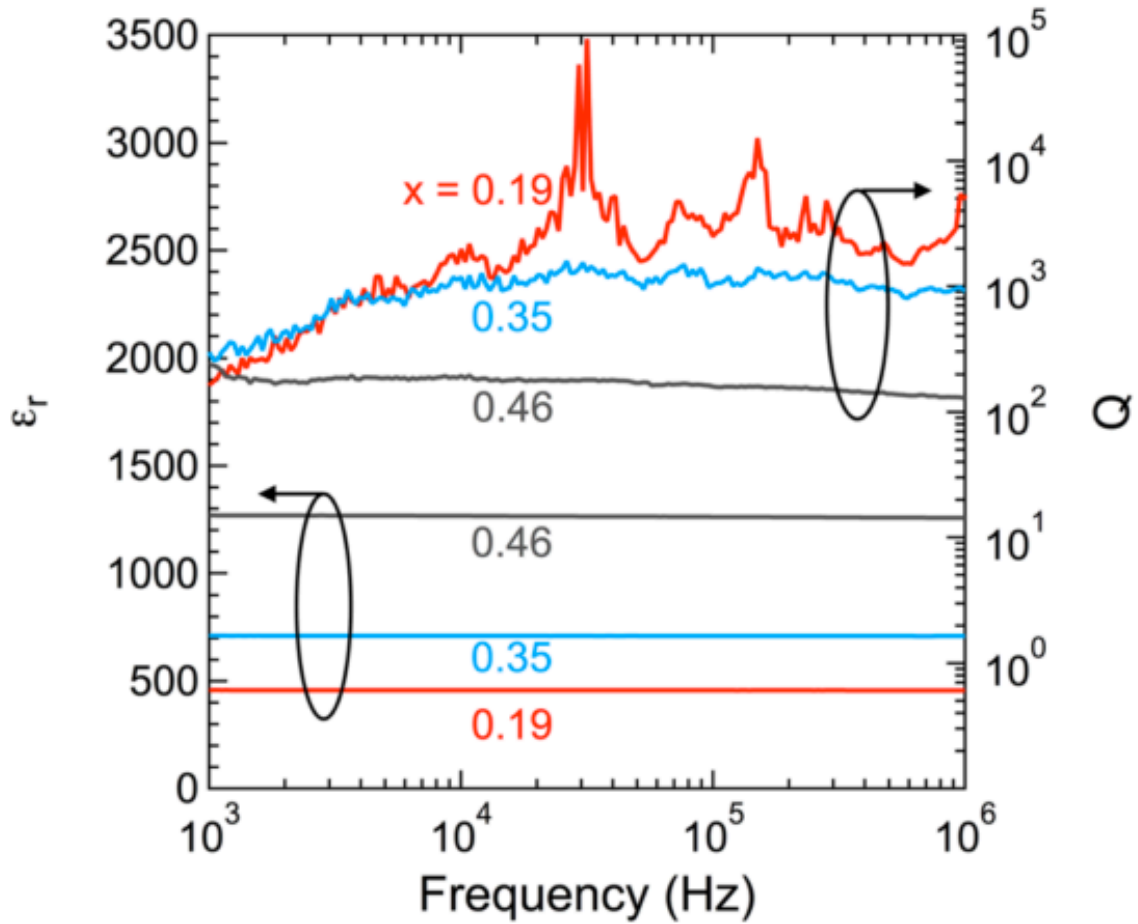
**Figure 4.7:** Relative permittivity $\varepsilon_r$ and quality factor $Q$ as a function of frequency for parallel plate capacitors with $Ba_xSr_{1-x}TiO_3$ films with compositions $x = 0.19$, 0.35, and 0.46. The values of permittivity were extracted from measured capacitances and film thicknesses measured with a Dektak Profilometer. Reprinted with permission from [121]. Copyright 2012, AIP Publishing LLC

formation of ferroelectric domains in BST films with higher Ba content. A slight hysteresis in capacitance-voltage measurements of this sample also suggests that this is the case. Although the ferroelectric transition occurs below room temperature for BST bulk specimens at this composition, the ferroelectric transition in thin films tends to be shifted to higher temperatures as compared to bulk specimens.

The relative permittivity and tunability of these films is shown as a function of applied electric field $E$ in Fig. 4.8a. The tunability clearly increases with increasing zero-field permittivity, and the permittivity approaches similar values for all films at high fields, consistent with the discussion in section 4.2. Figure 4.8b presents $Q$ plotted against $E$ for each film. For the films with $x = 0.19$ and 0.35, the $Q$ is highest at zero field and decreases with increasing field at low $E$. This is consistent with loss being dominated by quasi-Debye loss, which contributes more loss as $\varepsilon_r$ is suppressed. In contrast, the $Q$ for the film with $x = 0.46$ initially increases with increasing field, which suggests that an extrinsic mechanism, most likely from ferroelectric polar regions, is contributing loss proportional to the permittivity. Therefore, as the permittivity is suppressed, the loss contribution from polar regions is reduced initially. All films exhibit a further decrease in $Q$ at high fields, which can be attributed to the onset of soft dielectric breakdown.

The behavior for $Q$ versus applied field at $x = 0.46$ for hybrid MBE-grown BST is typical of higher loss films of any composition in the literature. When extrinsic factors dominate the dielectric loss, an initial increase in $Q$ is expected to result from suppression of loss mechanisms with decreased permittivity. Hybrid MBE-grown films at $x = 0.19$ and 0.35 are exceptional in that the decrease in $Q$ with applied field indicates that loss is dominated by the intrinsic quasi-Debye mechanism. Therefore, the stoichiometry optimization allowed
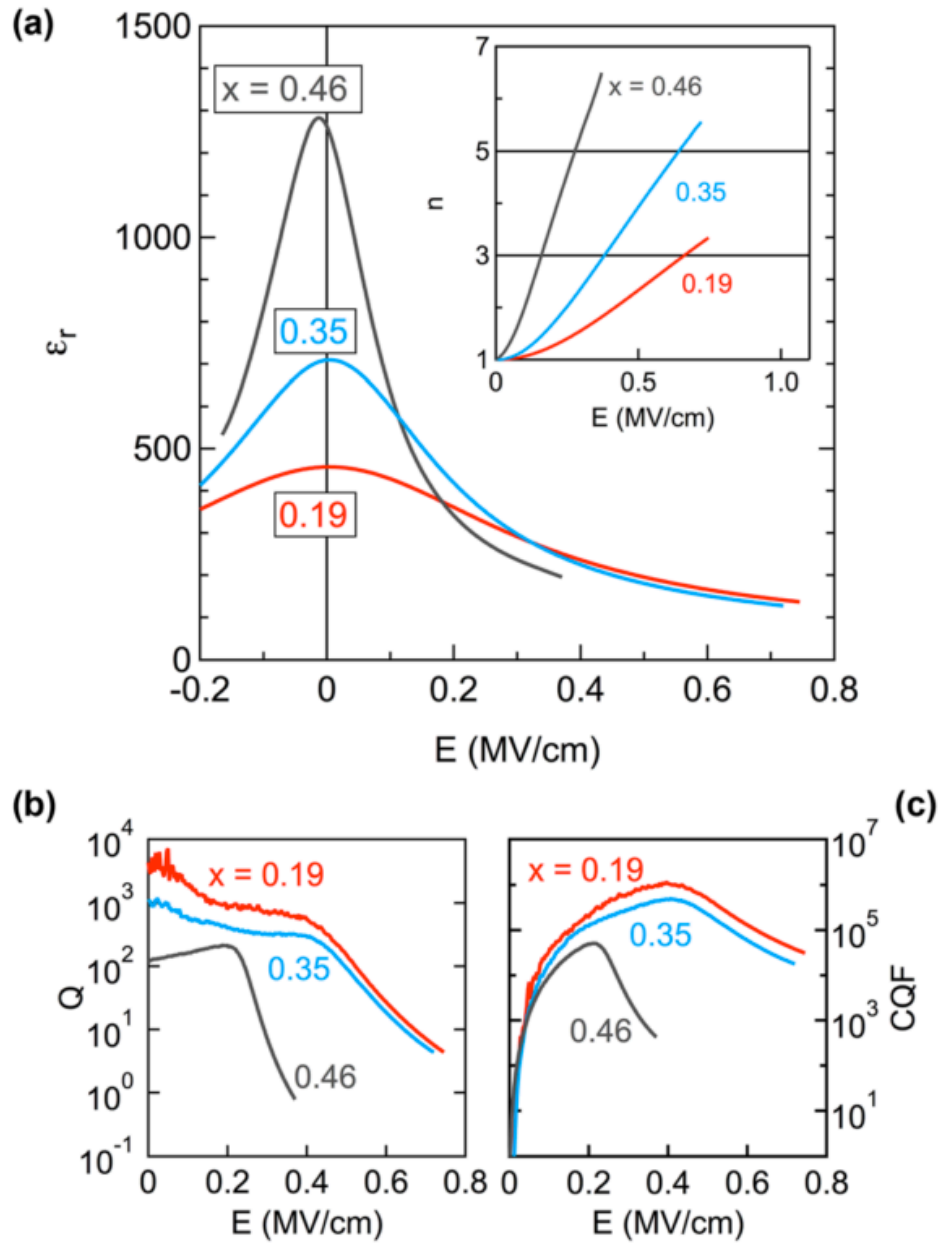
**Figure 4.8:** (a) Permittivity versus applied field (at 1 MHz) for parallel plate capacitors with $Ba_xSr_{1-x}TiO_3$ films with compositions $x = 0.19$, 0.35, and 0.46. Plots of $n(E)$ for each device are shown in the inset. The electric field dependence of (b) $Q$ and (c) the *CQF* see Eq. (8)) for each device. Reprinted with permission from [121]. Copyright 2012, AIP Publishing LLC

by the hybrid MBE approach allows for a drastic reduction in defects contributing to extrinsic loss, further validating the approach as a method to obtain superior A:B cation stoichiometry.

Comparison of $Q$ values for hybrid MBE-grown BST films with values from the literature are shown in Fig. 4.9a. The values of $Q$ for hybrid MBE-grown films exceed those of films grown by other methods as well as bulk ceramics and single crystals, though they are still clearly subject to the universal inverse relationship between $Q$ and permittivity (and thus tunability). The unprecedented values for $Q$ even for polycrystalline MBE-grown films suggests that the dielectric loss was mitigated primarily by the reduction of point defects in the interior of the film, and that extended defects, such as grain boundaries between grains of different orientations and dislocations at low-angle grain boundaries between (001)-oriented grains, contribute much less to the overall dielectric loss. Comparison of bulk polycrystalline ceramics with bulk single crystals also attests to the relatively innocuous effect of extended defects on the dielectric loss.

Figure 4.9b shows a comparison of the relative permittivity of samples in this study with thin films and bulk specimens in the literature. The permittivity of hybrid MBE-grown BST thin films is greater than that of thin films at similar compositions, instead tracking closely with that of polycrystalline bulk ceramics. This bulk-like behavior suggests minimal contributions from a dielectric dead layer. The high permittivity relative to other thin films also suggests a relatively low charged defect density within the interior of the film, since charged defects are expected to lower the permittivity by effectively introducing a space-charge layer [123]. The permittivity thus acts as an additional figure of merit suggesting superior stoichiometry in MBE-grown BST films.
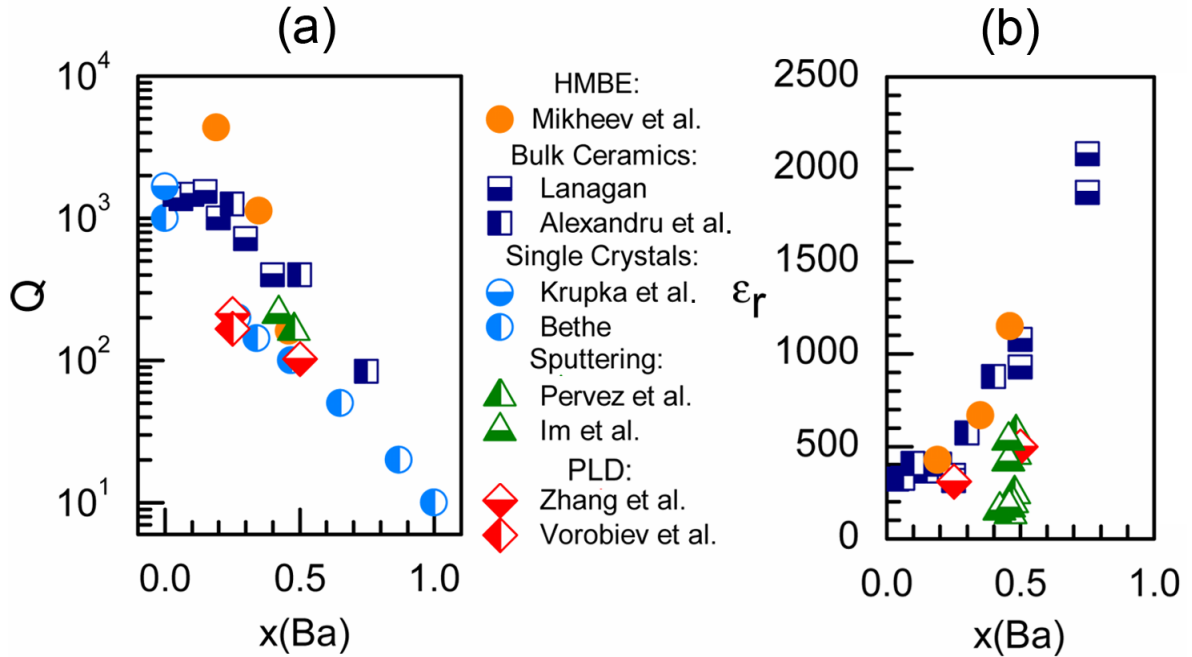
**Figure 4.9:** (a) Quality factor *Q* versus Ba composition *x* for BST samples from this study (Mikheev et al. [121]) and thin films (by sputtering and PLD), bulk ceramics and single crystals from the literature. Reprinted with permission from [121]. Copyright 2012, AIP Publishing LLC. (b) Comparison of permittivity of BST samples in this study with BST thin film and bulk specimens in the literature. Data was obtained from Lanagan [124], Alexandru et al. [125], Krupka et al. [126], Bethe [127], Pervez et al. [110], Im et al. [115], Zhang et al. [115] and Vorobiev et al. [111].

It is worth noting that the increase in $Q$ for hybrid MBE-grown films does not come at the expense of high tunability. The commutation quality factor ($CQF$) [128] is a figure of merit that is well-suited for the purpose of evaluating the combination of low loss and tunability in a tunable dielectric:

$$CQF = \frac{\left(n(E)-1\right)^2}{n(E)} Q(E)Q(0) \tag{8}$$

where $Q(E)$ is the quality factor at some applied field $E$ and $Q(0)$ is the quality factor at zero field. The $CQF$ of films with $x = 0.19$, 0.35, and 0.46 are shown in Fig. 4.8c. The maximum values for each are $1 \times 10^6$, $5 \times 10^5$, and $5 \times 10^4$, respectively. By comparison, typical values in the literature range from $10^1$-$10^4$ [129]. These values from the literature are reported for a wide range of frequencies, up to 1 GHz, whereas the values from the study in this chapter are reported for a frequency of 1 MHz. Due to the dominance of electrode-related losses at higher frequencies [122], extracting the losses arising exclusively from the BST films presented in this chapter is difficult beyond 1 MHz. However, the $Q$ factor from BST has been found to be largely independent of frequency between 1 MHz and 1 GHz [130]. As such, the comparison made here remains valid.


*4.7 Chapter Summary*

In this chapter, the stoichiometry optimization approach described in Chapters 2 and 3 was applied to the hybrid MBE growth of BST thin films. The observed trend in the lattice parameter of BST films grown on SrTiO$_3$ (001) substrates was found to be similar to that observed in homoepitaxial SrTiO$_3$ thin films, where the lattice parameter was a minimized under growth conditions giving optimal stoichiometry. This trend in the lattice parameter

was accompanied by a similar trend in the RHEED pattern, where a transition from a mixed termination, multi-domain (2 × 1) surface to a $TiO_2$-saturated c(4 × 4) to $TiO_2$-excess, multi-domain (2 × 1) surface was observed with increasing TTIP BEP for $Ba_{0.1}Sr_{0.9}TiO_3$. At higher Ba content, for $Ba_{0.46}Sr_{0.54}TiO_3$, the c(4 × 4) surface was no longer observed, instead the surface transitions from (1 × 1) to multi-domain (2 × 1) to (1 × 1) for Ti-poor, stoichiometric, and Ti-rich conditions, respectively.

The growth of BST films on epitaxial $Pt/SrTiO_3$ (001) bottom electrodes was investigated for the purpose of constructing parallel plate capacitors for dielectric characterization. Measurements of the dielectric properties of these capacitor structures reveal $Q$ factors that exceed those in thin films grown by PLD or sputtering by an order of magnitude and even exceed $Q$ factors of bulk ceramics and single crystals. This is attributed to a significant reduction in extrinsic defects in the films resulting in significantly lower dielectric loss. The behavior of $Q$ versus applied field $E$ for films with lower Ba content suggests that the intrinsic quasi-Debye mechanism dominates dielectric loss in these films. Large $Q$ factors in combination with high tunabilities in hybrid MBE-grown BST was shown to result in commutation quality factors that exceed any reported in the literature. The observations reported here collectively indicate that stoichiometry optimization with RHEED and XRD as described in Chapters 2 and 3 is valid for the growth of tunable BST films approaching the intrinsic limits of performance.

# Chapter 5

Growth and Electrical Transport Characterization of SrTi$_{1-x}$Zr$_x$O$_3$ Thin Films and Heterostructures

*5.1 Introduction*

Having established the validity of the stoichiometry optimization approach developed in Chapter 3 by applying it to the tunable dielectric $Ba_xSr_{1-x}TiO_3$ (as discussed in Chapter 4), the next step in realizing a modulation-doped $SrTiO_3$ heterostructure lies in the development of the doped barrier layer. As discussed in Chapter 1, $SrTi_{1-x}Zr_xO_3$ (STZO) stands as the primary candidate material for this function. This chapter will therefore present the results of the hybrid MBE growth of $SrTi_{1-x}Zr_xO_3$ using a metal-organic precursor for both Ti and Zr. Electrical transport in La:STZO and La:STZO/SrTiO_3 heterostructures will be discussed, with particular attention to Shubnikov-de Haas analysis. Portions of the work presented in this Chapter are published in [131].

*5.2 Experimental Details*

Heterostructures of $SrTiO_3$ and STZO were grown by hybrid MBE. $SrTiO_3$ layers were grown using the approach described in Chapter 3. Zr was supplied for the growth of STZO layers via the metal-organic precursor zirconium *tert*-butoxide (ZTB, 99.999% purity, Sigma-Aldrich). STZO films were grown by co-evaporating ZTB and TTIP metal-organic precursors, along with Sr from a solid-source effusion cell, in an RF oxygen plasma operating at 250 W in a background pressure of $4 \times 10^{-6}$ Torr. The ZTB delivery system was set up similarly to the TTIP delivery system described in Section 3.2. A substrate temperature of 900 °C, as measured by thermocouple (820 °C as measured by optical pyrometer), was used for all growths. The composition of STZO, *x*, was adjusted by adjusting the ZTB/B (BEP) ratio, where B (BEP) is the sum of TTIP BEP and ZTB BEP (i.e. the total B-cation precursor BEP). The composition was then determined by XRD and

RBS for various growth conditions. A:B cation stoichiometry (A = Sr) was then optimized by fixing ZTB/B (BEP) and adjusting the Sr BEP to achieve varying B/A (BEP) ratios. La dopants were supplied via a solid-source effusion cell, and dopant concentrations were calibrated by Hall measurements of La:SrTiO$_3$, in which a 1:1 correlation between La dopant concentration and charge carrier concentration was demonstrated previously [92]. A series of SrZrO$_3$ films was also grown by fixing the Sr BEP and adjusting the ZTB BEP. Growth was monitored *in-situ* with RHEED as described previously in Chapters 3 and 4. *Ex-situ* XRD measurements were performed similarly to the studies described in Chapters 3 and 4.

Structures intended for electrical transport measurements were post-growth annealed in 1 atm oxygen at 800 °C for 30 s in a rapid thermal annealing furnace to backfill oxygen vacancies and thus ensure oxygen stoichiometry. Ohmic contacts (40nm-Al/20nm-Ni/400nm-Au) were then deposited in a van der Pauw geometry (contacts on each corner of $10 \times 10 \times 0.5$ mm$^3$) samples by electron beam evaporation through a shadow mask. The longitudinal resistance ($R_{xx}$) and Hall resistance ($R_{xy}$, for magnetic fields of -1 T < B < 1 T) of these samples were measured from 300 K to 2 K in a Physical Properties Measurement System (PPMS, Quantum Design, Inc.) using the system's DC resistivity option (10 μA excitation current). Magnetoresistance measurements of select samples were performed in a He$^3$ cryostage at temperatures ranging from 0.45 K to 3 K using a standard AC lock-in technique for $B$ up to 14 T. Magnetoresistance measurements were also performed at various angles $\theta$, defined here as the angle between the magnetic field B and the sample surface normal ($\theta = 0°$ indicates that the magnetic field **B** is perpendicular to the sample surface), using a horizontal sample rotator stage.

*5.3 Growth of STZO*

Figure 5.1 shows the out-of-plane lattice parameters of ~65 nm thick STZO thin

films grown at various *B/A* BEP ratios for a fixed ZTB/B (BEP) = 0.25. The lattice

parameter of the STZO system explored here behaves differently from that of $SrTiO_3$ and

$Ba_xSr_{1-x}TiO_3$ films discussed in Chapters 3 and 4. Namely, in this system, the minimum

lattice parameter does not correspond to stoichiometric growth conditions. The *B/A* (BEP)

value marking the B-rich boundary is approximated from RBS data shown in Table I. All

films in Table I exhibit some amount of B cation excess (i.e. (Zr + Ti)/Sr > 1), which

increases with increasing *B/A* (BEP), as expected. The measured Zr incorporation (i.e.

Zr/(Zr + Ti)) gives a film composition of $x \approx 0.15$, which does not vary substantially (within

the limits of RBS measurements) for different values of *B/A* (BEP), which is similar to

reports on the growth of III-V solid solutions using multiple volatile precursors and various

V/III flux ratios [132]. The approximate boundary of the A-rich growth regime is marked in

Fig. 5.1 according to a combination of XRD and RHEED analysis to be discussed in some

detail below.

Figure 5.2 presents the RHEED patterns obtained after post-growth cooldown for

samples grown at various *B/A* (BEP) ratios. For *B/A* (BEP) = 47.0, nodes appearing on the

first-order reflections along both [100] and [110] azimuths, along with dim ½-order

reflections appearing in the pattern taken along the [110] azimuth (characteristic of a c(2 ×

2) surface reconstruction), are consistent with observations from $SrTiO_3$ and $Ba_xSr_{1-x}TiO_3$

thin films grown under A-cation-rich conditions. Increasing the *B/A* (BEP) ratio to 50.4

results in smooth streaks in the RHEED pattern and ½-order reflections observed along the

[100] azimuth, indicating a multi-domain (2 × 1) surface reconstruction. This clear, abrupt
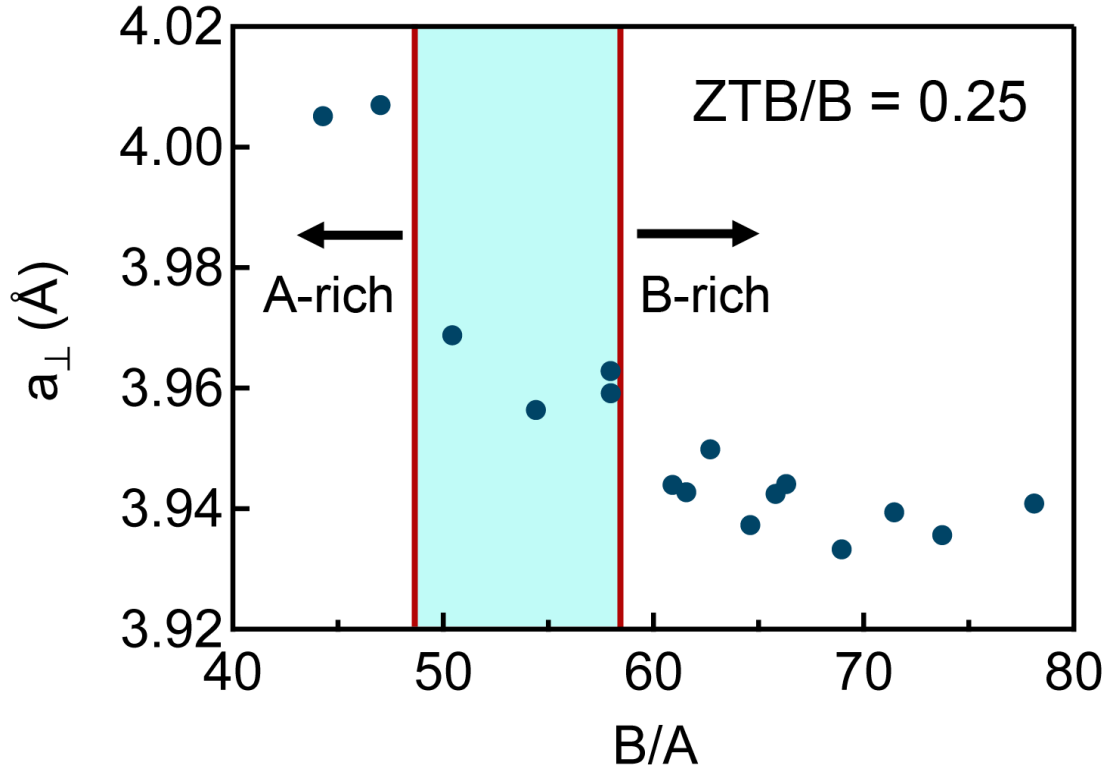
**Figure 5.1:** Out-of-plane lattice parameter of STZO films grown at a fixed ZTB/B (BEP) = 0.25 for various *B/A* (BEP) ratios. A-rich and B-rich growth regimes are shown with the approximate range of the stoichiometric growth regime shaded light-blue. The A-rich boundary was determined from RHEED and XRD analysis, whereas the B-rich boundary was determined by RBS analysis (see Table 4.1).

**Table 5.1:** *B/A* (BEP) ratio and corresponding Zr/(Zr + Ti) and (Zr + Ti)/Sr composition determined by Rutherford backscattering spectrometry (data collection courtesy of Dr. Leszek Wielunski, Rutgers University and analysis courtesy of Dr. Adam J. Hauser, University of California, Santa Barbara) for select STZO films grown at a ZTB/B (BEP) ratio of 0.25.

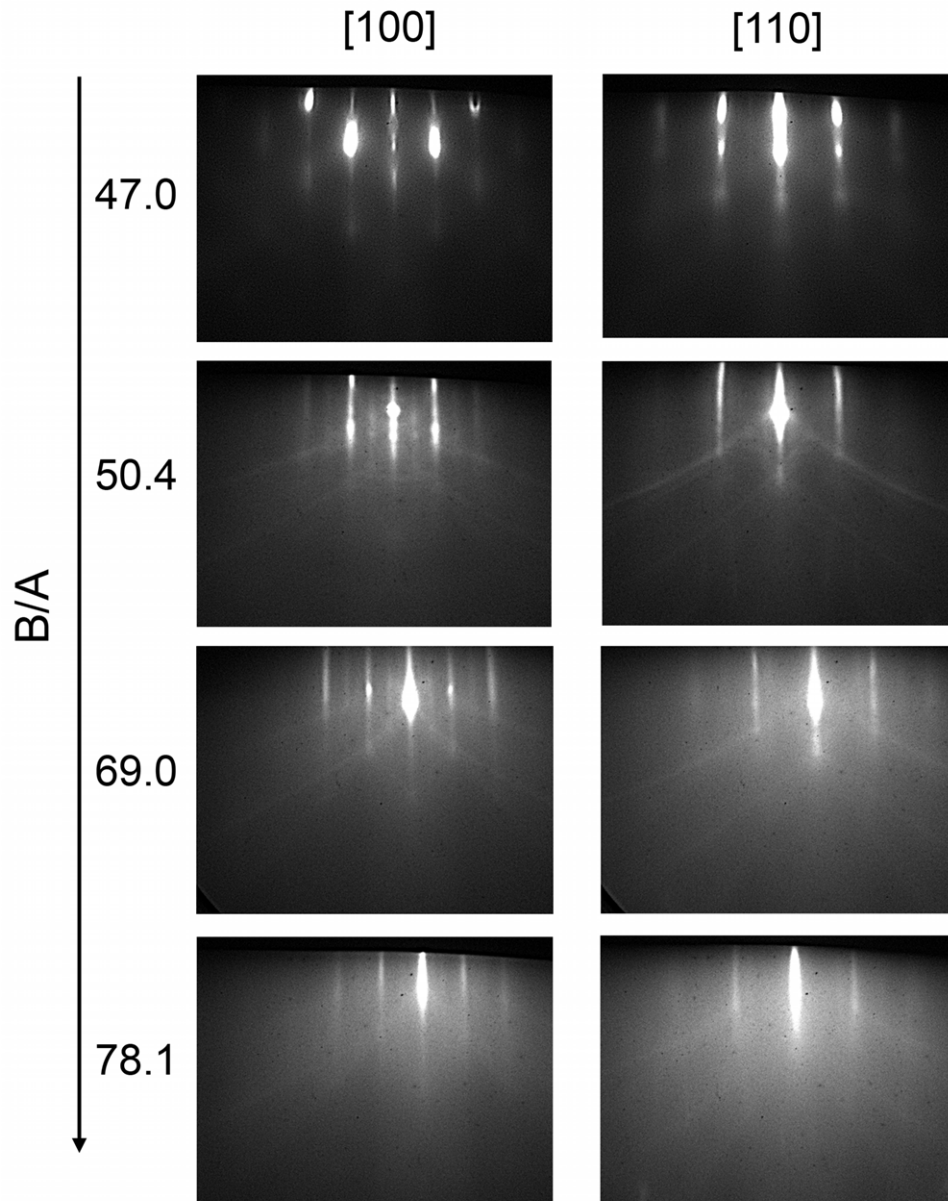| *B/A* (BEP) | (Zr + Ti)/Sr | Zr/(Zr + Ti) |
|---|---|---|
| 58 | 1.03 | 0.146 |
| 69.0 | 1.20 | 0.152 |
| 78.1 | 1.36 | 0.152 |

**Figure 5.2:** RHEED patterns captured after post-growth cooldown along the [100] and [110] azimuths of STZO films (ZTB/B (BEP) = 0.25) grown at various *B/A* (BEP) ratios.

shift from c(2 × 2) to (2 × 1) surface reconstruction suggests a possible shift from A-rich to stoichiometric growth conditions for *B/A* (BEP) between 47.0 and 50.4. The multi-domain (2 × 1) surface reconstruction persists up to *B/A* (BEP) = 69.0. Further increases in B/A result in the disappearance of the ½-order reflections along the [100] azimuth, giving a pattern consistent with a (1 × 1) surface (as shown for *B/A* (BEP) = 78.1). The RHEED pattern obtained for *B/A* (BEP) = 78.1 also exhibits a diffuse background reminiscent of SrTiO$_3$ thin films grown under conditions of extreme Ti excess.

Unlike in the hybrid MBE growth SrTiO$_3$ thin films, no c(4 × 4) surface reconstruction is observed in the RHEED pattern for any value of *B/A* (BEP) explored here. This may be the result of ZrO$_2$-terminated surface sites disrupting this particular reconstruction, which is characterized by an ordered TiO$_2$ network on pure SrTiO$_3$ [101]. As discussed in Chapter 3 for the growth of SrTiO$_3$, the multi-domain (2 × 1) surface reconstruction can be associated with either mixed SrO/TiO$_2$ termination within the growth window or with a purely TiO$_2$-terminated surface in a Ti-rich regime. Therefore, in the case of STZO, it is not clear from the trend in RHEED patterns alone whether the change in the surface lattice from (2 × 1) to (1 × 1) indicates a shift from stoichiometric conditions to B-rich conditions or whether this change is occurring entirely within the B-rich regime. The RBS data presented in Table I suggests the latter case.

Figure 5.3 shows the RHEED intensity from the specular (00) and 10 reflections along the [100] azimuth at the beginning of growth for STZO thin films with a ZTB/B (BEP) ratio of 0.25. Oscillations in the intensity suggest a layer-by-layer growth mode at the beginning of growth for all growth conditions explored here, even those at either extreme of cation excess. Similar to SrTiO$_3$ grown at lower TTIP/Sr (BEP) ratios within the XRD growth
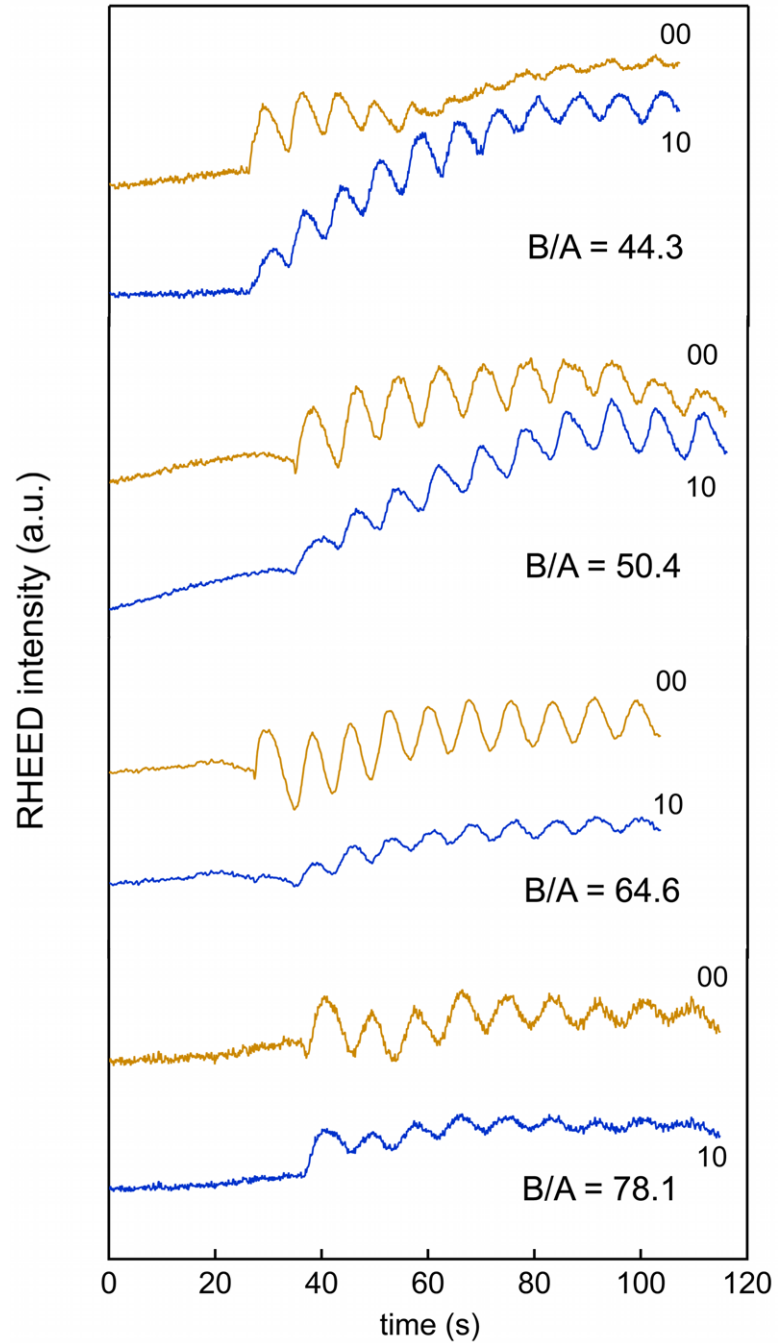
**Figure 5.3:** RHEED intensity from the specular (i.e. 00) and 10 reflections taken along the [100] azimuth of STZO films (ZTB/B (BEP) = 0.25) at the beginning of growth at various *B/A* (BEP) ratios.

window, growth of STZO in the A-rich regime leads to a shift or disruption of the RHEED intensity oscillations from the 00 reflection after ~5 oscillation periods, while oscillations from the 10 reflection remain unperturbed. For *B/A* (BEP) = 50.4 and above, there are no obvious changes in the observed RHEED intensity up to *B/A* (BEP) = 78.1, where the intensity oscillations from the 10 reflection may arguably decay more quickly than at lower *B/A* (BEP), possibly due to a substantial increase in the incorporation of excess B-cation species. For the purpose of A:B stoichiometry optimization, RHEED intensity oscillations may therefore allow for distinguishing A-rich growth conditions from stoichiometric and B-rich growth conditions. As is the case for $SrTiO_3$ growth, the shift from stoichiometric to B-rich growth conditions is not as apparent from RHEED intensity oscillations alone.

Figure 5.4 shows high-resolution XRD *2θ-ω* spectra measured in the vicinity of the $SrTiO_3$ 002 reflection for select STZO films from the same series presented in Fig. 5.1. For *B/A* (BEP) values that fall within the stoichiometric and even much of the B-rich growth regime, the STZO 004 film peak exhibits clearly defined thickness fringes, indicative of a smooth film of high structural quality. Only in the regime of extreme B-cation-excess (*B/A* (BEP) = 78.1) are the peak fringes noticeably disrupted in the vicinity of the film peak. Again, an abrupt shift is apparent from A-rich growth conditions (*B/A* (BEP) = 47.0) to nominally stoichiometric growth conditions. The spectrum presented for *B/A* (BEP) = 47.0 shows a STZO 004 peak that is accompanied by two additional peaks that may be associated with members of the Ruddlesden-Popper series of indeterminate order and Zr content. This markedly different structure in the A-rich regime probed by XRD is consistent with the change in the observed surface reconstructions by RHEED from A-rich to nominally stoichiometric conditions.
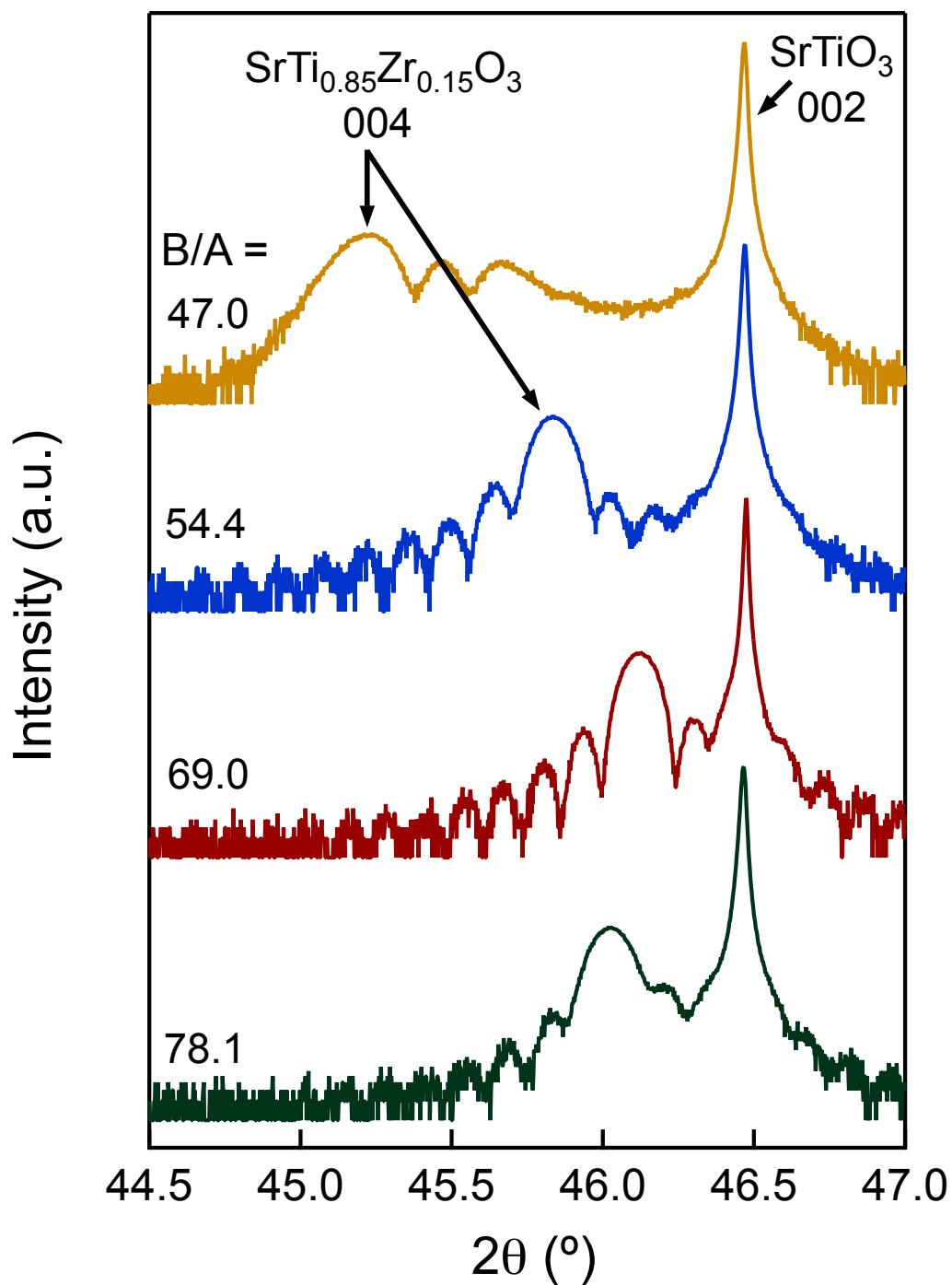
**Figure 5.4:** High-resolution XRD $2\theta$-$\omega$ scans in the vicinity of the $SrTiO_3$ 002 substrate peak for ~65 nm thick STZO films (ZTB/B (BEP) = 0.25) grown at various *B/A* (BEP) ratios.

It is worth noting that no apparent qualitative change in the XRD spectrum is observed when transitioning from stoichiometric to B-rich growth regimes. Even for $B/A$ (BEP) = 69.0, which is well within the B-rich growth regime (~20% B-cation excess as measured by RBS), the STZO 004 film peak still exhibits well-defined thickness fringes, suggesting that the cation excess is accommodated so as to not substantially disrupt the STZO film structure. In the case of $Ba_xSr_{1-x}TiO_3$, excess Ti was shown [100] to be accommodated by the formation of amorphous $TiO_x$ phases. For the STZO films investigated here, amorphous $BO_x$ phases, with B being some combination of Ti and Zr, may similarly form to accommodate the B-cation excess. Depending on the distribution of these amorphous phases, the crystalline portion of the STZO film may remain highly ordered with smooth surfaces and interfaces, and the amorphous phases may have a negligible effect on the measured XRD spectrum. This may not hold true for sufficiently high B-cation excess, as is suggested by the XRD spectrum measured for $B/A$ (BEP) = 78.1.

Comparing the above observation with the decrease in the lattice parameter observed in Fig. 5.1 for increasing $B/A$ (BEP) gives additional clues into the nature of STZO growth in the B-cation-excess regime. Reciprocal space map (RSM) measurements indicate that films in this regime up to $B/A$ (BEP) = 69.0 are coherently strained to the substrate, so the decrease in lattice parameter does not appear to be due to the films becoming progressively more relaxed with increasing $B/A$ (BEP). Instead, it is possible that with increasing $B/A$ (BEP), more Zr is preferentially rejected into the amorphous phase, resulting in a crystalline phase with lower Zr content (and thus lower lattice parameter) that is still coherently strained to the substrate. It is then possible that the overall Zr incorporation into the film does not appear to change according to RBS, even if the incorporation into the crystalline

phase does change. Furthermore, the incorporation of an alloying element in the growth of III-V semiconductor thin films by gas-source MBE has been shown to change depending on strain in a pseudomorphic film [133], which may also be relevant here. For instance, accomodating the B-cation excess with equal fractions of Ti and Zr in both crystalline and amorphous phases would likely lead to greater strain due to lattice expansion from B-cation excess (as is the case for $SrTiO_3$), which would change the preferred distribution of Zr and Ti in both phases. As a result, with increasing B-cation excess (higher $B/A$ (BEP)), relatively higher amounts of Zr might be preferentially rejected into the amorphous phase to accommodate the strain in the crystalline phase from B-cation excess. Further investigation on the distribution of Zr and Ti in the film grown under these conditions would be needed to determine how accurately this describes the system, but within the scope of this study, it suffices to say that alloying with a volatile precursor may complicate investigations into growth of STZO compared to alloying with a second solid source, as was the case for $Ba_xSr_{1-x}TiO_3$ (see Chapter 4).

To summarize the findings on the growth of STZO, it has so far been shown that the transition from A-rich growth conditions to nominally stoichiometric growth conditions can be easily discerned with XRD and RHEED. The transition from stoichiometric to B-rich growth conditions is much less apparent; it can only be readily discerned from measurements of the chemical composition (RBS in this case). Considering the somewhat cumbersome nature of obtaining and analyzing RBS data, A:B stoichiometry optimization can be more readily effected by using the A-rich growth regime as a reference, with sufficient care taken to not grow too far into B-cation excess. For the purpose of doping and

transport studies to be discussed in subsequent sections, A:B stoichiometry was optimized to the extent possible based on the above analysis.

*5.4 Growth of SrZrO₃*

Prior to discussing the electrical properties of La:STZO thin films and heterostructures, the growth of $SrZrO_3$ will be briefly discussed in this section. Because of the large lattice mismatch between $SrZrO_3$ and $SrTiO_3$ (~5%), only very thin films (~10 nm or thinner) are practical for the growth of high-quality heterostructures for transport. The critical thickness of $SrZrO_3$ on $SrTiO_3$ was not investigated here. Because the XRD-based approach used for the optimization of $SrTiO_3$, $Ba_xSr_{1-x}TiO_3$, and STZO discussed previously is of more limited utility for such thin films, this section will thus only focus on trends observed in RHEED.

Figure 5.5 shows RHEED patterns taken along the [100] and [110] azimuths of ~10 nm $SrZrO_3$ thin films grown at various ZTB/Sr (BEP) ratios on $SrTiO_3$ (001) substrates. The RHEED pattern for the film grown at ZTB/Sr (BEP) = 113.4 exhibits a (1 × 1) surface lattice with bulging in the first-order reflections along the [100] azimuth, characteristics reminiscent of Sr-rich $SrTiO_3$. Increasing the ZTB BEP to give ZTB/Sr (BEP) = 118.0 results in a RHEED pattern with ½-order reflections along both [100] and [110] azimuths, which suggests a (2 × 2) surface reconstruction. Increasing the ZTB/Sr (BEP) ratio further to 125.5 results in a (1 × 1) surface. Spotty features visible from films grown at ZTB/Sr (BEP) = 118.0 and 125.5 may be related to some combination of relaxation-related defects and/or the nucleation of $ZrO_2$ crystallites on the surface. This latter point is consistent with the features being more exaggerated at higher ZTB/Sr (BEP) ratios for films with nominally the same thickness.
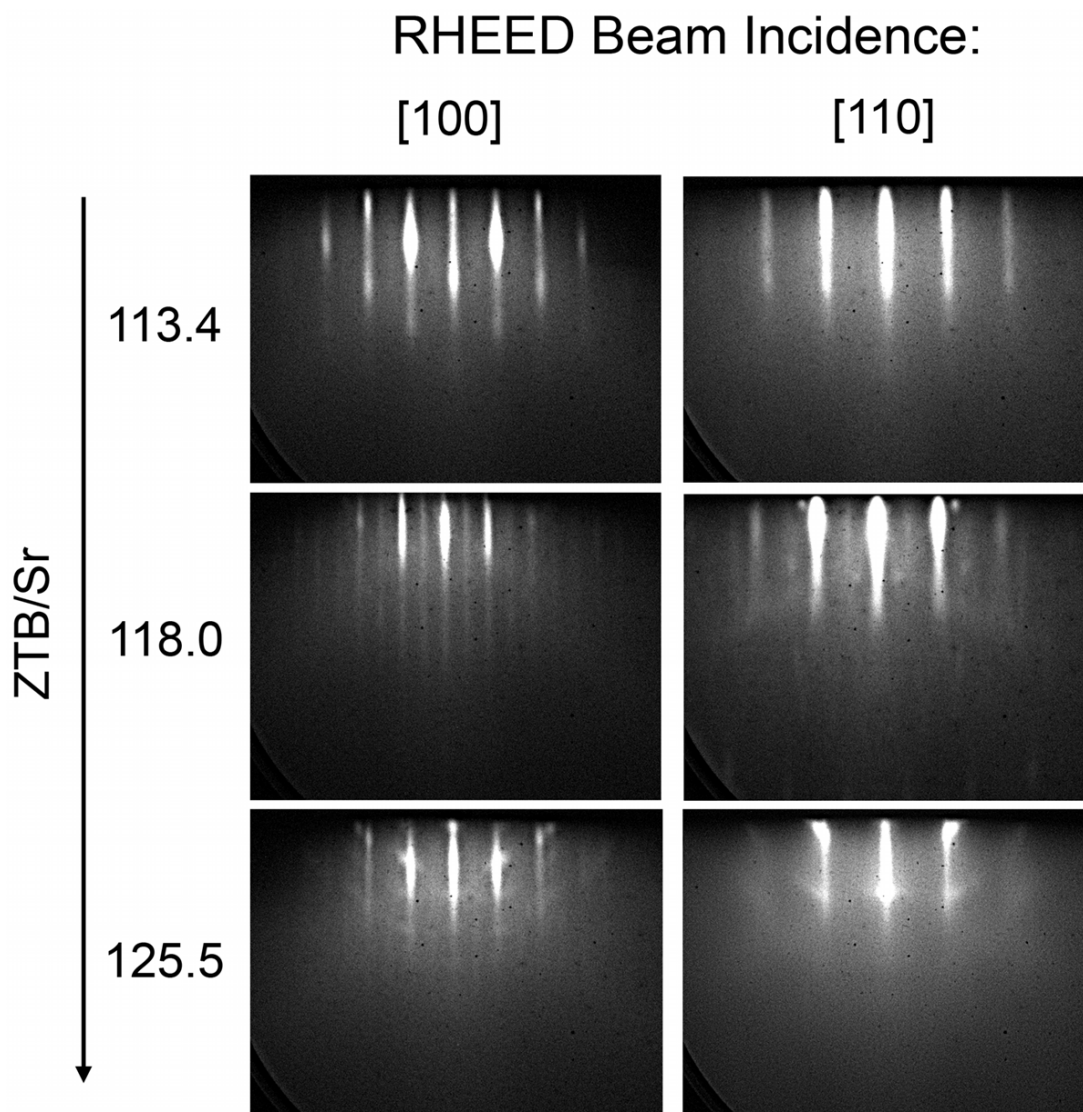
**Figure 5.5:** RHEED patterns obtained along the [100] and [110] azimuths of ~10 nm SrZrO$_3$ thin films grown on SrTiO$_3$ (001) substrates at various ZTB/Sr (BEP) ratios.

Figure 5.6 shows the RHEED intensity oscillations taken from the specular (00) and 10 reflections along the [100] azimuth at the beginning of growth for $SrZrO_3$ films grown at various ZTB/Sr (BEP) ratios. For the 10 reflection at ZTB/Sr (BEP) = 113.4, ~6 RHEED intensity oscillation periods are completed before the oscillations are extinguished; these oscillations are accompanied by a hump in the background intensity for the 00 and 10 reflections. At ZTB/Sr (BEP) = 118.0, the oscillations from the 10 reflection persist for the entirety of the growth (~23 oscillation periods), and the transient increase in the background intensity observed at ZTB/Sr (BEP) = 113.4 is not observed at the beginning of growth for ZTB/Sr (BEP) = 118.0. Increasing ZTB/Sr (BEP) to 125.5 results in oscillations that decay rapidly, extinguishing within ~10 oscillation periods. Again, no transient increase in the background intensity is observed at ZTB/Sr (BEP) = 125.5. This behavior suggests that ZTB/Sr (BEP) ratios of 113.4 and 125.5 fall within Sr-rich and Zr-rich growth regimes, respectively, where the accumulation of defects from excess of the respective cation disrupts the layer-by-layer growth, thus extinguishing the intensity oscillations. The hump in background intensity observed at ZTB/Sr (BEP) = 113.4 (as well as lower ZTB/Sr, though not shown here) can thus be associated with growth of $SrZrO_3$ in the Sr-rich regime. Although a phase shift in the oscillations from the 00 reflection occurs for ZTB/Sr (BEP) = 118.0 so as to place the 00 and 10 intensity oscillations ~$\pi$ rad out of phase with one another (associated with growth in Sr-rich conditions, see Chapter 3), the persistence of the intensity oscillations suggests that this BEP ratio is close to stoichiometric growth conditions for $SrZrO_3$ on $SrTiO_3$ (001).

Based on the observed trend in the RHEED patterns and reflection intensities measured at the beginning of growth, one may place the stoichiometric growth conditions for $SrZrO_3$
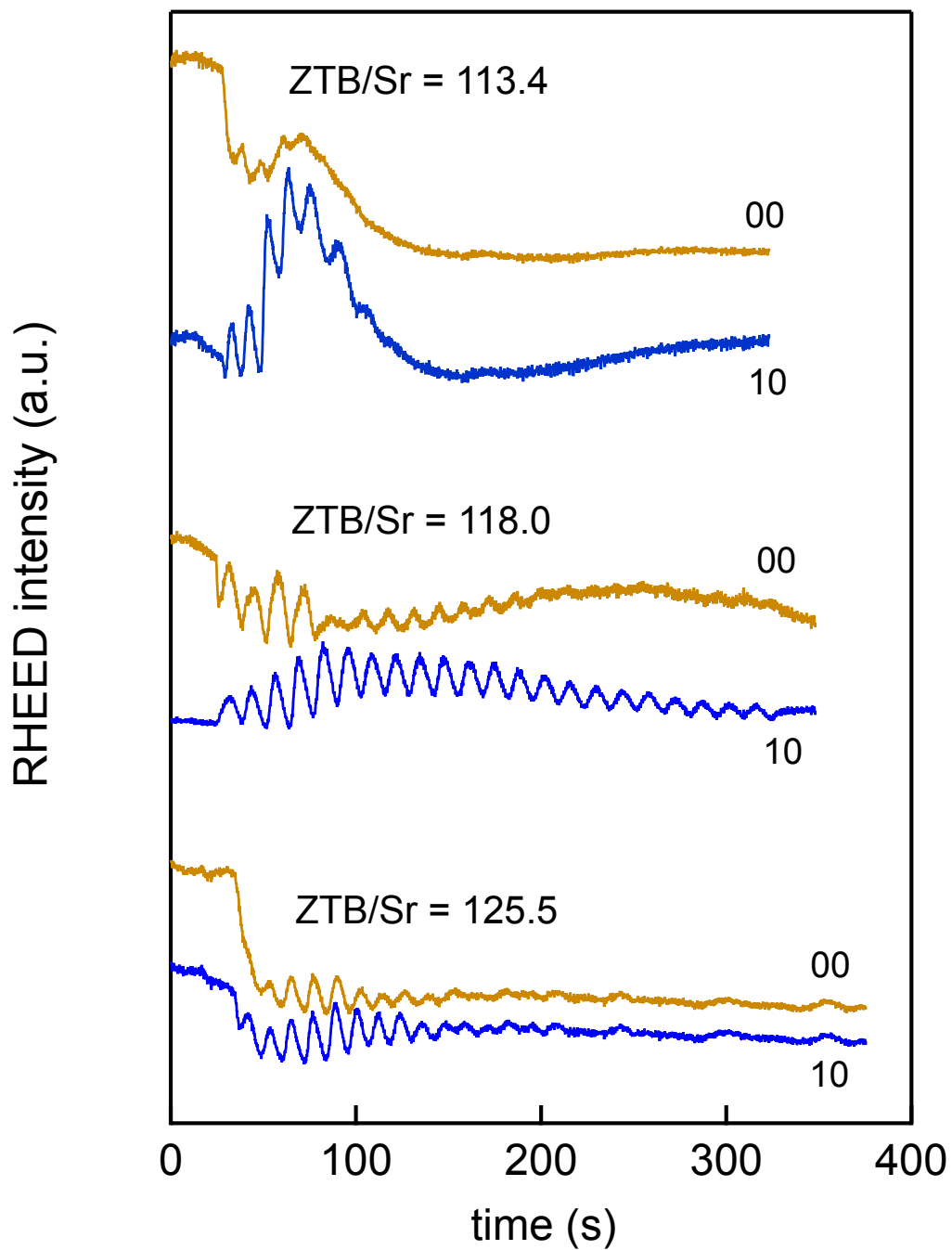
**Figure 5.6:** RHEED intensity from the specular (00) and 10 reflections taken along the [100] azimuth of SrZrO₃ films during growth at various ZTB/Sr (BEP) ratios.

between ZTB/Sr (BEP) = 113.4 and 125.5 at substrate temperature and oxygen background given in Section 5.2. In addition, a $(2 \times 2)$ surface reconstruction is associated here with films grown under nominally stoichiometric conditions. Growth of $SrZrO_3$ thin films both with and without oxygen background and growth on $(LaAlO_3)_{0.3}(Sr_2AlTaO_6)_{0.7}$ (LSAT) (001) substrates both show similar results, though more detailed studies will be left for future work.

*5.5 Electron doping and Transport in La:STZO and SrTiO₃/La:STZO*

Following the growth optimization study described in Section 5.3, electron doping with La was attempted for films with ZTB/B (BEP) = 0.25 at various *B/A* (BEP), using the following structure: $SrTiO_3$ substrate/ 20 nm STZO/ 65 nm La:STZO ($n_{La} \sim 2 \times 10^{20}$ cm$^{-3}$). All samples (ranging from *B/A* (BEP) = 53 to 69.0) were insulating, with room temperature resistivity greater than the measurement limit of both the PPMS resistivity option and standard multimeters. There are many possible factors that may prevent these STZO films from being amenable to electron doping, such as defects or perhaps the shifting of the conduction band relative to the La dopant level, which would prevent dopant ionization. $SrZrO_3$ is a trivial insulator with a very large band gap and no known shallow donor impurity species [134], so it is reasonable to expect that STZO may also act as an insulator with sufficiently high Zr content.

STZO films were only successfully doped once ZTB/B (BEP) was reduced to 0.13 or below, corresponding to ~5% Zr substitution or lower. To investigate transport in STZO alone, prior to interfacing with $SrTiO_3$, structures with the configuration shown in Fig. 5.7d were grown. The 25 nm undoped STZO spacer was included to minimize charge transfer

into the $SrTiO_3$ substrate. The temperature dependence of the sheet resistance ($R_S$), 3D

charge carrier Hall density ($n_{3D}$), and electron Hall mobility ($\mu$) of two such samples, each

grown at a different ZTB/B (BEP), is shown in Figs. 5.7a, 5.7b, and 5.7c, respectively. The

carrier densities of $2 \times 10^{20}$ cm$^{-3}$ and $1 \times 10^{20}$ cm$^{-3}$ in these structures grown at ZTB/B

(BEP) = 0.07 and 0.13, respectively, are commensurate with values expected for La doping

calibrations performed with homoepitaxial $SrTiO_3$. It should be noted that for this structure,

lower doping concentrations and off-stoichiometric growth results in insulating films whose

Hall coefficient (and thus Hall mobility) could not be determined.

For both samples, $R_S$ decreases with decreasing temperature down to ~100 K, below

which the $R_S$ either remains constant for ZTB/B (BEP) = 0.07 or begins increasing with

decreasing temperature for ZTB/B (BEP) = 0.13 (see Fig. 5.7a). The flattening of $R_S$ for

ZTB/B (BEP) = 0.07 is expected when ionized impurity scattering dominates at lower

temperatures [135]. This same mechanism is likely contributing to transport in the structure

grown at *ZTB/B (BEP)* = 0.13 as well, though some other mechanism, perhaps related to the

$SrTiO_3$ structural transition at ~110 K, may be causing the change in the temperature

dependence of $R_S$ below at ~100 K. For ZTB/B (BEP) = 0.13, this change from metallic to

insulating behavior in $R_S$ is also accompanied by a decrease in the apparent charge carrier

density with decreasing temperature for the same temperature range (see Fig. 5.7b). This

change in carrier density does not give a linear relationship in $\ln(n_{3D})$ versus $T^{-1}$, which

would suggest charge carrier trapping by defects or carrier freeze-out in this structure. As

such, the behavior of $R_S$ and $n_{3D}$ with temperature, shown here, is not yet well understood.

That being said, the values of $\mu$ at 2 K for both samples is at least an order of magnitude
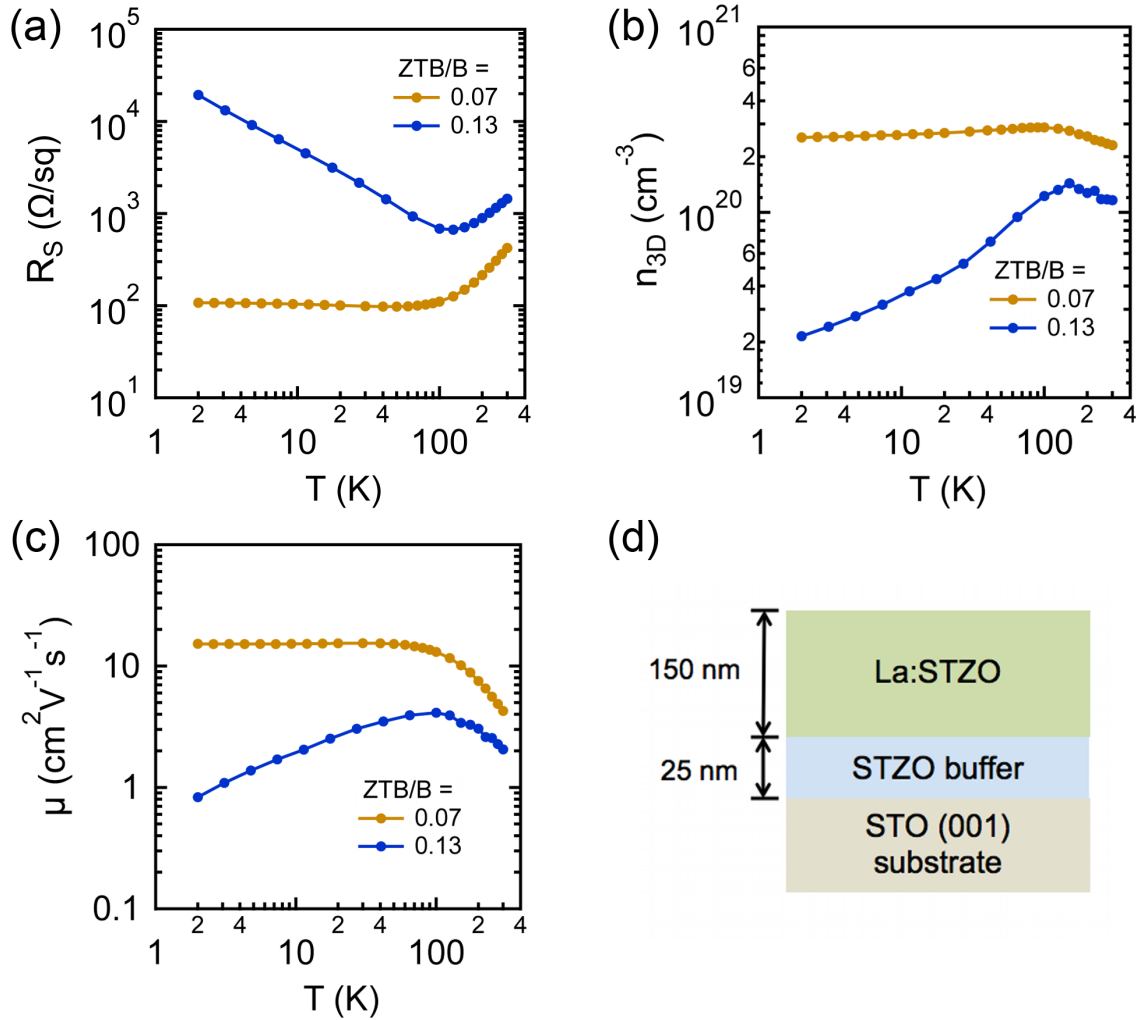
**Figure 5.7:** (a) Sheet resistance, $R_S$, (b) 3D charge carrier Hall density, $n_{3D} = 1/(eR_H t_{STZO})$, where $t_{STZO}$ is the La:STZO layer thickness, and (c) Hall mobility, $\mu$, determined as a function of temperature for La:STZO thin film heterostructures grown at different ZTB/B (BEP) and described schematically in (d). The value of $n_{3D}$ measured at T = 300 K for each sample is consistent with the expected value from La doping calibrations in SrTiO$_3$.

lower than in $SrTiO_3$ for comparable doping densities [93], most likely due to alloy scattering from the substituted Zr.

Following a brief study of electronic transport in thick La:STZO films, modulation doped structures were grown with the configuration shown in Fig. 5.8. The STZO composition of ~5% was achieved with ZTB/B (BEP) = 0.13 and was determined by XRD. A band diagram was drawn for the structure shown in Fig. 5.8 based on the energy of the conduction band edge, valence band edge, and Fermi level calculated using a 1D Poisson solver [136]. For STZO with $x = 0.05$, a conduction band offset, $\Delta E_C$, of 95 meV was estimated by Vegard's law. The La:STZO layer in the structures discussed below have a dopant concentration of $\sim 2 \times 10^{19}$ $cm^{-3}$, which is the lower limit of doping that results in a conductive film. For this particular configuration, a 2DEG is predicted to reside at the interface. La:STZO layers of the same dopant density with a thickness below 30 nm or lower dopant density in 30 nm La:STZO layers on $SrTiO_3$ resulted in insulating films, most likely due in large part to surface depletion. It should be noted that conductive heterostructures could be realized at a lower dopant density when La:STZO is directly interfaced with $SrTiO_3$, compared to structures like that shown in Fig. 5.7d. This may be due to the charge carrier trapping in undoped STZO layers or partial relaxation in thicker STZO films, though a conclusive explanation remains elusive.

The temperature dependence of $R_S$, $n_{3D}$, and $\mu$ of modulation doped structures "MA" and "MB" are shown in Figs. 5.9a, 5.9b, and 5.9c, respectively. The 3D density $n_{3D}$ is presented here rather than the 2D density for the purpose of comparison with thicker La:STZO. MA and MB are structures with La:STZO layers grown under similar growth conditions: *B/A* (BEP) = 52.3 for MA and *B/A* (BEP) = 53.2 for MB, all other parameters being equal. A
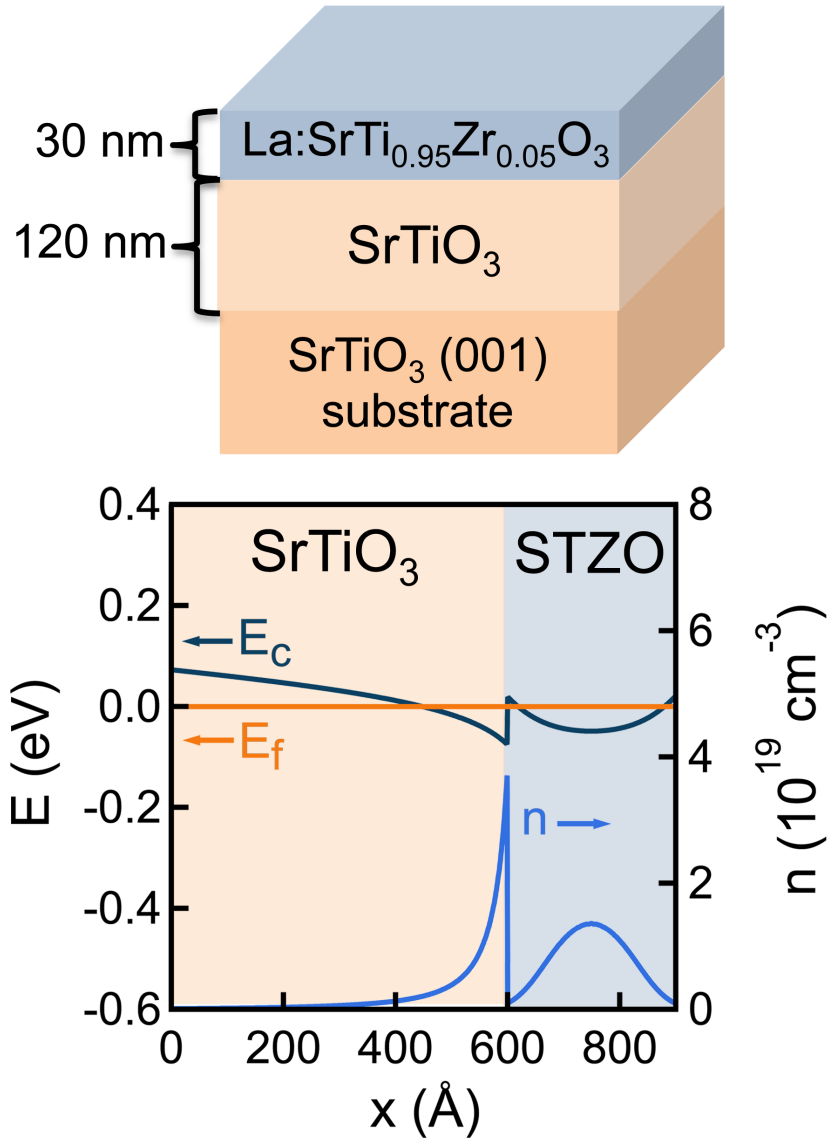
**Figure 5.8:** Schematic of a modulation doped $SrTiO_3$/La:$SrTi_{0.95}Zr_{0.05}O_3$ (La:STZO) heterostructure, along with the corresponding band diagram. The position of the conduction band edge ($E_C$) relative to the Fermi level ($E_f$) and the corresponding carrier density were calculated using a 1D Poisson solver [136]. The conduction band offset between La:STZO and $SrTiO_3$ was estimated using the experimentally-determined $SrZrO_3$-$SrTiO_3$ conduction band offset [42] and assuming a Vegard's law dependence with Zr content. For the calculation, a dopant density of $2 \times 10^{19}$ $cm^{-3}$ was assumed for La:STZO, and a surface pinning potential of 0.1 eV was used. A residual donor-type defect density of $10^{16}$ $cm^{-3}$ was assumed for $SrTiO_3$, which is consistent with previous doping studies. Adapted with permission from [131]. Copyright 2013, AIP Publishing LLC.
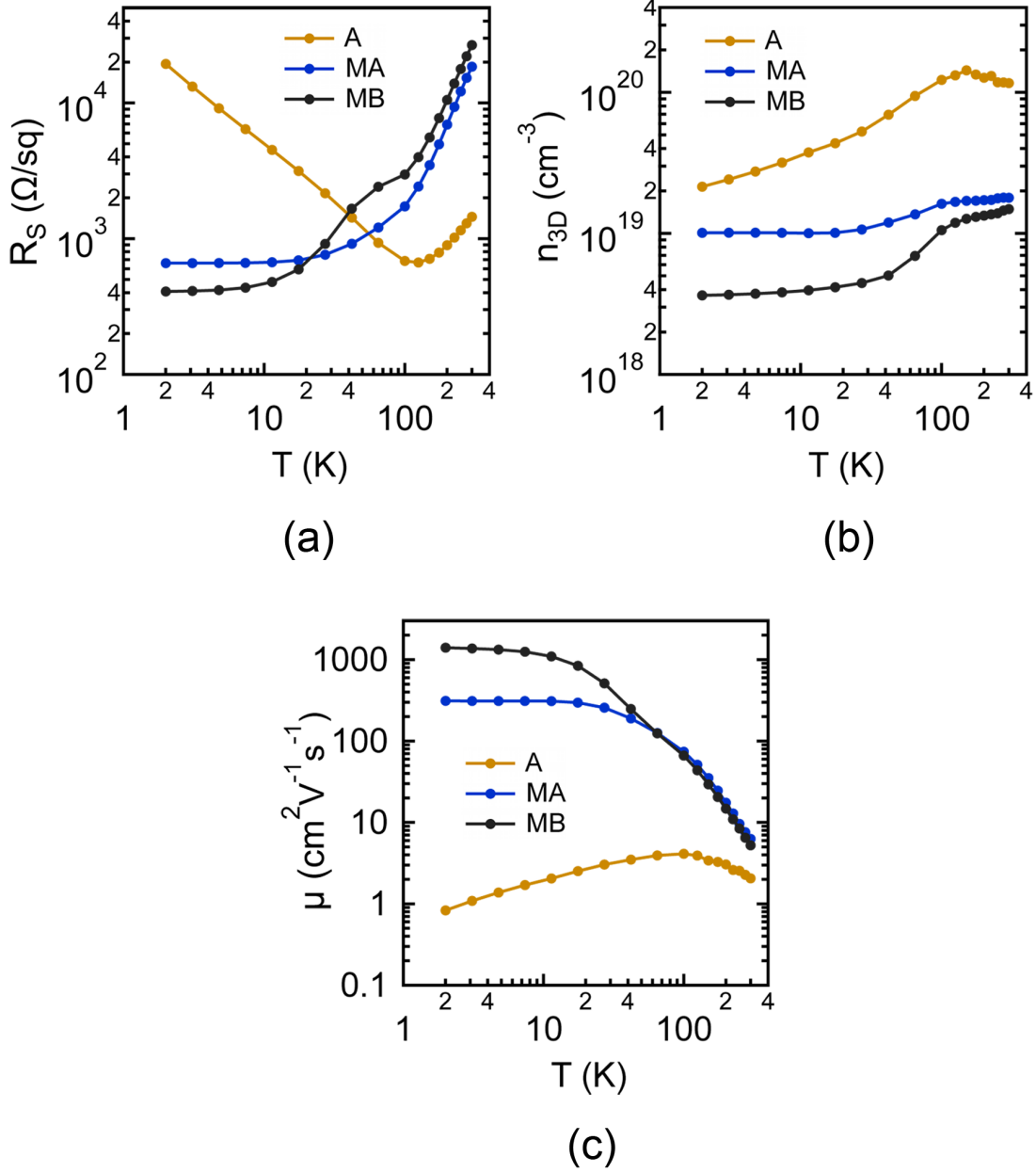
**Figure 5.9:** (a) Sheet resistance, $R_S$, (b) 3D charge carrier Hall density, $n_{3D} = 1/(eR_H t_{STZO})$, where $t_{STZO}$ is the La:STZO layer thickness, and (c) Hall mobility, $\mu$, determined as a function of temperature for modulation doped heterostructures "MA" and "MB", which were grown with the structure schematically described in Fig. 5.8. MA and MB differ only by the growth conditions of the La:STZO layer: $B/A$ (BEP) = 52.3 for MA and $B/A$ (BEP) = 53.2 for MB. Sample "A" is the same sample presented for ZTB/B (BEP) = 0.13 in Fig. 5.7 and is included here for comparison.

sample grown at *B/A* (BEP) = 51.1 showed similar transport behavior and mobility as sample MB, and any such structures grown at *B/A* (BEP) < 51.1 and *B/A* (BEP) > 53.2 were insulating. Transport data for sample "A" is the same as that shown for ZTB/B (BEP) = 0.13 in Fig. 5.7 and is included in Fig. 5.9 for comparison.

Despite similar growth conditions, samples MA and MB exhibit significant differences in transport behavior. Although both heterostructures show relatively constant $R_S$ versus temperature below 10 K, MB shows a hump in $R_S$ just below 100 K, whereas MA does not. MB also exhibits a Hall mobility at 2 K that is ~4 times greater than that of MA. However, both exhibit a drop in the apparent carrier density upon cooling from 300 K to 2 K: a 45% decrease for MA and a 75% decrease for MB. This apparent change in the carrier density is most likely due to multi-carrier conduction and the different temperature dependencies of the mobilities of different carrier types, which can alter the measured Hall coefficient near zero-field so as to lower the apparent carrier density [4]. Multi-carrier conduction is expected for this system as shown in Fig. 5.8, where higher mobility charge carriers at the $SrTiO_3$ side of the interface conduct in parallel with residual carriers in the La:STZO.

Comparing MA and MB to sample A already suggests an increase in mobility from charge transfer into the undoped $SrTiO_3$ buffer. Although it may be difficult to compare sample A to samples MA and MB due to differing 3D densities, it is still informative to compare them using uniformly-doped La:$SrTiO_3$ as a reference. For example, the 2 K Hall mobilities of MA and MB are approximately 2-3 orders of magnitude greater than that of sample A. A comparable change in the carrier density from ~$1 \times 10^{20}$ cm$^{-3}$ to ~$2 \times 10^{19}$ cm$^{-3}$ in uniformly-doped La:$SrTiO_3$ results in only 1 order of magnitude increase in the low-temperature mobility [93]. As such, some of the improvement in mobility may be due to a

lower 3D density, but that does not account for the additional 1 or 2 orders of magnitude

increases in mobility comparing the sample configuration of A to MA and MB.

This analysis alone does not conclusively confirm the formation of a 2DEG in $SrTiO_3$ by

modulation doping. To do this requires the analysis of the angle-dependence of Shubnikov-

de Haas oscillations, which will be discussed in the subsequent section. It should be noted

that while sample MB exhibits Shubnikov-de Haas oscillations at temperatures below 3 K,

sample MA does not (to magnetic fields as high as $B = 14$ T). It is not clear why these

samples exhibit such significant differences in transport behavior despite very similar

growth conditions. It is possible that the optimal growth conditions for this type of

heterostructure fall within a narrow range of $B/A$ (BEP); deviations from the ideal conditions

result in lower mobilities or insulating films depending on the extent of deviation from

cation stoichiometry. Whatever the case may be, the electronic structure of MB will be

investigated with Shubnikov-de Haas analysis in the following section.


*5.6 Shubnikov-de Haas Analysis of $SrTiO_3$/La:STZO*

Figure 5.10 shows the longitudinal magnetoresistance for sample MB, with the structure

sketched schematically in Fig. 5.8, at temperatures ranging from 0.45 K to 3 K. Oscillations

in $R_{xx}$ are observed for temperatures of 3 K and below; at 0.45 K, oscillations become

visible for $B > 5$ T. The observation of magnetoresistance oscillations in this structure is

itself a strong indication of charge transfer into the undoped $SrTiO_3$ layer, since the mobility

in the La:STZO layer has been shown in previous sections to be too low to resolve

magnetoresistance oscillations as a result of alloy scattering. Oscillations are also not

observed in La:SrTiO$_3$ with comparable dopant densities due to scattering from ionized dopants.

To extract more information about the electronic structure, the magnetoresistance background was subtracted using multiple polynomial fits, yielding the oscillatory component of the magnetoresistance, $\Delta R_{xx}$. Figure 5.11a shows $\Delta R_{xx}$ versus $1/B$ for this sample measured at 0.45 K. A fast-Fourier transform (FFT) of this data is presented in the inset, with multiple peaks indicating the presence of multiple oscillating components. These oscillating components may arise from either multiple subbands (and their harmonics) or from spin splitting of fewer subbands. More detailed analysis of the electronic structure from this data will be discussed below.

Figure 5.11b shows $\Delta R_{xx}$ measured for this sample at 2 K at multiple tilt angles $\theta$, plotted against the inverse perpendicular component of the magnetic field, $(B\cos\theta)^{-1}$. For tilt angles up to 60°, minima and maxima in $\Delta R_{xx}$ coincide for the same values of $(B\cos\theta)^{-1}$. This is an unambiguous indicator of the 2D nature of the electronic structure. It suggests a 2D density of states confined to the plane of the interface whose corresponding Landau level spacing and degeneracy depend only on the component of the magnetic field perpendicular to the interface due to the restriction of out-of-plane cyclotronic motion. Based on the 2D nature of this system and the low mobility of charge carriers in STZO, one can conclude that a 2DEG has been formed in SrTiO$_3$ by modulation doping.

As discussed in Chapter 1, many important properties of the electronic structure can be extracted from Shubnikov de-Haas oscillations. For oscillations arising from a 2DEG with a single electronic subband, the decay in the amplitude of the oscillations with temperature depends on the effective mass of the carriers. Similarly, using a Dingle plot to track the

**Figure 5.10:** Longitudinal magnetoresistance ($R_{xx}$) measured from sample MB (see Figs. 5.8 and 5.9) at temperatures between 0.45 K and 3 K. Adapted with permission from [131]. Copyright 2013, AIP Publishing LLC.
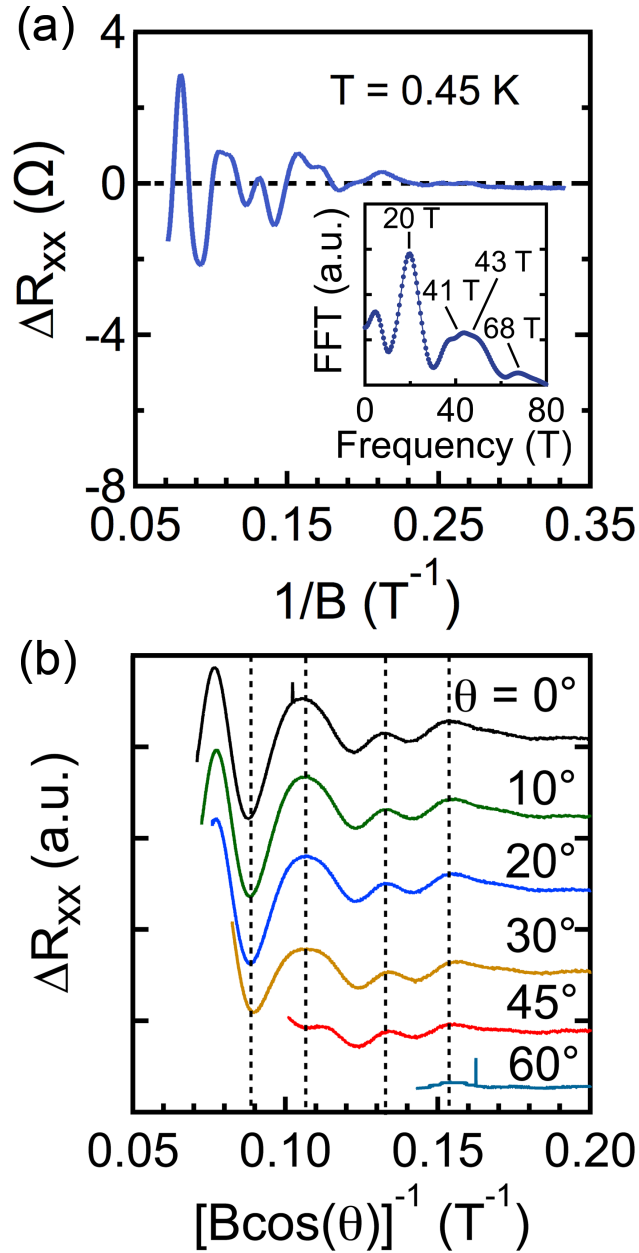
**Figure 5.11:** (a) Shubnikov-de Haas oscillations, $\Delta R_{xx}(1/B)$, extracted from the longitudinal magnetoresistance measured in sample MB (see Figs. 5.8 and 5.9) at 0.45 K. A Fourier transform of this data along with the approximate positions of the peaks is shown in the inset. (b) $\Delta R_{xx}$ measured at 2 K and plotted against the inverse of the component of the magnetic field $B$ that is perpendicular to the interface, $[B\cos(\theta)]^{-1}$, for various tilt angles $\theta$. Adapted with permission from [131]. Copyright 2013, AIP Publishing LLC.

decrease in oscillation amplitude with inverse field yields the Dingle temperature ($T_D$, related to the quantum scattering time $\tau_q$). In this system, where oscillations appear to arise from multiple subbands (which may be spin-split), extracting values based on changes in oscillation amplitude is impractical; oscillating components from multiple subbands with different effective masses and scattering rates may contribute to the total amplitude at any field. Instead, the data is fit to Eq. (1.3).

The following sections will explore the fitting of Shubnikov-de Haas oscillations to Eq. (1.3), or variations thereof, adapted for oscillations arising from varying numbers of subbands. The parameters in the equation are adjusted to reproduce the qualitative features and amplitudes of experimentally measured $\Delta R_{xx}$ at 0.45-3 K (see Fig. 5.12). Specifically a two-subband model (with first and second harmonic terms), a two-spin-split subband model, and four-subband model will be evaluated against the experimental data. The FFT spectra of the calculated $\Delta R_{xx}$ are also compared to that obtained from the experimental data (see inset of Fig. 5.11a).

### 5.6.1 Two-subband, Two-harmonic Model

The experimental data was fit to two-subband model with first and second harmonic terms, similar to Eq. (1.3):

$$\frac{\Delta R_{xx}}{R_0} = \sum_{i=1}^{m} \sum_{s=1}^{2} 2A_i \exp\left(-\frac{2s\pi^2 k_B T_{D,i}}{\hbar\omega_c}\right) \frac{sX}{\sinh(sX)} \cos\left(\frac{2\pi s f_i}{B} + s\pi\right) \tag{5.1}$$

where $i$ is the subband index, $m$ is the number of occupied subbands ($m = 2$ in this case), $s$ is the order of the harmonic, $A_i$ are amplitude factors associated with intrasubband scattering probabilities, $k_B$ is the Boltzmann constant, $T_{D,i}$ is the Dingle temperature of each subband, $\hbar$ is the reduced Planck's constant, $\omega_c$ is the cyclotron frequency, $f_i$ are the oscillation

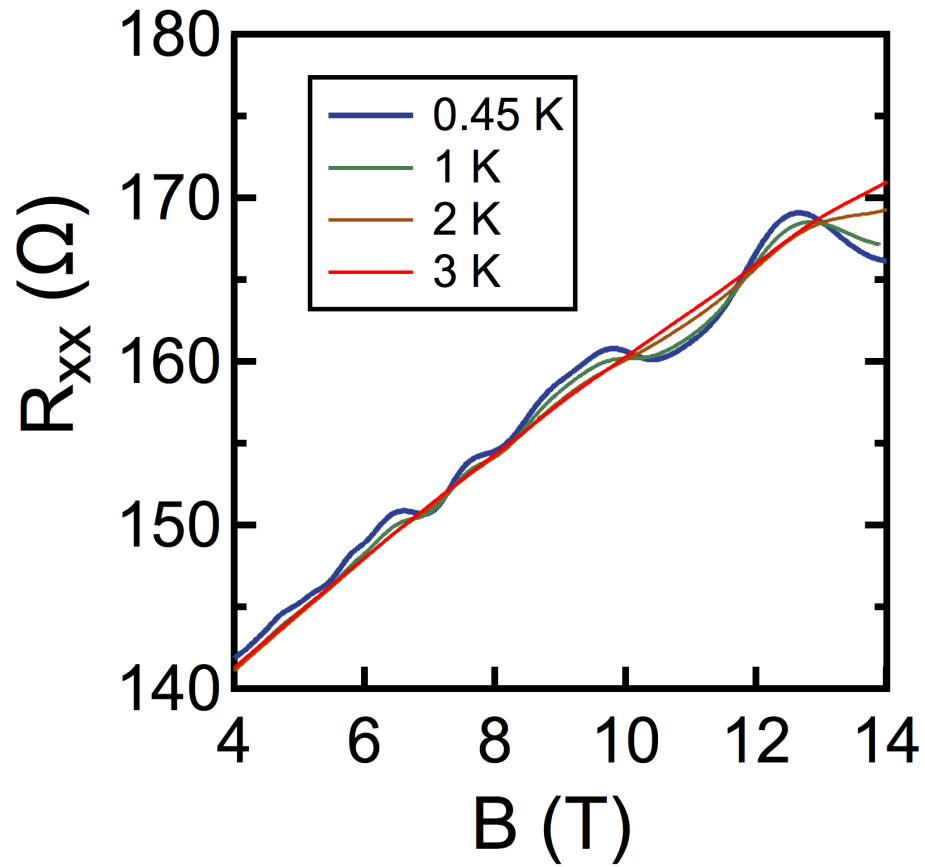**Figure 5.12:** Shubnikov-de Haas oscillations, $\Delta R_{xx}(1/B)$, extracted from the longitudinal magnetoresistance measured in sample MB (see Figs. 5.8 and 5.9) at temperatures between 0.45 K and 3 K. Adapted with permission from [131]. Copyright 2013, AIP Publishing LLC.
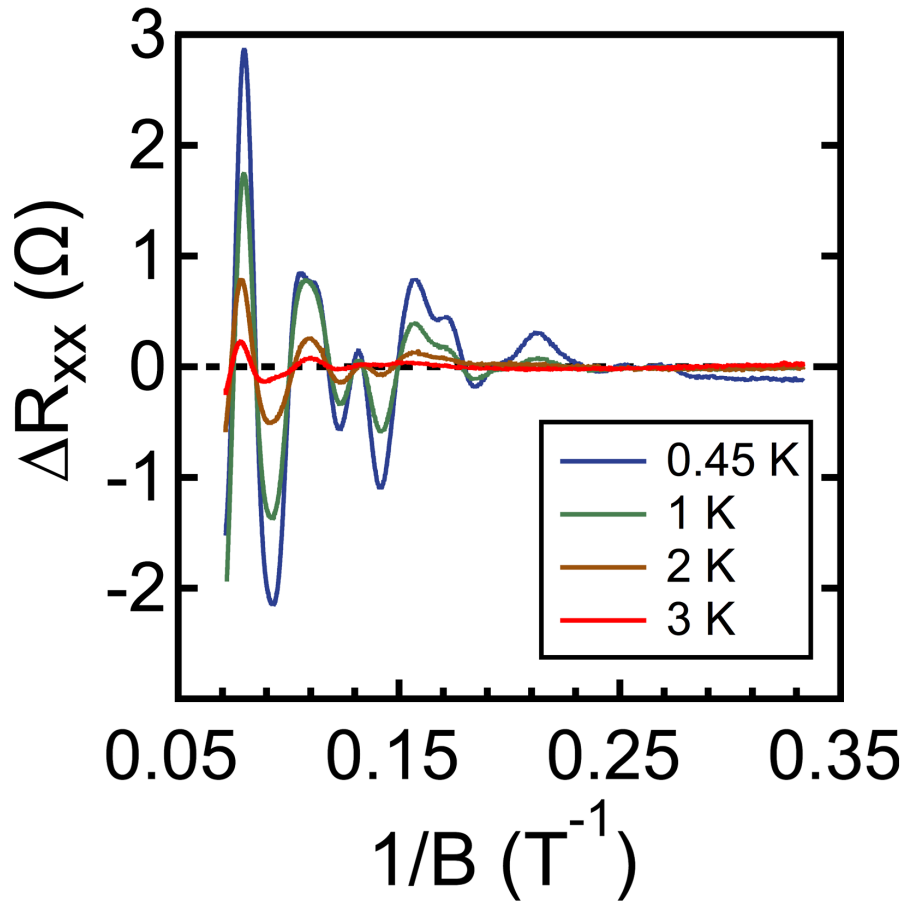
frequencies (in $1/B$), and $X = \left(2\pi^2 k_B T\right)\big/\left(\hbar\omega_c\right)$. The parameters extracted from this model are

presented in Table 5.2. The calculated $\Delta R_{xx}(1/B)$ and its corresponding FFT spectrum are

presented in Figs. 5.13a and 5.13b, respectively.

The values extracted for charge carrier mass are consistent with what is expected for

$d_{xy}$-derived subbands in SrTiO$_3$ [137-140]. The combined sheet carrier densities of the two

subbands do not account for the carrier density extracted from room-temperature Hall

measurements ($n_{s,H} = 4.46 \times 10^{13}$ cm$^{-2}$), but this can be reasonably attributed to parallel

conduction of the remaining low-mobility carriers in the La:STZO layer. The $\Delta R_{xx}(1/B)$

calculated with these parameters also qualitatively matches that of the experiment to a

reasonable extent, although discrepancies remain, especially at low $B$ fields. However, the

FFT spectrum of the calculated $\Delta R_{xx}(1/B)$ contains only 2 discernible peaks, which is

markedly simpler than the experimentally determined FFT. As such, the two-subband model

with first and second harmonics does not adequately describe the observed data.


*5.6.2 Two Spin-split Subband Model*

A two spin-split subband model was also explored by fitting to the equation:

$$\frac{\Delta R_{xx}}{R_0} = \sum_{i=1}^{m}\sum_{s=1}^{2} 2A_i \exp\left(-\frac{2s\pi^2 k_B T_{D,i}}{\hbar\omega_c}\right)\frac{sX}{\sinh(sX)}\cos\left(\frac{2\pi s f_i}{B} + s\pi\right)Z_s \qquad (5.2)$$

which is similar to Eq. (1.3) with the exception of the added Zeeman term,

$Z_s = \cos(s\dfrac{\pi}{4}\dfrac{m^*}{m_e}g^*)$, where $m^*$ is the effective mass, m$_e$ is the electron rest mass, and $g^*$ is

the Landé g factor. The above equation is only valid when the magnetic field **B** is oriented

parallel to the sample surface normal, which is consistent with the experiment described

here. The parameters extracted from fitting are presented in Table 5.3. The calculated
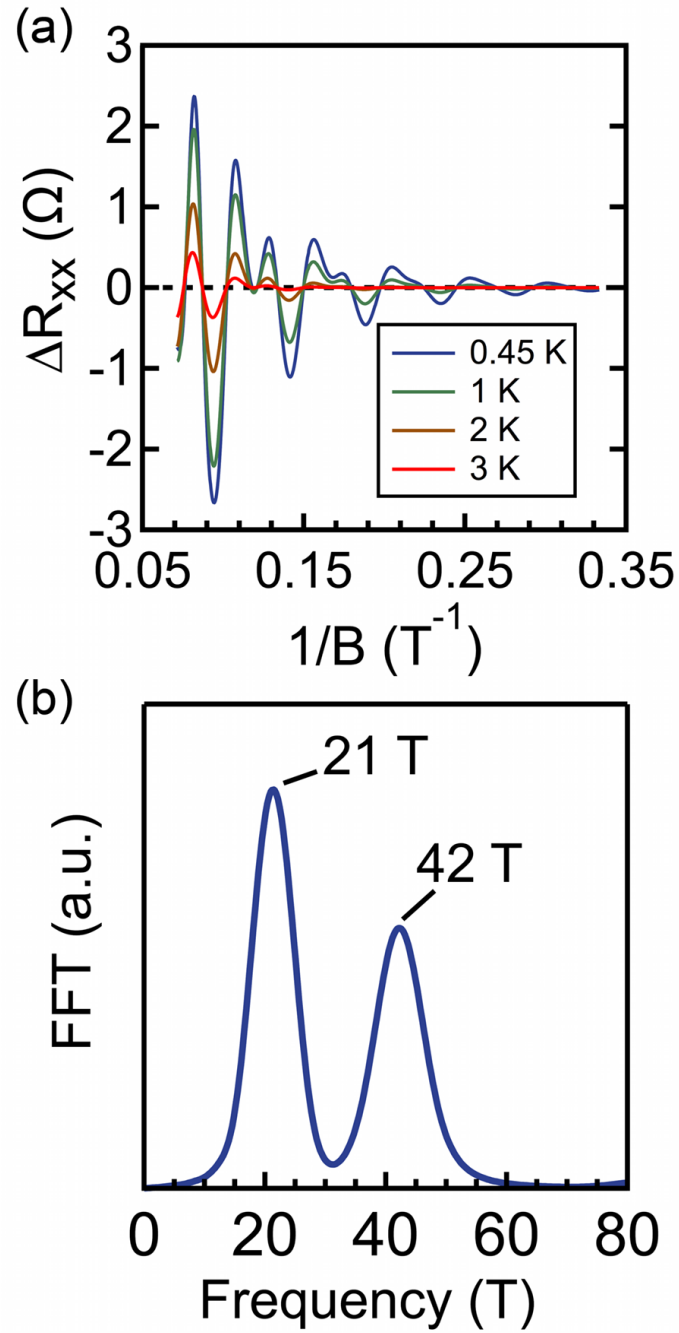
118

**Figure 5.13:** (a) Shubnikov-de Haas oscillations, $\Delta R_{xx}(1/B)$, calculated using Eq. (5.1), $m = 2$, with the parameters listed in Table 5.2, and (b) the corresponding Fourier transform of the data, with peak positions labeled.

**Table 5.2:** Parameters extracted from fits of the experimental Shubnikov-de Haas oscillations measured at 0.45 K to a two-subband model including first and second harmonic terms [Eq. (5.1), $m = 2$]. The sheet carrier densities ($n_s$), quantum scattering times ($\tau_q$), and quantum mobilities ($\mu_q$) extracted from the fits are shown for each subband. The effective mass $m^*$ is determined from the cyclotron frequency $\omega_c = eB/m^*$, $\tau_q$ is calculated from $\tau_q = \hbar/(2\pi k_B T_D)$, and $n_s$ is calculated from $f = nh/2q$, where $h$ is Planck's constant.

| Subband index $i$ | $R_0 A$ ($\Omega$) | $f$ (T) | $m^*$ ($m_e$) | $T_D$ (K) | $n_s$ (cm$^{-2}$) | $\tau_q$ (s) | $\mu_q$ (cm$^2$V$^{-1}$s$^{-1}$) |
|---|---|---|---|---|---|---|---|
| 1 | 2 | 21.4 | 1.02 | 0.8 | $1.03 \times 10^{12}$ | $1.52 \times 10^{-12}$ | 2620 |
| 2 | 10 | 42.2 | 1.08 | 1.5 | $2.04 \times 10^{12}$ | $8.10 \times 10^{-13}$ | 1320 |

$\Delta R_{xx}(1/B)$ and its corresponding FFT spectrum are presented in Figs. 5.14a and 5.14b, respectively.

Similar to the non-spin-split two-subband model, the resulting $\Delta R_{xx}(1/B)$ calculated $\Delta R_{xx}(1/B)$ using the parameters in Table III gives a reasonable qualitative agreement with the experimental data. The spin-split model gives a combined sheet carrier density far below that extracted from Hall measurements. Unlike the previous model, the FFT spectrum seems to qualitatively reproduce many of the features observed in the FFT of experimental data. As such, the spin-split model offers an improvement over the non-spin-split model; however, the extracted values for the charge carrier effective masses ($\sim 0.7 m_e$) are substantially lower than what is expected or previously observed for electrons in $d_{xy}$-derived subbands in SrTiO$_3$. The two spin-split subband model is therefore mostly consistent with the data, although the extracted values for the effective mass may call its validity into question.
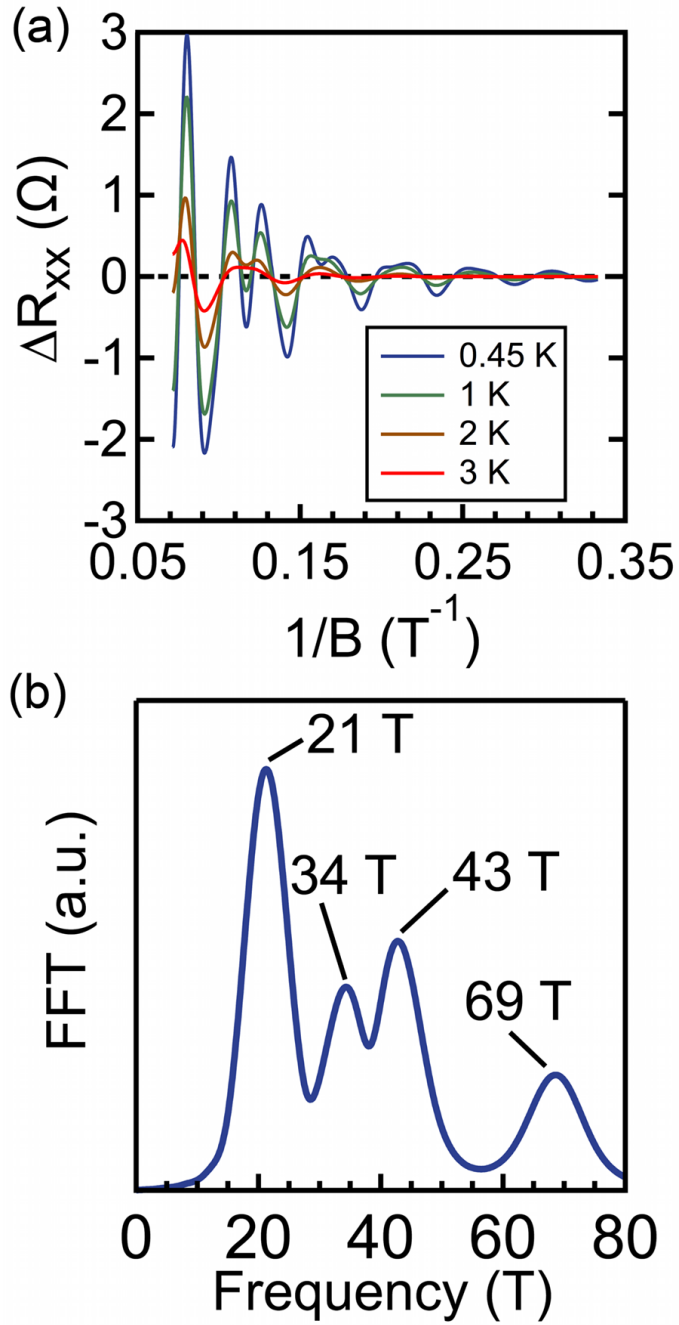
**Figure 5.14:** (a) Shubnikov-de Haas oscillations, $\Delta R_{xx}(1/B)$, calculated using Eq. (5.2), $m = 2$, with the parameters listed in Table 5.3, and (b) the corresponding Fourier transform of the data, with peak positions labeled.

**Table 5.3:** Parameters extracted from fits of the experimental Shubnikov-de Haas oscillations measured at 0.45 K to a two-spin-split-subband model [Eq. (5.2), $m = 2$]. The sheet carrier densities ($n_s$), quantum scattering times ($\tau_q$), and quantum mobilities ($\mu_q$) extracted from the fits are shown for each subband. The effective mass $m*$ is determined from the cyclotron frequency $\omega_c = eB/m^*$, $\tau_q$ is calculated from $\tau_q = \hbar/(2\pi k_B T_D)$, and $n_s$ is calculated from $f = nh/q$, where $h$ is Planck's constant.

| Subband index $i$ | $R_0 A$ ($\Omega$) | $f$ (T) | $m*$ ($m_e$) | $T_D$ (K) | $g*$ | $n_s$ (cm$^{-2}$) | $\tau_q$ (s) | $\mu_q$ (cm$^2$V$^{-1}$s$^{-1}$) |
|---|---|---|---|---|---|---|---|---|
| 1 | 7 | 21.3 | 0.67 | 1.1 | 2.65 | $5.14 \times 10^{11}$ | $1.10 \times 10^{-12}$ | 2880 |
| 2 | 5 | 34.3 | 0.73 | 1.35 | 2.6 | $8.28 \times 10^{11}$ | $9.00 \times 10^{-13}$ | 2170 |

*5.6.3 Four-subband Model*

The four subband model was evaluated by fitting with Eq. (1.3) for $m = 4$. Only the first harmonic term for each subband was considered in this analysis. The parameters extracted from this model are presented in Table IV. The calculated $\Delta R_{xx}(1/B)$ and its corresponding FFT spectrum are presented in Figs. 5.15a and 5.15b, respectively.

The $\Delta R_{xx}(1/B)$ calculated from the four-subband model arguably captures more of the qualitative features of the experimental data than the previously described models, especially at higher temperatures. Unlike the two spin-split subband model, the charge carrier effective masses extracted from the four-subband model are more consistent with theory and previous experiments. Variations in the mass ($0.95 m_e$ to $1.5\ m_e$) are expected for varying degrees of hybridization of $d_{xy}$ orbitals with $d_{xz}$ and $d_{yz}$ orbitals, which have a comparatively higher in-plane effective mass [138]. That being said, the FFT spectrum from the four-subband model does not capture as many of the features of the experimental data as that extracted from the two spin-split subband model.
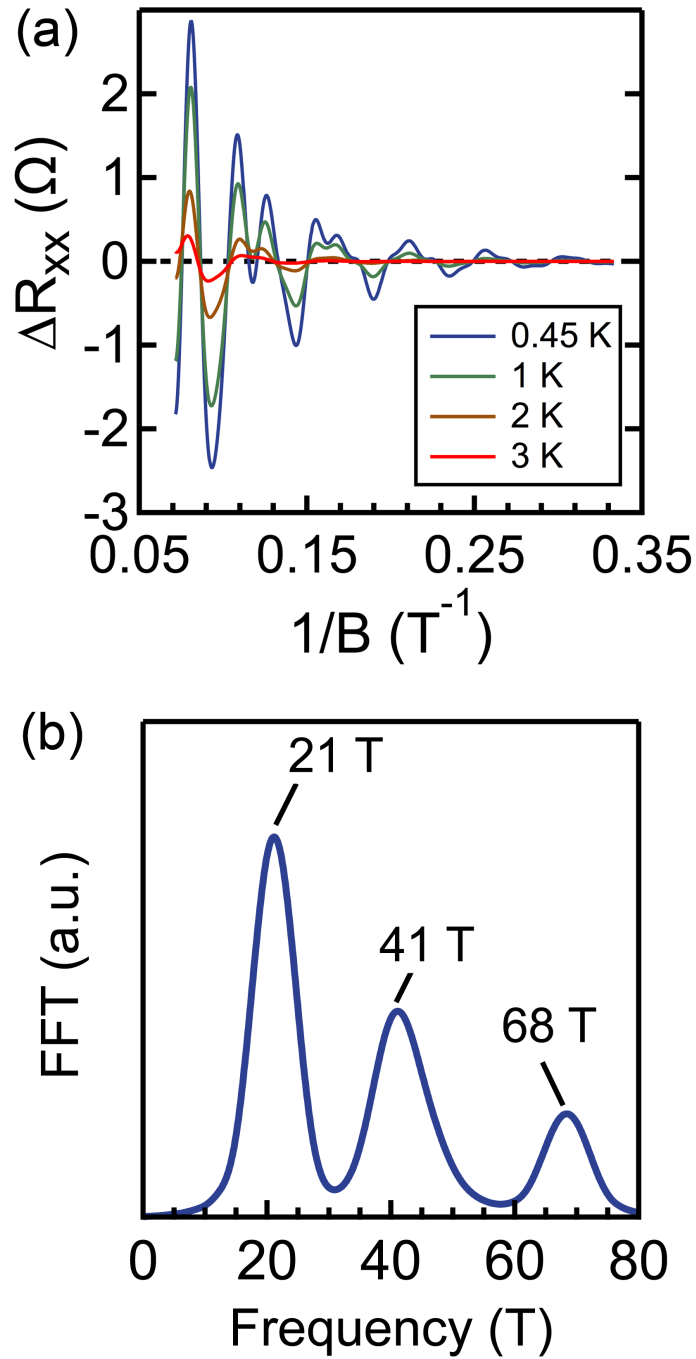
**Figure 5.15:** (a) Shubnikov-de Haas oscillations, $\Delta R_{xx}(1/B)$, calculated using Eq. (1.1), $m = 4$, with the parameters listed in Table 5.4. Adapted with permission from [131]. Copyright 2013, AIP Publishing LLC. (b) The corresponding Fourier transform of the data, with peak positions labeled.

**Table 5.4:** Parameters extracted from fits of the experimental Shubnikov-de Haas oscillations measured at 0.45 K to a four-subband model [Eq. (1.3), $m = 4$]. The sheet carrier densities ($n_s$), quantum scattering times ($\tau_q$), and quantum mobilities ($\mu_q$) extracted from the fits are shown for each subband. The effective mass $m^*$ is determined from the cyclotron frequency $\omega_c = eB/m^*$, $\tau_q$ is calculated from $\tau_q = \hbar/(2\pi k_B T_D)$ and $n_s$ is calculated from $f = nh/2q$, where $h$ is Planck's constant. Adapted with permission from [131]. Copyright 2013, AIP Publishing LLC.

| Subband index $i$ | $R_0A$ ($\Omega$) | $f$ (T) | $m^*$ ($m_0$) | $T_D$ (K) | $n_s$ (cm$^{-2}$) | $\tau_q$ (s) | $\mu_q$ (cm$^2$V$^{-1}$s$^{-1}$) |
|---|---|---|---|---|---|---|---|
| 1 | 2 | 21.2 | 0.95 | 0.9 | $1.02 \times 10^{12}$ | $1.35 \times 10^{-12}$ | 2496 |
| 2 | 2 | 41.2 | 1.4 | 0.8 | $1.99 \times 10^{12}$ | $1.52 \times 10^{-12}$ | 1907 |
| 3 | 6.5 | 43 | 1.5 | 1.1 | $2.08 \times 10^{12}$ | $1.10 \times 10^{-12}$ | 1288 |
| 4 | 0.8 | 68.4 | 1.2 | 0.8 | $3.30 \times 10^{12}$ | $1.52 \times 10^{-12}$ | 2225 |

*5.6.4 Further Comments*

Among the multiple subband models discussed above, the non-spin-split two-subband model appears to be the least consistent with the experimental data, in regards to both $\Delta R_{xx}(1/B)$ and the corresponding FFT. The two spin-split subband model and four-subband model are both more consistent with the data, though conclusively favoring one over the other as the best description of the electronic structure is difficult with the available data. Indeed, determining whether electronic subbands in SrTiO$_3$ 2DEGs experience spin splitting has proven difficult in previous studies [141]. That being said, the four-subband model arguably offers a better qualitative fit in $\Delta R_{xx}(1/B)$, and the extracted values for the electron effective mass are closer to what is expected for 2DEG's in SrTiO$_3$. As such, the four-subband model is currently the best description of the electronic structure of the modulation-doped SrTiO$_3$/La:STZO system explored here.

The remaining discrepancies between the calculated and experimental $\Delta R_{xx}(1/B)$ after fitting can be attributed to intersubband scattering [46, 142], whose contribution is not included in any of the models above. This effect is more significant at low $B$ [46, 142] and when different subbands are close in energy. The energy spacing between subbands $\Delta E$ can be described by:

$$\Delta E = \frac{q\hbar\Delta f}{m^*} \tag{3}$$

where $\Delta f$ is the difference in the frequencies of Shubnikov-de Haas oscillations arising from any two subbands, and q the elementary charge. For the four-subband model, this gives $\Delta E$ ranging from 0.15 meV to 5 meV. These relatively small values of $\Delta E$ may explain the significant discrepancies between calculated and experimental data, which are more apparent at low $B$.

An improved theoretical understanding of electronic transport in $SrTiO_3$-based 2DEGs would significantly improve the prospects of conclusively characterizing the electronic structure of modulation-doped $SrTiO_3$. Improvements in electron mobility through materials development would also allow for the resolution of finer features in the magnetoresistance. Unfortunately, significant improvements in the mobility for this structure have proven elusive, exacerbated perhaps by interface scattering or ionized impurity scattering (despite its reduction through modulation doping). The following section will explore alternative structures for modulation doping of $SrTiO_3$ with STZO and $SrZrO_3$.

## 5.7 Superconductivity in SrTiO₃/La:STZO

Figure 5.16a shows the longitudinal resistance $R_{xx}$ measured versus temperature at a magnetic field $H = 0$ for sample MB (see Fig. 5.8) down to 50 mK, measured in a Physical

Properties Measurement System (Quantum Design, Inc.) equipped with a dilution refrigerator. The apparent onset of a superconducting transition versus temperature is observed at approximately 420 mK, followed by a shoulder in $R_{xx}$ at approximately 280 mK. $R_{xx}$ then falls below the detection limit of the PPMS resistivity option at temperatures below 150 mK. The appearance of the shoulder suggests multiple transitions or perhaps a disruption of the ~420 mK transition with decreasing temperature, though the behavior observed here is not yet well understood. Whatever mechanism may be active, the critical temperatures of the superconducting transitions in this system are consistent with the range of superconducting critical temperatures observed in bulk doped $SrTiO_3$ [13]. A shoulder in $R_{xx}$ is also observed versus magnetic field $H$ at various temperatures, as shown in Fig. 5.16b. As such, this shoulder is a feature that appears both in the temperature dependence and the field dependence of $R_{xx}$, suggesting two superconductivity-related transitions with separate critical temperatures and critical fields. Determining the origin of this behavior, as well as its tilt-angle dependence (to determine whether the superconductivity two-dimensional), is left for future studies.

*5.8 Alternative Modulation-doped Heterostructures*

In an effort to increase the mobility of modulation-doped heterostructures beyond those described in Fig. 5.8, alternative structures were also explored. One such alternative structure involved placing an undoped STZO spacer between the La:STZO and $SrTiO_3$ layers with the intent of increasing charge carrier mobility by further separating ionized impurities from the 2DEG in $SrTiO_3$, which has proven effective in analogous modulation-doped III-V heterostructures [39]. Figure 5.17 shows transport data collected from two
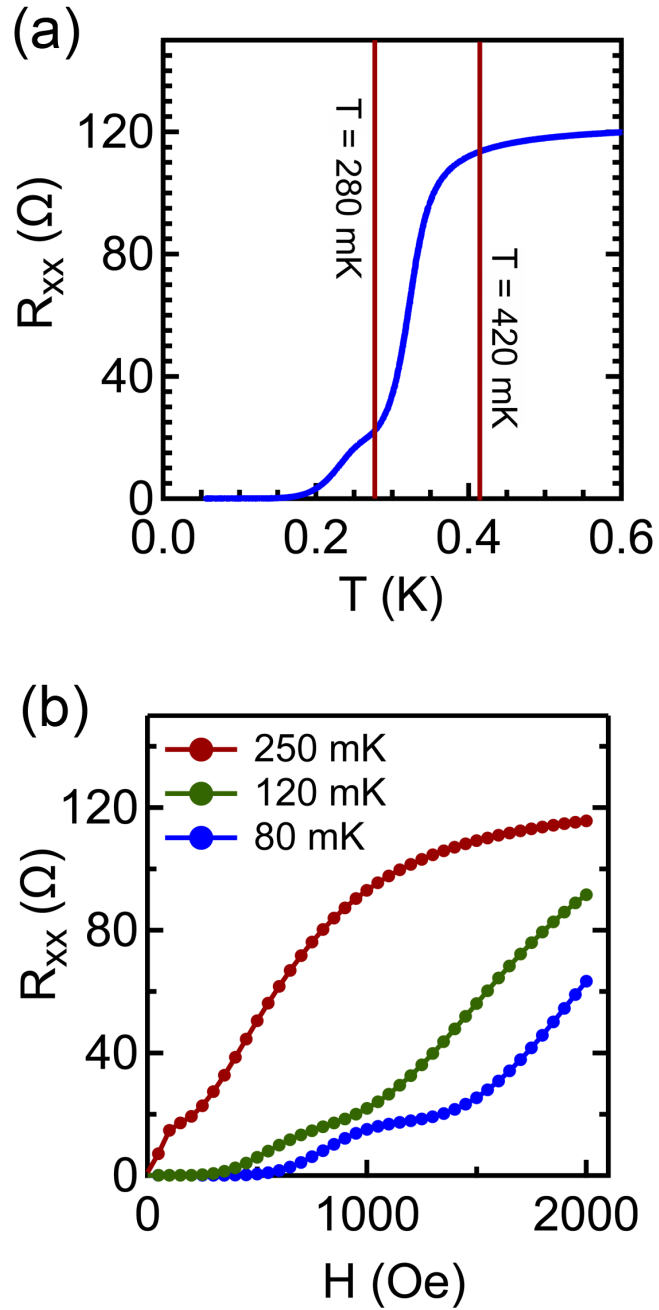
**Figure 5.16:** (a) Longitudinal resistance, $R_{xx}$, versus temperature at magnetic field $H$ = 0 measured for sample "MB" (see Fig. 5.8). The approximate temperatures for the onset of two superconducting transitions are marked. (b) $R_{xx}$ versus $H$ (with **H** oriented perpendicular to the plane of the interface) measured at various temperatures for the same sample.

samples which are identical to samples MA and MB, except in one sample, a 5 nm undoped STZO spacer was placed between La:STZO and $SrTiO_3$ layers. In both structures, the apparent carrier density decreases with decreasing temperature until ~40 K, below which the carrier density appears constant. This is likely due to the effect of multicarrier conduction on the zero-field Hall coefficient, as discussed for similar structures in previous sections. This indicates that some of the charge carriers in the system reside in the $SrTiO_3$ layer of both samples. Surprisingly, adding the spacer layer results in a decrease in electron mobility at 2 K of almost an order of magnitude compared to the sample without a spacer layer. This is greater than the change in mobility expected from differences in carrier density between the two samples, so it is likely a change effected by the added spacer layer. The reason for this decreased mobility is unclear, though it is most likely associated with a significant fraction of the carriers residing in the spacer layer, resulting in a lower overall mobility. Whatever the case may be, adding an undoped spacer layer does not appear to be an effective method for increasing mobility in modulation-doped $SrTiO_3$/STZO heterostructures.

Due in part to the difficulty of controllably doping STZO layers, selectively-delta-doped heterostructures like those shown schematically in Fig. 5.18 (modeled after analogous structures in III-V semiconductors [6]) were also investigated. The transport data obtained at 2 K for each sample is shown in Table V. Such structures appear to give an advantage in electron mobility over standard selectively-doped heterostructures (see Fig. 5.8). However, no oscillations in the magnetoresistance were observed for temperatures down to 0.45 K and for fields up to 14 T. Again, scattering from the undoped STZO may be playing a substantial role in the transport, thus explaining the absence of oscillatory behavior in the longitudinal magnetoresistance. Ultimately, these structures do not allow for as extensive study of the

128
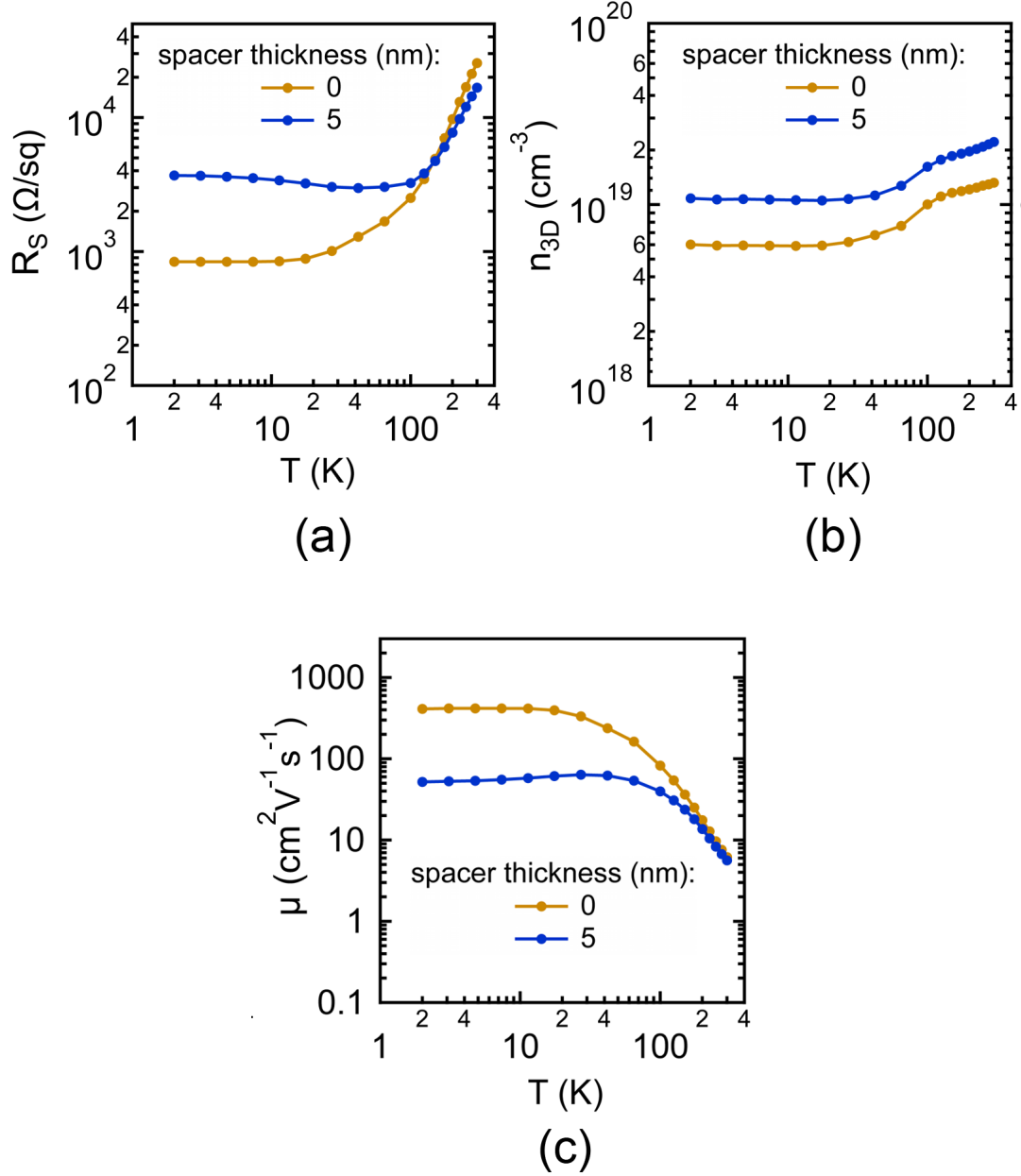
**Figure 5.17:** (a) Sheet resistance, $R_S$, (b) 3D charge carrier Hall density, $n_{3D} = 1/(eR_H t_{STZO})$, where $t_{STZO}$ is the La:STZO layer thickness, and (c) Hall mobility, $\mu$, determined as a function of temperature for nominally modulation doped heterostructures with structures similar to that schematically described in Fig. 5.8, except one contains a 5 nm undoped STZO spacer between $SrTiO_3$ and La:STZO layers. STZO layers in both samples were grown with ZTB/B (BEP) = 0.13 and $B/A$ (BEP) = 52.8. Both La:STZO layers have a nominal dopant density of $\sim 2 \times 10^{19}$ $cm^{-3}$.
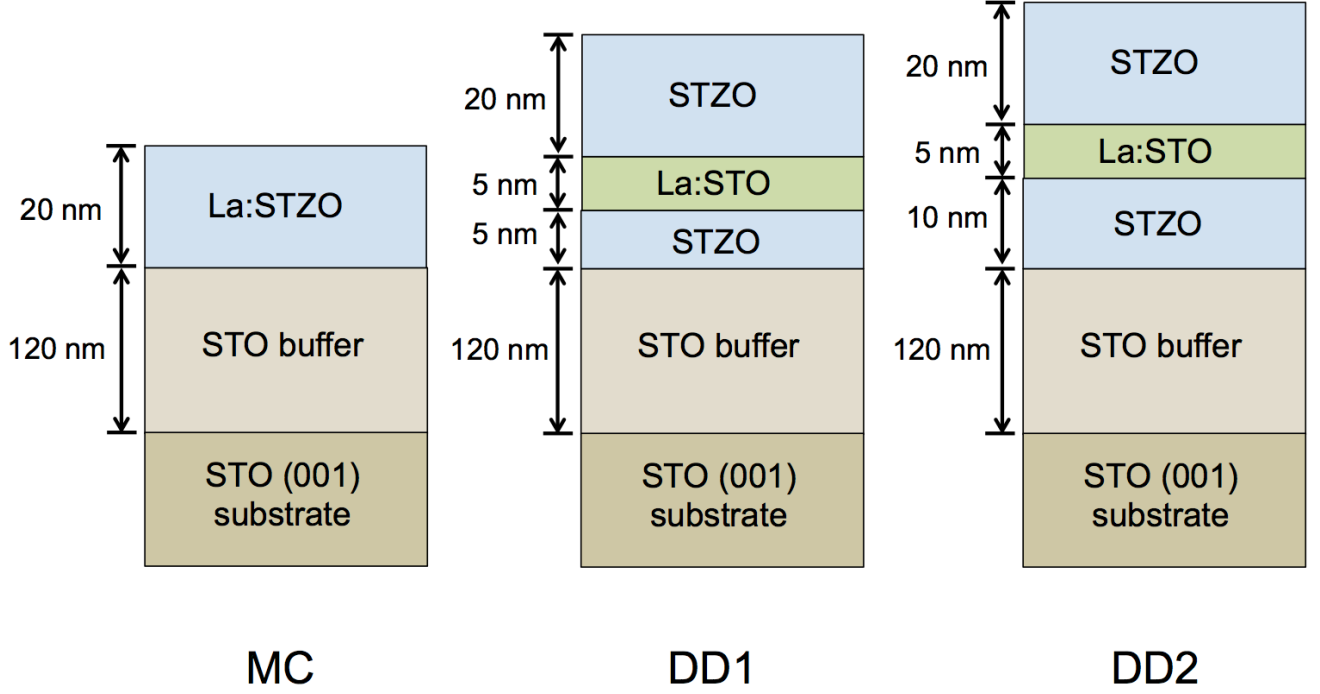
**Figure 5.18:** Schematic of selectively-delta-doped heterostructures (DD1 and DD2) grown by hybrid MBE, with a standard selectively-doped heterostructure (MC) shown for comparison. Each doped layer contains a nominal dopant concentration of $2 \times 10^{20}$ cm$^{-3}$. ZTB/B (BEP) = 0.12 for STZO layers shown here. The transport properties of these structures at 2 K are presented in Table V.

**Table 5.5:** Sheet resistance ($R_S$), zero-field Hall coefficient ($R_H$), sheet carrier Hall density ($n_{2D}$), and Hall mobility ($\mu_H$) at $T = 2$ K for samples described schematically in Fig. 5.18.

| Sample | $R_S$ ($\Omega$/sq) | $R_H$ ($\times 10^4$ cm$^2$C$^{-1}$) | $n_{2D}$ (1/(e$R_H$), cm$^{-2}$) | $\mu_H$ (cm$^2$V$^{-1}$s$^{-1}$) |
|--------|---------|---------|---------|---------|
| MC | 510 | 26 | $2.1 \times 10^{13}$ | 510 |
| DD1 | 95 | 20 | $3.1 \times 10^{13}$ | 2100 |
| DD2 | 55 | 9.3 | $6.7 \times 10^{13}$ | 1700 |

electronic structure as those showing Shubnikov-de Haas oscillations.

In the interest of reducing alloy scattering from STZO, the feasibility of integrating SrZrO$_3$ into modulation-doped heterostructures was also investigated. Structures were grown with the following configuration: SrTiO$_3$ (001) substrate/ 5 nm or 10 nm SrZrO$_3$/ 650 nm La:STO ($n_{La}$ = 5 × 10$^{18}$ cm$^{-3}$). The growths of SrZrO$_3$ and La:SrTiO$_3$ layers were consistent with stoichiometric growth conditions discussed in section 5.4 and Chapter 3, respectively. All resulting structures were insulating. Therefore, integration of SrZrO$_3$ into heterostructures as a separator layer between La:STO and undoped SrTiO$_3$ might only be feasible for transport studies with thinner SrZrO$_3$ layers or for growth on substrates with smaller lattice mismatch. Since controlled electron doping of SrTiO$_3$ layers with La appears to be compromised when growing on SrZrO$_3$, further efforts in this area were suspended.


*5.9 Chapter Summary*

The growth of STZO using both TTIP and ZTB metal-organic precursors along with a Sr solid source was discussed. Expansion of the lattice parameter could not be used as a measure of non-stoichiometry as was the case for the growth of SrTiO$_3$ and Ba$_x$Sr$_{1-x}$TiO$_3$, since stoichiometric conditions do not correspond to a minimum lattice parameter. RHEED and XRD analysis show a clear transition in growth conditions from A-cation excess to nominal cation stoichiometry, but the transition from stoichiometry to B-cation excess is much less apparent. This latter boundary could only be discerned with RBS data. The decreasing lattice parameter with increasing *B/A* (BEP) was then attributed to preferential segregation of Zr into ZrO$_x$ amorphous phases, rather than strain relaxation.

The electron doping of STZO films was then discussed. STZO films could not be doped for ZTB/B (BEP) greater than 0.13 (corresponding to ~5% Zr substitution) Thick La:STZO films separated from a $SrTiO_3$ substrate by an undoped buffer layer show electron mobilities below 20 $cm^2V^{-1}s^{-1}$ (for ZTB/B (BEP) = 0.07) and ~1 $cm^2V^{-1}s^{-1}$ (for ZTB/B (BEP) = 0.13) for $n_{3D}$ ~1 × $10^{20}$ $cm^{-3}$ at 2 K. Lower doping concentrations could not be achieved in this structure; films grown with a lower dopant density (or grown in off-stoichiometric conditions) were insulating. Interfacing La:STZO directly with $SrTiO_3$ allows for electron doping with La down to ~2 × $10^{19}$ $cm^{-3}$ and electron mobilities greater than 300 $cm^2V^{-1}s^{-1}$. The increase in the Hall coefficient (decrease in apparent carrier density) with decreasing temperature is indicative of multicarrier Hall conduction and thus suggests charge transfer into the $SrTiO_3$ layer.

The successful generation of a 2DEG in $SrTiO_3$ is then confirmed with Shubnikov-de Haas analysis of the sample labeled "MB" (see Figs. 5.8 and 5.9). The increased mobility of charge carriers suggests charge transfer into the undoped $SrTiO_3$ buffer layer, and the angle dependence of the Shubnikov-de Haas oscillations confirms the two-dimensional nature of the system. Multiple oscillation frequencies (arising from the occupation of multiple subbands) are observed in the longitudinal magnetoresistance. The magnetoresistance data is fit to several models for Shubnikov-de Haas oscillations from multiple subbands. The model for two spin-split subbands and the model for four (non-spin-split) subbands are the most consistent with the experimental data. The four-subband model appears to be more qualitatively consistent with the experiment, though more studies are needed to conclusively determine whether spin-splitting is involved.

Alternative modulation-doped heterostructures were investigated for the purpose of improving the electron mobility. Incorporating a 5 nm-thick undoped STZO spacer layer was shown to actually decrease the mobility at low temperatures, possibly due to scattering from the undoped layer. Selectively delta-doped heterostructures were shown to give electron mobilities up to 2000 $cm^2V^{-1}s^{-1}$. However, not much could be determined about their electronic structure due to the absence of magnetoresistance oscillations at temperatures down to 0.45 K and magnetic fields up to 14 T.

# Chapter 6

## Summary and Future Outlook

Chapters 3 and 4 demonstrated the effectiveness of using RHEED in conjunction with XRD to achieve ideal A:B cation stoichiometry in both $SrTiO_3$ and $Ba_xSr_{1-x}TiO_3$ thin films grown by hybrid MBE. In particular, observed trends in the surface reconstruction with changing B/A cation ratio can be used to indirectly determine the surface and resulting bulk stoichiometry of thin films for applications and research efforts where defects from non-stoichiometry affect the most relevant materials properties, such as electron mobility in $SrTiO_3$ conducting channels or dielectric loss in $Ba_xSr_{1-x}TiO_3$ capacitor structures. This was shown to apply to the growth of STZO as a doped barrier layer for modulation doping, to the extent that the onset of A-cation-rich growth conditions could be readily discerned. The transition to B-cation-rich growth in STZO was not so apparent in RHEED and XRD, and could only be discerned with measurements of the chemical composition (e.g. RBS). This latter issue suggests that substantially different growth dynamics are active in the hybrid MBE growth of complex oxide solid solutions using multiple metal-organic precursors rather than multiple solid-sources, as was the case for the growth of $Ba_xSr_{1-x}TiO_3$. Additional studies utilizing electron microscopy coupled with energy-dispersive X-ray spectroscopy (EDX) chemical analysis may yield important information about the incorporation of multiple volatile metal-organic precursors into a complex oxide thin film.

In Chapter 5, it was also shown that STZO could be doped and used to transfer charge carriers into $SrTiO_3$, thus forming a 2DEG. As such, it was shown to be effective in realizing a modulation-doped heterostructure. The mobility of electrons in the 2DEG appears to be limited in part by the lower limit of doping in the La:STZO layer. Interfacial scattering may also be a limiting factor for mobility, though the exact nature of its contribution remains unclear. The difficulty in determining stoichiometric growth conditions

for STZO, as well as the inability to electron dope films with more than ~5% Zr substitution, limits the prospects of STZO for band gap engineering in complex oxides similarly to efforts in III-V semiconductors. Although investigations into modulation doped heterostructures with STZO does support the assertion that modulation doping in complex oxides is possible, there are substantial limitations to the engineering of heterostructures for substantially improved mobility over uniformly-doped $SrTiO_3$.

The observation of superconductivity in the modulation-doped heterostructure described in Chapter 5 warrants further investigation into the nature of the superconducting transition, focusing particularly on features that suggest a second transition with a separate critical temperature and critical magnetic field within the same system. Investigation of the tilt-angle dependence of the critical field may yield information about the dimensionality of the superconducting transition. This may also determine whether the 2DEG, the La:STZO layer, or both are undergoing a superconducting transition in this system.

It is reasonable to look to other material systems as potential candidates as a doped barrier layer. Among other perovskite band insulators, $KTaO_3$ and $CaSnO_3$ are predicted to have conduction band offsets of 150 and 130 meV, respectively, with $SrTiO_3$ [143]. $KTaO_3$ has been successfully doped n-type with Ba [144] and oxygen vacancies [145] in previous studies with high electron mobilities in bulk single crystals ($\sim$20,000 $cm^2V^{-1}s^{-1}$) at 4.2 K [145]. However, it is not a favorable candidate for the modulation doping of $SrTiO_3$ due to its polar nature; along the [001] direction it is composed of alternating $KO^-$ and $TaO_2^+$ layers, which would to a polar discontinuity at the interface with $SrTiO_3$. $CaSnO_3$, on the other hand, is isovalent with $SrTiO_3$. Similar to $SrZrO_3$, $CaSnO_3$ is orthorhombic (space group Pbnm [146]), but compared to $SrZrO_3$, it has a much smaller lattice mismatch with

136

SrTiO$_3$ (pseudocubic $a \sim 3.96$ Å [146]). It remains to be seen whether shallow donors exist for this compound. If not, other perovskite systems will need to be explored.

Regardless of the material system employed for modulation doping, further investigation is needed to more accurately describe the electronic structure of low-density 2DEGs through Shubnikov-de Haas analysis, particularly in regard to whether or not the subbands are spin-split. In the realm of theory, simulations of Shubnikov-de Haas oscillations in systems with multiple occupied subbands both with and without spin-splitting would aid experimental efforts in investigating the electronic structure. This may also involve determining how subbands closely-spaced in energy interact with each other through intersubband scattering. Experimentally, further investigations of the subband structure depend not only on achieving higher electron mobility but on the ability to control the 2DEG carrier density, thus adjusting the filling of subbands. Although this may be accomplished with controlled doping, further development of electric-field gated structures for this purpose based on hybrid MBE-grown SrTiO$_3$ will remain a necessary endeavor for studying the electronic structure of 2DEGs in SrTiO$_3$.

# References

[1]     E. Abrahams, S. V. Kravchenko, and M. P. Sarachik, "Colloquium: Metallic behavior and related phenomena in two dimensions," *Rev. Mod. Phys.* 73, 251-266 (2001).

[2]     F. Schaffler, "High-mobility Si and Ge structures," *Semicond. Sci. Technol.* 12, 1515-1549 (1997).

[3]     A. Cho, "Growth of III–V semiconductors by molecular beam epitaxy and their properties," *Thin Solid Films* 100, 291--317 (1983).

[4]     D. C. Look, *Electrical Characterization of GaAs Materials and Devices*: Wiley, (1989).

[5]     L. Pfeiffer and K. W. West, "The role of MBE in recent quantum Hall effect physics discoveries," *Physica E* 20, 57-64 (2003).

[6]     E. F. Schubert, "Delta Doping of III-V Compound Semiconductors - Fundamentals and Device Applications," *J. Vac. Sci. Technol. A-Vac. Surf. Films* 8, 2980-2996 (1990).

[7]     P. Ye, Y. Xuan, Y. Wu, M. Xu, and S. Oktyabrsky, *Fundamentals of III-V Semiconductor MOSFETs*: Springer, (2010).

[8]     O. Ambacher, J. Smart, J. R. Shealy, N. G. Weimann, K. Chu, M. Murphy*, et al.*, "Two-dimensional electron gases induced by spontaneous and piezoelectric polarization charges in N- and Ga-face AlGaN/GaN heterostructures," *J Appl Phys* 85, 3222-3233 (1999).

[9]     R. S. Pengelly, S. M. Wood, J. W. Milligan, S. T. Sheppard, and W. L. Pribble, "A Review of GaN on SiC High Electron-Mobility Power Transistors and MMICs," *IEEE Trans. Microw. Theory Tech.* 60, 1764-1783 (2012).

[10]    T. Wojtowicz, M. Kutrowski, G. Karczewski, J. Kossut, B. Konig, A. Keller*, et al.*, "II-VI quantum structures with tunable electron g-factor," *J. Cryst. Growth* 214, 378-386 (2000).

[11]    K. von Klitzing, "The Quantized Hall-Effect," *Rev. Mod. Phys.* 58, 519-531 (1986).

[12]     D. C. Tsui, H. L. Stormer, and A. C. Gossard, "Two-dimensional Magnetotransport in the Extreme Quantum Limit," *Phys. Rev. Lett.* 48, 1559-1562 (1982).

[13]     J. Appel, "Soft-mode Superconductivity in $SrTiO_{3-x}$," *Phys. Rev.* 180, 508-& (1969).

[14]     G. H. Jonker and J. H. Vansanten, "Ferromagnetic Compounds of Manganese with Perovskite Structure," *Physica* 16, 337-349 (1950).

[15]     A. K. Tagantsev, V. O. Sherman, K. F. Astafiev, J. Venkatesh, and N. Setter, "Ferroelectric materials for microwave tunable applications," *J. Electroceram.* 11, 5-66 (2003).

[16]     M. Imada, A. Fujimori, and Y. Tokura, "Metal-insulator transitions," *Rev. Mod. Phys.* 70, 1039-1263 (1998).

[17]     H. P. R. Frederikse, W. R. Hosler, and W. R. Thurber, "Magnetoresistance of Semiconducting $SrTiO_3$," *Phys. Rev.* 143, 648-651 (1966).

[18]     O. N. Tufte and P. W. Chapman, "Electron Mobility in Semiconducting Strontium Titanate," *Phys. Rev.* 155, 796-802 (1967).

[19]     T. V. Ramakrishnan, "Strongly correlated electrons in solids," *Curr. Sci.* 95, 1284-1309 (2008).

[20]     A. Ohtomo and H. Y. Hwang, "A high-mobility electron gas at the $LaAlO_3/SrTiO_3$ heterointerface.," *Nature* 427, 423-6 (2004).

[21]     H. Ishida and A. Liebsch, "Origin of metallicity of $LaTiO_3/SrTiO_3$ heterostructures," *Phys. Rev. B* 77, 5 (2008).

[22]     R. Ohtsuka, M. Matvejeff, K. Nishio, R. Takahashi, and M. Lippmaa, "Transport properties of $LaTiO_3/SrTiO_3$ heterostructures," *Appl. Phys. Lett.* 96, 3 (2010).

[23]     P. Moetakef, T. A. Cain, D. G. Ouellette, J. Y. Zhang, D. O. Klenov, A. Janotti, *et al.*, "Electrostatic carrier doping of $GdTiO_3/SrTiO_3$ interfaces," *Appl. Phys. Lett.* 99, 232116 (2011).

[24] C. A. Jackson, J. Y. Zhang, C. R. Freeze, and S. Stemmer, "Quantum critical behaviour in confined $SrTiO_3$ quantum wells embedded in antiferromagnetic $SmTiO_3$," *Nat. Commun.* 5, 6 (2014).

[25] P. Xu, D. Phelan, J. S. Jeong, K. A. Mkhoyan, and B. Jalan, "Stoichiometry-driven metal-to-insulator transition in $NdTiO_3$/$SrTiO_3$ heterostructures," *Appl. Phys. Lett.* 104, 5 (2014).

[26] J. A. Bert, B. Kalisky, C. Bell, M. Kim, Y. Hikita, H. Y. Hwang*, et al.*, "Direct imaging of the coexistence of ferromagnetism and superconductivity at the $LaAlO_3$/$SrTiO_3$ interface," *Nat. Phys.* 7, 767-771 (2011).

[27] M. Boucherit, O. F. Shoron, T. A. Cain, C. A. Jackson, S. Stemmer, and S. Rajan, "Extreme charge density $SrTiO_3$/$GdTiO_3$ heterostructure field effect transistors," *Appl. Phys. Lett.* 102, 4 (2013).

[28] A. D. Caviglia, S. Gariglio, N. Reyren, D. Jaccard, T. Schneider, M. Gabay*, et al.*, "Electric field control of the $LaAlO_3$/$SrTiO_3$ interface ground state," *Nature* 456, 624-627 (2008).

[29] A. Joshua, S. Pecker, J. Ruhman, E. Altman, and S. Ilani, "A universal critical density underlying the physics of electrons at the $LaAlO_3$/$SrTiO_3$ interface," *Nat. Commun.* 3, 7 (2012).

[30] K. Ploog, "Delta-Doping in MBE-Grown GaAs - Concept and Device Application," *J. Cryst. Growth* 81, 304-313 (1987).

[31] Y. Kozuka, M. Kim, C. Bell, B. G. Kim, Y. Hikita, and H. Y. Hwang, "Two-dimensional normal-state quantum oscillations in a superconducting heterostructure.," *Nature* 462, 487--90 (2009).

[32] H. Nakamura, H. Takagi, I. H. Inoue, Y. Takahashi, T. Hasegawa, and Y. Tokura, "Low temperature metallic state induced by electrostatic carrier doping of $SrTiO_3$," *Appl. Phys. Lett.* 89, 3 (2006).

[33] T. Sato, K. Shibuya, T. Ohnishi, K. Nishio, and M. Lippmaa, "Fabrication of $SrTiO_3$ field effect transistors with $SrTiO_{3-x}$ source and drain electrodes," *Jpn. J. Appl. Phys. Part 2 - Lett. Express Lett.* 46, L515-L518 (2007).

[34]   K. Ueno, I. H. Inoue, H. Akoh, M. Kawasaki, Y. Tokura, and H. Takagi, "Field-effect transistor on $SrTiO_3$ with sputtered $Al_2O_3$ gate insulator," *Appl. Phys. Lett.* 83, 1755-1757 (2003).

[35]   K. Ueno, S. Nakamura, H. Shimotani, A. Ohtomo, N. Kimura, T. Nojima, *et al.*, "Electric-field-induced superconductivity in an insulator," *Nat. Mater.* 7, 855-858 (2008).

[36]   R. Dingle, H. L. Stormer, A. C. Gossard, and W. Wiegmann, "Electron Mobilities in Modulation-doped Semiconductor Heterojunction Super-lattices," *Appl. Phys. Lett.* 33, 665-667 (1978).

[37]   V. Umansky, M. Heiblum, Y. Levinson, J. Smet, J. Nubler, and M. Dolev, "MBE growth of ultra-low disorder 2DEG with mobility exceeding $35 \times 10^6$ $cm^2/Vs$," *J. Cryst. Growth* 311, 1658-1661 (2009).

[38]   H. L. Stormer, R. Dingle, A. C. Gossard, W. Wiegmann, and M. D. Sturge, "Two-dimensional Electron-gas at Differentially Doped GaAs-$Al_xGa_{1-x}$As Heterojunction Interface," *J. Vac. Sci. Technol.* 16, 1517-1519 (1979).

[39]   H. L. Stormer, A. Pinczuk, A. C. Gossard, and W. Wiegmann, "Influence of an Undoped (AlGa)As Spacer on Mobility Enhancement in GaAs-(AlGa)As Super-lattices," *Appl. Phys. Lett.* 38, 691-693 (1981).

[40]   Y. S. Lee, J. S. Lee, T. W. Noh, D. Y. Byun, K. S. Yoo, K. Yamaura, *et al.*, "Systematic trends in the electronic structure parameters of the 4d transition-metal oxides SrMO3 (M=Zr, Mo, Ru, and Rh)," *Phys. Rev. B* 67, 4 (2003).

[41]   T. K. Y. Wong, B. J. Kennedy, C. J. Howard, B. A. Hunter, and T. Vogt, "Crystal structures and phase transitions in the $SrTiO_3$-$SrZrO_3$ solid solution," *J. Solid State Chem.* 156, 255-263 (2001).

[42]   R. Schafranek, J. D. Baniecki, M. Ishii, Y. Kotaka, K. Yamanka, and K. Kurihara, "Band offsets at the epitaxial $SrTiO_3/SrZrO_3$ (001) heterojunction," *J. Phys. D-Appl. Phys.* 45, 5 (2012).

[43]   R. E. A. McKnight, B. J. Kennedy, Q. Zhou, and M. A. Carpenter, "Elastic anomalies associated with transformation sequences in perovskites: II. The strontium zirconate-titanate Sr(Zr,Ti)$O_3$ solid solution series," *J. Phys.-Cond. Matt.* 21, 12 (2009).

[44]     T. Tsurumi, T. Teranishi, S. Wada, H. Kakemoto, M. Nakada, J. Akedo*, et al.*, "Wide Range Dielectric Spectroscopy of $SrTiO_3$-$SrZrO_3$ Solid Solution," in *2006 15th IEEE Int. Symp. Appl. Ferro.*, ed New York: Ieee, 2007, pp. 194-201.

[45]     J. H. Davies, *The Physics of Low-dimensional Semiconductors: An Introduction*: Cambridge University Press, (1998).

[46]     P. T. Coleridge, "Intersubband Scattering in a 2D Electron-gas," *Semicond. Sci. Technol.* 5, 961-966 (1990).

[47]     A. Isihara and L. Smrcka, "Density and Magnetic-Field Dependences of the Conductivity of Two-dimensional Electron-Systems," *J. Phys. C* 19, 6777-6789 (1986).

[48]     N. W. Ashcroft and N. D. Mermin, *Solid State Physics*: Harcourt College Publishers, (1976).

[49]     J. Y. Tsao, *Materials Fundamentals of Molecular Beam Epitaxy*: Elsevier Science, (1993).

[50]     D. G. Schlom, J. H. Haeni, J. Lettieri, C. D. Theis, W. Tian, J. C. Jiang*, et al.*, "Oxide nano-engineering using MBE," *Mater. Sci. Eng. B* 87, 282-291 (2001).

[51]     H. M. Christen and G. Eres, "Recent advances in pulsed-laser deposition of complex oxides," *J. Phys.-Condes. Matter* 20, 16 (2008).

[52]     P. J. Kelly and R. D. Arnell, "Magnetron sputtering: a review of recent developments and applications," *Vacuum* 56, 159-172 (2000).

[53]     J. Son, J. M. LeBeau, S. J. Allen, and S. Stemmer, "Conductivity enhancement of ultrathin $LaNiO_3$ films in superlattices," *Appl. Phys. Lett.* 97, 3 (2010).

[54]     J. J. Cuomo, D. L. Pappas, J. Bruley, J. P. Doyle, and K. L. Saenger, "Vapor-Deposition Processes for Amorphous-carbon Films with $sp^3$ Fractions Approaching Diamond," *J. Appl. Phys.* 70, 1706-1711 (1991).

[55]     B. Jalan, P. Moetakef, and S. Stemmer, "Molecular beam epitaxy of $SrTiO_3$ with a growth window," *Appl. Phys. Lett.* 95, 3 (2009).

[56]  C. D. Theis, J. Yeh, D. G. Schlom, M. E. Hawley, and G. W. Brown, "Adsorption-controlled growth of PbTiO$_3$ by reactive molecular beam epitaxy," *Thin Solid Films* 325, 107-114 (1998).

[57]  J. F. Ihlefeld, A. Kumar, V. Gopalan, D. G. Schlom, Y. B. Chen, X. Q. Pan*, et al.*, "Adsorption-controlled molecular-beam epitaxial growth of BiFeO$_3$," *Appl. Phys. Lett.* 91, 071922 (2007).

[58]  J. H. Haeni, C. D. Theis, and D. G. Schlom, "RHEED intensity oscillations for the stoichiometric growth of SrTiO$_3$ thin films by reactive molecular beam epitaxy," *J. Electroceram.* 4, 385-391 (2000).

[59]  C. Lu and Y. Guan, "Improved Method of Nonintrusive Deposition Rate Monitoring by Atomic-Absorption Spectroscopy for Physical Vapor-Deposition Processes," *J. Vac. Sci. Technol. A* 13, 1797-1801 (1995).

[60]  Z. Yu, Y. Liang, C. Overgaard, X. Hu, J. Curless, H. Li*, et al.*, "Advances in heteroepitaxy of oxides on silicon," *Thin Solid Films* 462, 51-56 (2004).

[61]  P. Fisher, H. Du, M. Skowronski, P. A. Salvador, O. Maksimov, and X. Weng, "Stoichiometric, nonstoichiometric, and locally nonstoichiometric SrTiO$_3$ films grown by molecular beam epitaxy," *J. Appl. Phys.* 103, 10 (2008).

[62]  T. Ohnishi, K. Shibuya, T. Yamamoto, and M. Lippmaa, "Defects and transport in complex oxide thin films," *J. Appl. Phys.* 103, 103703 (2008).

[63]  B. E. Yoldas, "Preparation of Glasses and Ceramics from Metal-organic Compounds," *J. Mater. Sci.* 12, 1203-1208 (1977).

[64]  M. Balog, M. Schieber, M. Michman, and S. Patai, "Chemical Vapor-deposition and Characterization of HfO$_2$ Films from Organo-hafnium Compounds," *Thin Solid Films* 41, 247-259 (1977).

[65]  M. Balog, M. Schieber, M. Michman, and S. Patai, "Chemical Vapor-deposition and Characterization of ZrO$_2$ Films from Organometallic Compounds," *Thin Solid Films* 47, 109-120 (1977).

[66]  J. A. Belot, D. A. Neumayer, C. J. Reedy, D. B. Studebaker, B. J. Hinds, C. L. Stern*, et al.*, "Volatility by design. Synthesis and characterization of polyether adducts of

bis(1,1,1,5,5,5-hexafluoro-2,4-pentanedionato)barium and their implementation as metal-organic chemical vapor deposition precursors," *Chem. Mat.* 9, 1638-1648 (1997).

[67] A. D. Berry, D. K. Gaskill, R. T. Holm, E. J. Cukauskas, R. Kaplan, and R. L. Henry, "Formation of High-$T_C$ Superconducting Films by Organometallic Chemical Vapor-deposition," *Appl. Phys. Lett.* 52, 1743-1745 (1988).

[68] D. A. Boyd, S. G. Hirsch, C. Hubbard, and M. W. Cole, "BST Films Grown by Metal Organic Chemical Vapor Deposition Incorporating Real-Time Control of Stoichiometry," *Integr. Ferroelectr.* 111, 17-26 (2009).

[69] A. M. Dhote, A. L. Meier, D. J. Towner, B. W. Wessels, J. Ni, and T. J. Marks, "Low temperature deposition of epitaxial BaTiO$_3$ films in a rotating disk vertical MOCVD reactor," *J. Vac. Sci. Technol. B* 23, 1674-1678 (2005).

[70] J. F. Roeder, T. H. Baum, S. M. Bilodeau, G. T. Stauf, C. Ragaglia, M. W. Russell*, et al.*, "Liquid-delivery MOCVD: Chemical and process perspectives on ferro-electric thin film growth," *Adv. Mater. Opt. Electron.* 10, 145-154 (2000).

[71] A. R. Teren, J. A. Belot, N. L. Edleman, T. J. Marks, and B. W. Wessels, "MOCVD of epitaxial BaTiO$_3$ films using a liquid barium precursor," *Chem. Vapor Depos.* 6, 175-177 (2000).

[72] K. H. Ahn, Y. B. Park, and D. W. Park, "Kinetic and mechanistic study on the chemical vapor deposition of titanium dioxide thin films by in situ FT-IR using TTIP," *Surf. Coat. Technol.* 171, 198-204 (2003).

[73] D. J. Burleson, J. T. Roberts, W. L. Gladfelter, S. A. Campbell, and R. C. Smith, "A study of CVD growth kinetics and film microstructure of zirconium dioxide from zirconium tetra-tert-butoxide," *Chem. Mat.* 14, 1269-1276 (2002).

[74] S. Chen, M. G. Mason, H. J. Gysling, G. R. Pazpujalt, T. N. Blanton, T. Castro*, et al.*, "Ultrahigh-vacuum Metalorganic Chemical-vapor-deposition Growth and *in-situ* Characterization of Epitaxial TiO$_2$ Films," *J. Vac. Sci. Technol. A* 11, 2419-2429 (1993).

[75] M. Nandi, D. Rhubright, and A. Sen, "Pyrolytic Transformation of Metal Alkoxides to Oxides - Mechanistic Studies - Pyrolysis of Homoleptic Titanium Alkoxides," *Inorg. Chem.* 29, 3065-3066 (1990).

[76]    C. J. Taylor, D. C. Gilmer, D. G. Colombo, G. D. Wilk, S. A. Campbell, J. Roberts, *et al.*, "Does chemistry really matter in the chemical vapor deposition of titanium dioxide? Precursor and kinetic effects on the microstructure of polycrystalline films," *J. Am. Chem. Soc.* 121, 5220-5229 (1999).

[77]    K. Endo, S. Saya, S. Misawa, and S. Yoshida, "Preparation of Yttrium Barium Copper-oxide Superconducting Films by Metalorganic Molecular-Beam Epitaxy," *Thin Solid Films* 206, 143-145 (1991).

[78]    J. P. Bade, E. A. Baker, A. I. Kingon, R. F. Davis, and K. J. Bachmann, "Deposition of Oxide-Films by Metal-Organic Molecular-Beam Epitaxy," *J Vac Sci Technol B* 8, 327-331 (1990).

[79]    P. C. Van Buskirk, S. M. Bilodeau, J. F. Roeder, and P. S. Kirlin, "Metalorganic chemical vapor deposition of complex metal oxide thin films by liquid source chemical vapor deposition," *Jpn. J. Appl. Phys. Part 1* 35, 2520-2525 (1996).

[80]    D. C. Bradley, "Metal Alkoxides as Precursors for Electronic and Ceramic Materials," *Chem. Rev.* 89, 1317-1322 (1989).

[81]    C. P. Fictorie, J. F. Evans, and W. L. Gladfelter, "Kinetic and Mechanistic Study of the Chemical-vapor-deposition of Titanium-dioxide Thin-films Using *tetrakis*-(isopropoxo)-titanium(IV)," *J. Vac. Sci. Technol. A* 12, 1108-1113 (1994).

[82]    B. Jalan, R. Engel-Herbert, J. Cagnon, and S. Stemmer, "Growth modes in metal-organic molecular beam epitaxy of $TiO_2$ on r-plane sapphire," *J. Vac. Sci. Technol. A* 27, 230-233 (2009).

[83]    F. Niu, B. H. Hoerman, and B. W. Wessels, "Epitaxial thin films of MgO an Si using metalorganic molecular beam epitaxy," *J. Vac. Sci. Technol. B* 18, 2146-2152 (2000).

[84]    K. Ogata, T. Kawanishi, K. Maejima, K. Sakurai, S. Fujita, and S. Fujita, "Improvements of ZnO qualities grown by metal-organic vapor phase epitaxy using a molecular beam epitaxy grown ZnO layer as a substrate," *Jpn. J. Appl. Phys. Part 2 - Lett.* 40, L657-L659 (2001).

[85]    L. L. H. King, K. Y. Hsieh, D. J. Lichtenwalner, and A. I. Kingon, "In-situ Deposition of Superconducting $YBa_2Cu_3O_{7-x}$ and $DyBa_2Cu_3O_{7-x}$ Thin-films by Organometallic Molecular-beam Epitaxy," *Appl. Phys. Lett.* 59, 3045-3047 (1991).

[86]     E. S. Hellman and E. H. Hartford, "Effects of Oxygen on the Sublimation of Alkaline-earths from Effusion Cells," *J. Vac. Sci. Technol. B* 12, 1178-1180 (1994).

[87]     C. D. Theis and D. G. Schlom, "Cheap and stable titanium source for use in oxide molecular beam epitaxy systems," *J. Vac. Sci. Technol. A* 14, 2677-2679 (1996).

[88]     B. E. Yoldas, "Hydrolysis of Aluminum Alkoxides and Bayerite Conversion," *J. Appl. Chem. Biotechnol.* 23, 803-809 (1973).

[89]     B. Jalan, R. Engel-Herbert, N. J. Wright, and S. Stemmer, "Growth of high-quality $SrTiO_3$ films using a hybrid molecular beam epitaxy approach," *J. Vac. Sci. Technol. A* 27, 461-464 (2009).

[90]     D. J. Keeble, B. Jalan, L. Ravelli, W. Egger, G. Kanda, and S. Stemmer, "Suppression of vacancy defects in epitaxial La-doped $SrTiO_3$ films," *Appl. Phys. Lett.* 99, 232905 (2011).

[91]     D. J. Keeble, S. Wicklein, R. Dittmann, L. Ravelli, R. A. Mackie, and W. Egger, "Identification of A- and B-Site Cation Vacancy Defects in Perovskite Oxide Thin Films," *Phys. Rev. Lett.* 105, 226102 (2010).

[92]     J. Son, P. Moetakef, B. Jalan, O. Bierwagen, N. J. Wright, R. Engel-Herbert*, et al.*, "Epitaxial $SrTiO_3$ films with electron mobilities exceeding 30,000 $cm^2V^{-1}s^{-1}$," *Nat. Mater.* 9, 482-484 (2010).

[93]     T. A. Cain, A. P. Kajdos, and S. Stemmer, "La-doped $SrTiO_3$ films with large cryogenic thermoelectric power factors," *Appl. Phys. Lett.* 102, 4 (2013).

[94]     K. J. Ross and B. Sonntag, "High-temperature Metal Atom Beam Sources," *Rev. Sci. Instrum.* 66, 4409-4433 (1995).

[95]     T. Harigai, D. Tanaka, S. M. Nam, H. Kakemoto, S. Wada, K. Saito*, et al.*, "Preparation and dielectric properties of $SrZrO_3/SrTiO_3$ superlattices," *Jpn. J. Appl. Phys. Part 1* 43, 6530-6534 (2004).

[96]     R. Engel-Herbert, Y. Hwang, J. Cagnon, and S. Stemmer, "Metal-oxide-semiconductor capacitors with $ZrO_2$ dielectrics grown on $In_{0.53}Ga_{0.47}As$ by chemical beam deposition," *Appl. Phys. Lett.* 95, 062908 (2009).

[97]     D. C. Bradley and J. D. Swanwick, "Vapour Pressures of Metal Alkoxides 2. Zirconium tetra-*tert*-butoxide and tetra-*tert*-amyloxide," *J. Chem. Soc.* 748-752 (1959).

[98]     A. P. Kajdos and S. Stemmer, "Surface reconstructions in molecular beam epitaxy of $SrTiO_3$," *Appl. Phys. Lett.* 105, 191901 (2014).

[99]     Y. Du, D. J. Kim, T. C. Kaspar, S. E. Chamberlin, I. Lyubinetsky, and S. A. Chambers, "*In-situ* imaging of the nucleation and growth of epitaxial anatase $TiO_2(001)$ films on $SrTiO_3(001)$," *Surf. Sci.* 606, 1443-1449 (2012).

[100]    S. Stemmer, S. K. Streiffer, N. D. Browning, and A. I. Kingon, "Accommodation of nonstoichiometry in (100) fiber-textured $(Ba_xSr_{1-x})Ti_{1-y}O_{3+z}$ thin films grown by chemical vapor deposition," *Appl. Phys. Lett.* 74, 2432-2434 (1999).

[101]    M. R. Castell, "Scanning tunneling microscopy of reconstructions on the $SrTiO_3(001)$ surface," *Surf. Sci.* 505, 1-13 (2002).

[102]    S. Gerhold, Z. Wang, M. Schmid, and U. Diebold, "Stoichiometry-driven switching between surface reconstructions on $SrTiO_3(001)$," *Surf. Sci.* 621, L1-L4 (2014).

[103]    Q. D. Jiang and J. Zegenhagen, "c(6x2) and c(4x2) reconstruction of $SrTiO_3(001)$," *Surface Science* 425, 343-354 (1999).

[104]    N. Erdman, O. Warschkow, M. Asta, K. R. Poeppelmeier, D. E. Ellis, and L. D. Marks, "Surface structures of $SrTiO_3$ (001): A $TiO_2$-rich reconstruction with a c(4 x 2) unit cell," *J. Am. Chem. Soc.* 125, 10050-10056 (2003).

[105]    M. Naito and H. Sato, "Reflection High-Energy Electron-Diffraction Study on the $SrTiO_3$ Surface-Structure," *Physica C* 229, 1-11 (1994).

[106]    N. Erdman, K. R. Poeppelmeier, M. Asta, O. Warschkow, D. E. Ellis, and L. D. Marks, "The structure and chemistry of the $TiO_2$-rich surface of $SrTiO_3(001)$," *Nature* 419, 55-58 (2002).

[107]    O. G. Vendik and S. P. Zubko, "Ferroelectric phase transition and maximum dielectric permittivity of displacement type ferroelectrics $(Ba_xSr_{1-x}TiO_3)$," *J. Appl. Phys.* 88, 5343-5350 (2000).

[108]  X. X. Xi, H. C. Li, W. D. Si, A. A. Sirenko, I. A. Akimov, J. R. Fox, *et al.*, "Oxide thin films for tunable microwave devices," *J. Electroceram.* 4, 393-405 (2000).

[109]  J. M. Worlock and P. A. Fleury, "Electric Field Dependence of Optical-Phonon Frequencies," *Phys. Rev. Lett.* 19, 1176-& (1967).

[110]  N. K. Pervez, P. J. Hansen, and R. A. York, "High tunability barium strontium titanate thin films for rf circuit applications," *Appl. Phys. Lett.* 85, 4451-4453 (2004).

[111]  A. Vorobiev, P. Rundqvist, K. Khamchane, and S. Gevorgian, "Microwave loss mechanisms in $Ba_{0.25}Sr_{0.75}TiO_3$ thin film varactors," *J. Appl. Phys.* 96, 4642-4649 (2004).

[112]  K. F. Astafiev, A. K. Tagantsev, and N. Setter, "Quasi-Debye microwave loss as an intrinsic limitation of microwave performance of tunable components based on $SrTiO_3$ and $Ba_xSr_{1-x}TiO_3$ ferroelectrics," *J. Appl. Phys.* 97, 8 (2005).

[113]  A. K. Tagantsev and K. F. Astafiev, "Quasi-Debye microwave loss in Perovskite ferroelectrics," *Integr. Ferroelectr.* 39, 1201-1210 (2001).

[114]  K. F. Astafiev, V. O. Sherman, A. K. Tagantsev, N. Setter, T. Kaydanova, and D. S. Ginley, "Crossover between extrinsic and intrinsic dielectric loss mechanisms in $SrTiO_3$ thin films at microwave frequencies," *Appl. Phys. Lett.* 84, 2385-2387 (2004).

[115]  J. Im, O. Auciello, P. K. Baumann, S. K. Streiffer, D. Y. Kaufman, and A. R. Krauss, "Composition-control of magnetron-sputter-deposited $(Ba_xSr_{1-x})Ti_{1+y}O_{3+z}$ thin films for voltage tunable devices," *Appl. Phys. Lett.* 76, 625-627 (2000).

[116]  X. Y. Zhang, P. Wang, S. Sheng, F. Xu, and C. K. Ong, "Ferroelectric $Ba_xSr_{1-x}TiO_3$ thin-film varactors with parallel plate and interdigital electrodes for microwave applications," *J. Appl. Phys.* 104, 6 (2008).

[117]  E. Mikheev, B. D. Hoskins, D. B. Strukov, and S. Stemmer, "Resistive switching and its suppression in $Pt/Nb:SrTiO_3$ junctions," *Nat. Commun.* 5, 8 (2014).

[118]  M. Stengel and N. A. Spaldin, "Origin of the dielectric dead layer in nanoscale capacitors," *Nature* 443, 679-682 (2006).

[119] J. Son, J. Cagnon, and S. Stemmer, "Strain relaxation in epitaxial Pt films on (001) SrTiO$_3$," *J. Appl. Phys.* 106, 3 (2009).

[120] Q. J. Gao and T. T. Tsong, "Direct Observation of Atomic Structures in the Surface Reconstruction of Ir and Pt (001), (110), and (131) Surfaces," *Phys. Rev. B* 36, 2547-2556 (1987).

[121] E. Mikheev, A. P. Kajdos, A. J. Hauser, and S. Stemmer, "Electric field-tunable Ba$_x$Sr$_{1-x}$TiO$_3$ films with high figures of merit grown by molecular beam epitaxy," *Appl. Phys. Lett.* 101, 4 (2012).

[122] R. A. York, *Multifunctional Adaptive Microwave Circuits and Systems*: SciTech, (2009).

[123] J. C. Shin, J. Park, C. S. Hwang, and H. J. Kim, "Dielectric and electrical properties of sputter grown (Ba,Sr)TiO$_3$ thin films," *J. Appl. Phys.* 86, 506-513 (1999).

[124] M. T. Lanagan, "Microwave dielectric properties of antiferroelectric lead zirconate," The Pennsylvania State University, 1987.

[125] H. V. Alexandru, C. Berbecaru, F. Stanculescu, A. Ioachim, M. G. Banciu, M. I. Toacsen*, et al.*, "Ferroelectric solid solutions (Ba,Sr)TiO$_3$ for microwave applications," *Mater. Sci. Eng. B* 118, 92-96 (2005).

[126] J. Krupka, R. G. Geyer, M. Kuhn, and J. H. Hinken, "Dielectric-Properties of Single-Crystals of Al$_2$O$_3$, LaAlO$_3$, NdGaO$_3$, SrTiO$_3$, and MgO at Cryogenic Temperatures," *IEEE Trans. Microw. Theory Tech.* 42, 1886-1890 (1994).

[127] K. Bethe, "Microwave properties of nonlinear dielectrics," in *Microwave properties of nonlinear dielectrics*, ed, 1970, p. 145.

[128] I. B. Vendik, O. G. Vendik, and E. L. Kollberg, "Commutation quality factor of two-state switchable devices," *IEEE Transactions on Microwave Theory and Techniques* 48, 802-808 (2000).

[129] T. J. Jackson and I. P. Jones, "Nanoscale defects and microwave properties of (BaSr)TiO$_3$ ferroelectric thin films," *J. Mater. Sci.* 44, 5288-5296 (2009).

[130] A. Tombak, J. P. Maria, F. Ayguavives, Z. Jin, G. T. Stauf, A. I. Kingon, *et al.*, "Tunable barium strontium titanate thin film capacitors for RF and microwave applications," *IEEE Microw. Wirel. Compon. Lett.* 12, 3-5 (2002).

[131] A. P. Kajdos, D. G. Ouellette, T. A. Cain, and S. Stemmer, "Two-dimensional electron gas in a modulation-doped $SrTiO_3$/$Sr(Ti, Zr)O_3$ heterostructure," *Appl. Phys. Lett.* 103, 082120 (2013).

[132] H. Q. Hou, B. W. Liang, T. P. Chin, and C. W. Tu, "In-situ Determination of Phosphorus Composition in $GaAs_{1-x}P_x$ Grown by Gas-source Molecular-Beam Epitaxy," *Appl. Phys. Lett.* 59, 292-294 (1991).

[133] A. Y. Egorov, A. R. Kovsh, V. M. Ustinov, A. E. Zhukov, P. S. Kop'ev, and C. W. Tu, "A thermodynamic analysis of the growth of III-V compounds with two volatile group V elements by molecular-beam epitaxy," *J. Cryst. Growth* 188, 69-74 (1998).

[134] J. Robertson and P. W. Peacock, "Doping and hydrogen in wide gap oxides," *Thin Solid Films* 445, 155-160 (2003).

[135] A. Verma, A. P. Kajdos, T. A. Cain, S. Stemmer, and D. Jena, "Intrinsic Mobility Limiting Mechanisms in Lanthanum-Doped Strontium Titanate," *Phys. Rev. Lett.* 112, 5 (2014).

[136] M. Grundmann, BandEng program

[137] P. Delugas, A. Filippetti, V. Fiorentini, D. I. Bilc, D. Fontaine, and P. Ghosez, "Spontaneous 2-Dimensional Carrier Confinement at the n-Type $SrTiO_3$/$LaAlO_3$ Interface," *Phys. Rev. Lett.* 106, 4 (2011).

[138] G. Khalsa and A. H. MacDonald, "Theory of the $SrTiO_3$ surface state two-dimensional electron gas," *Phys. Rev. B* 86, 125121 (2012).

[139] W. J. Son, E. Cho, B. Lee, J. Lee, and S. Han, "Density and spatial distribution of charge carriers in the intrinsic n-type $LaAlO_3$-$SrTiO_3$ interface," *Phys. Rev. B* 79, 7 (2009).

[140] H. Uwe, R. Yoshizaki, T. Sakudo, A. Izumi, and T. Uzumaki, "Conduction Band Structure of $SrTiO_3$," *Jap. J. Appl. Phys.* 24, 335--337 (1985).

[141]  B. Jalan, S. Stemmer, S. Mack, and S. J. Allen, "Two-dimensional electron gas in $\delta$-doped SrTiO$_3$," *Phys. Rev. B* 82, 4 (2010).

[142]  T. H. Sander, S. N. Holmes, J. J. Harris, D. K. Maude, and J. C. Portal, "Determination of the phase of magneto-intersubband scattering oscillations in heterojunctions and quantum wells," *Phys. Rev. B* 58, 13856--13862 (1998).

[143]  L. Bjaalie, B. Himmetoglu, L. Weston, A. Janotti, and C. G. Van de Walle, "Oxide interfaces for novel electronic applications," *New J. Phys.* 16, 1-18 (2014).

[144]  P. D. C. King, R. H. He, T. Eknapakul, P. Buaphet, S. K. Mo, Y. Kaneko*, et al.*, "Subband Structure of a Two-Dimensional Electron Gas Formed at the Polar Surface of the Strong Spin-Orbit Perovskite KTaO$_3$," *Phys. Rev. Lett.* 108, 5 (2012).

[145]  S. H. Wemple, "Some Transport Properties of Oxygen-Deficient Single-Crystal Potassium Tantalate (KTaO$_3$)," *Phys. Rev.* 137, 1575-1582 (1965).

[146]  A. Vegas, M. Valletregi, J. M. Gonzalezcalbet, and M. A. Alariofranco, "The ASnO$_3$ (A=Ca, Sr) Perovskites," *Acta Crystallogr. B* 42, 167-172 (1986).